TÉCNICO LISBOA

Synthesis and characterization of Gallium-based materials for catalytic applications

Pedro Alexandre Lopes Martins

Thesis to obtain the Master of Science Degree in

Materials Engineering

Supervisors: Dr. Joaquim Miguel Badalo Branco
Dra. Ana Cristina Gomes Ferreira da Silva Parreira

Examination Committee

Chairperson: Professor Dr. José Paulo Sequeira Farinha
Supervisor: Dra. Ana Cristina Gomes Ferreira da Silva Parreira
Members of the Committee: Dra. Carla Maria Duarte Nunes

December 2022

"Agir, eis a inteligência verdadeira. Serei o que quiser.
Mas tenho que querer o que for. O êxito está em
ter êxito, e não em ter condições de êxito.
Condições de palácio tem qualquer terra larga,
mas onde estará o palácio se não o fizerem ali?"

Fernando Pessoa, in *Livro do Desassossego*

Acknowledgements

For the success of this thesis, I have undoubtably to start by thanking my supervisors, Doctor Ana Ferreira and Doctor Joaquim Branco, for all the support, guidance, and help throughout the months I have been at CTN. During this period, many were the obstacles and challenges we faced and without their patience, professionalism, and love to this field, it would have been impossible to finish this thesis. To them, all my gratitude and consideration.

Beside my supervisors, there is no doubt about the person that help and taught me the most. More than a co-worker, a friend that I had the pleasure and good fortune to meet at CTN. To the PhD student, my dear friend, Joana Martinho, I thank for every laugh and teaching, all the patience to my systematic complaints, all the music chosen to cheer me up in those hard days, but most of all, for the friendship. I also want to thank Marta Silva for all the path we have done together, for always being there when I needed the most, for the patience to all my requests, and for being an amazing co-worker and friend. Without them, this work would have been a lot more difficult, and I could not have been luckier to have them with me.

For everyone I met at CTN, I thank for welcoming me so well from the very first day and for also being an important part of my journey.

To my family, especially my mother, father, brother and grandparents, I owe them everything I am and have accomplished. They are an immutable part of me. Throughout my life and particularly in these five years at IST, they were a crucial support that was always there for the good and not so good moments.

Finally, I want to thank my dear friends. These five years were some of the most challenging I have faced to this day, and without them, I could not have come this far. To all the friends I have made throughout these years at IST and in my Erasmus semester in Padua, I have to thank for all the help and support you gave me, and for being a part of this important chapter in my life which is about to end. My dear friends from Colégio Militar, from the so called “curso 2009”, they were always there for me, and they are an essential part of me that I know I can count on for my entire life. To them, “um forte Zacatraz”.

To all, my sincere gratitude.

Abstract

Gallium oxide's unique electrochemical properties have brought attention to several applications, but those in catalytic reactions seem to be fewer. One that has shown some interesting results is the oxidative dehydrogenation of ethane (ODHE) aiming the production of ethylene, a key building block for the polymer industry. However, the rapid deactivation of Ga_2O_3 is the main drawback. Adding other oxides, such as cerium and copper seems to improve the stability and performance of gallium-based catalysts, namely by increasing the number of oxygen vacancies and promoting the key reactions responsible for the catalytic activity.

In this work, gallium-cerium bimetallic oxides with three molar ratios (Ga:Ce=1:3, 1:1 and 3:1) were prepared by two methods: electrospinning technique and epoxide addition method (sol-gel method), aiming at the synthesis of compounds with different morphologies (fibres or aerogels) and to test them as catalysts for ODHE. Besides, to investigate the effect on this reaction, copper oxide supported on Ga_2O_3, CeO_2 and Ga:Ce (1:1) bimetallic oxide aerogels were also prepared.

The catalytic performance for ODHE depends on the type of oxidant used, catalyst morphology, crystallite size and catalysts' acid-base properties. From the oxidizing agents tested, N_2O presented the best results. Among the bimetallic Ga-Ce oxides, the best results were those obtained over the fibres with the highest molar ratio, with 87% of ethane conversion and 13% of ethylene yield at 650ºC. Moreover, the copper-based materials, especially the one supported on CeO_2 presented the highest catalytic performance, with 97% ethane conversion and 7% ethylene yield at 650ºC. This confirms that copper has an enhanced effect on the catalyst's behaviour, as well as gallium. To our knowledge, this is the first time that such type of results using gallium-based catalysts are reported in the literature.

Keywords: Gallium, Cerium, Copper, Bimetallic oxides, ODHE, Ethylene.

Resumo

O óxido de gálio tem propriedades eletroquímicas únicas e potencialidades em inúmeras aplicações. No entanto, ainda não é muito usado como catalisador em reações catalíticas de interesse. Destas, uma das reações que tem despertado interesse devido aos resultados promissores é a reação de desidrogenação oxidativa do etano visando a produção de etileno, um composto fundamental para indústria química. No entanto, o Ga_2O_3 tem como principal desvantagem a sua rápida desativação, mas a adição de outros óxidos, como o de cério e o de cobre, parece melhorar a sua estabilidade e desempenho catalítico, nomeadamente devido ao aumento do número de lacunas de oxigénio responsáveis pela promoção da sua atividade catalítica.

Neste trabalho, foram preparados óxidos bimetálicos de gálio-cério com três razões molares (Ga:Ce=1:3, 1:1 e 3:1) usando para tal dois métodos: a técnica de eletrofiação e o método de adição de epóxido (método sol-gel), visando a síntese de compostos com diferentes morfologias (fibras ou aerogéis) e o teste destes como catalisadores para a desidrogenação oxidativa do etano. Além disso, para estudar o seu efeito nesta reação, foram também preparados catalisadores de óxido de cobre suportados em aerogéis de Ga_2O_3, CeO_2 e óxido bimetálico de Ga-Ce (1:1).

Os resultados obtidos mostram que o seu desempenho catalítico nesta reação depende do tipo de oxidante utilizado (O_2, CO_2, N_2O), tendo os melhores sido obtidos com N_2O; da morfologia do catalisador, os melhores foram os obtidos com as fibras; do tamanho das cristalites e das propriedades ácido-base do catalisador, a atividade diminui com o tamanho da cristalite e aumento com a basicidade do catalisador. Entre os óxidos bimetálicos de Ga-Ce, os melhores resultados foram aqueles obtidos com o catalisador com o maior teor de gálio (3:1), obtendo 87% de conversão de etano e 13% de rendimento em etileno a 650°C. Alem disso, os catalisadores à base de cobre são os que apresentam os melhores resultados, especialmente o suportado em CeO_2, com 97% de conversão de etano e 7% de rendimento em etileno a 650°C. Assim, confirma-se que além do gálio também o cobre apresenta um efeito positivo na atividade catalítica destes catalisadores. Tanto quanto sabemos, esta é a primeira vez que este tipo de catalisadores são reportados na literatura para a desidrogenação do etano.

Palavras-Chave: Gálio, Cério, Cobre, Óxidos bimetálicos, Desidrogenação oxidativa de etano, Etileno.

Communications

- Pedro Martins, Ana C. Ferreira, Joaquim B. Branco. "*Oxidative Dehydrogenation of Ethane over Gallium-Cerium Bimetallic Oxides*", CQE Days, May 2022, Lisbon, Portugal.

Papers

- "*Synthesis and characterization of Gallium-based materials for dehydrogenation of ethane*"; in preparation.

Contents

List of Tables

Table of Figures

Abbreviations

$25_{wt.\%}$Cu: 25% in weight of copper

BET: Brunauer-Emmett-Teller method

BSE: Back Scattered Electrons

CVD: Chemical Vapour Deposition

DME: Dimethyl ether

E_a: Apparent Activation Energy

EDS: Energy Dispersive Spectroscopy

FZ: Floating Zone method

Ga:Ce : Ga-Ce bimetallic oxide

GC: Gas Chromatography

GHSV: Gas Hourly Space Velocity

HVPE: Halide Vapour Phase Epitaxy

ICSD: Inorganic Crystal Structure Database

MBE: Molecular Beam Epitaxy

MvK: Mars Van Krevelen model

ODHE: Oxidative dehydrogenation of ethane

OSSD: Organic Solvent Sublimation Drying method

PLD: Pulsed Laser Deposition

RF: Radio Frequency

RWGS: Reverse Water Gas Shift

SE: Secondary Electrons

SEM: Scanning Electron Microscopy

SSA: Specific Surface Area

TCD: Thermal Conductivity Detector

TPR: Temperature Programmed Reduction

UWBG: Ultra-Wide Band Gap

WBG: Wide Band Gap

XRD: X-ray Diffraction

1. Introduction

In a time of so many challenges constantly raised by social, economic, and political events, technology has always had a key rule to unravel these uncertainties. Hence, for the development of innovative solutions, novel materials are many times needed to defy and surpass current technologies, providing new opportunities in the development of society. Therefore, one of the main aims of this thesis was to study an emerging material with an immense potential yet to be unveiled. The chosen material was gallium oxide (Ga_2O_3).

Gallium was first discovered back in 1875 by French chemist Lecoq de Boisbaudran[1] and named it as a tribute to his home country, France. Thus, the element has his name inspired by the roman name for the region of the modern country, *Gallia*. However, it was not until 1950s and 1960s that gallium oxide started to be studied and characterized,[2] without ever attracting too much attention.

Nevertheless, gallium oxide has earned a growing interest in the past decade, as can be seen by the exponential increase in research articles related to it in **Figure 1**. Its emergence has mostly come from the recognition of its potential as an eventual replacement for conventional semiconductor materials in applications like power devices, photodetectors, optoelectronic devices, among others, as it will be addressed in further chapters. With an ultra-wide band gap (UWBG), around 4.5 to 5 eV,[3] Gallium oxide is now believed to have the potential to surpass some limitations of the other wide band gap (WBG) materials, such as SiC and GaN. Another ambitious driving force for the study of Ga_2O_3 lies in nanotechnology, where the large surface-to-volume ratio of nanostructures opens the possibility, frequently, to enhanced physical properties compared to equivalent bulk material. Hence, applications in catalysis and chemical sensing can take advantage of the nanostructure of gallium oxide.[4]

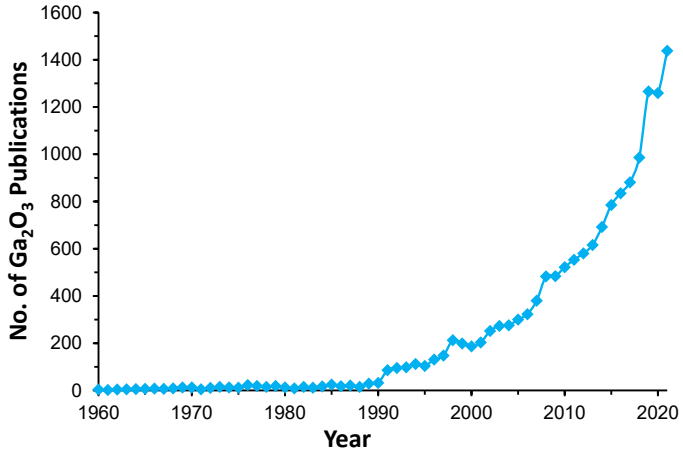

Figure 1: Evolution of the number of publications related to gallium oxide (Source: Web of Science[5])

Having a look at Ga_2O_3 crystal structures, in the literature it is usually reported that there are five polymorphs of this material. Each one having structures like rhombohedral (α), monoclinic (β), defective spinel (γ), cubic (δ), or orthorhombic (ε).[2,6] All five structures can exist in normal pressures and temperatures depending on the preparation conditions of this material.[7] Besides, varying the crystals

growing conditions, they may have different properties, e.g. insulating or a semiconducting electrical behaviour, if prepared under different conditions, e.g. oxidizing or reducing conditions, respectively.[8] However, the β-phase is the most stable either thermally or chemically and the remaining phases are metastable and convert into β-phase upon high temperatures (higher than 600 ºC).[2] Thus, the β-phase is the most studied and used, and for this reason, it will also be the primary focus of this thesis.

Even though there is a growing interest in gallium oxide, it is safe to say that its research and development is still in an incipient stage. To this day, there is still some controversy around several of its properties and even contradicting data. For instance, its n-type conductivity is relatively well established, but there is not a consensus about the existence or not of p-type conductivity, which has a huge implication for some applications in power devices.[4] Moreover, for what concerns its catalytic properties, there are still some doubts about what drives its catalytic activity, but several studies have demonstrated that polymorphism strongly influenced its catalytic properties.[9,10]

1.1. Gallium oxide properties

One of the most important aspects that may provide an explanation of the material's properties is its crystal structure. In the case of β-Ga_2O_3, it presents a monoclinic structure with two types of gallium ions (Ga^{3+}), represented in **Figure 2** as Ga0 and Ga1, and three types of oxygen ions (O2, O3, and O4). These different types of ions have a tetrahedral (Ga0) and octahedral (Ga1) coordination, which explains its asymmetry and the anisotropy of physical, optical, and electrical properties of this material.[6] In **Table 1**, some important properties of β-Ga_2O_3 are presented, exhibiting its anisotropy.

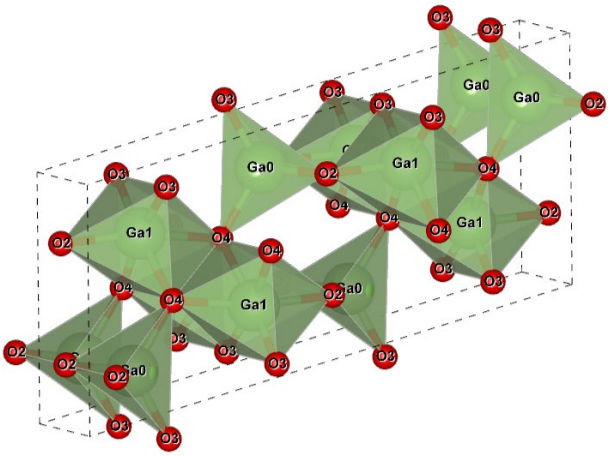

Figure 2: β-Ga_2O_3 crystal structure.[7]

Table 1: β–Ga_2O_3 properties.[4,11]

Property		Value	Ref.	Property		Value	Ref.
Melting Point		1793 °C	11	Breakdown Electric field, E_c		8 MV/cm	11
Density		5.95 g/cm^3	4	Band Gap		4.85 ± 0.1 eV	4
Crystal structure		Monoclinic	4	Mobility		100 cm^2/Vs	11
Space group		C2/m	4	Thermal Conductivity	[100]	10.9 ± 1 W/mK	11
Lattice parameters	a	12.214 Å	4		$[\bar{2}01]$	13.3 ± 1 W/mK	11
	b	3.0371 Å	4		[001]	14.7 ± 1.5 W/mK	11
	c	5.7981 Å	4		[110]	27 ± 2 W/mK	11
	β	103.83°	4	Refractive Index	[010]	1.9523	11
Dielectric constant		9.9-10.2	4		(100)	1.9201	11

Besides the crystal structure, another major factor is responsible for the unique gallium oxide properties: its ultra-wide bandgap (UWBG). Due to this factor, β–Ga_2O_3 can be used in high temperature operations as a semiconductor,[6] pure stoichiometric β-Ga_2O_3 is colourless and highly transparent up to UV-C range (around 250 nm) of the light spectrum.[4,6] This also means that it has strong bonds that inherently give a high radiation endurance.[12] Therefore, this oxide can be employed in the detection of UV radiation with wavelengths lower than 280 nm.

Furthermore, Ga_2O_3 is said to be the only UWBG oxide where its conductivity can be modulated by doping or by changing the atmospheric conditions.[3,13] For instance, when grown under reducing atmosphere, gallium oxide crystals show very good n-type conductivity. Ueda et al. observed that by decreasing the oxygen content in the growing atmosphere of β–Ga_2O_3 single crystals, it was possible to control their conductivity from $<10^{-9}$ to 38 Ω^{-1} cm^{-1}. Although it remains controversial, some have assigned this to the existence of oxygen vacancies, which are ionized and form electron donors.[13] However, Varley et al.[14] conducted calculations to understand the role of oxygen vacancies and some candidate donors in β–Ga_2O_3 conductivity. Their study suggests that oxygen vacancies, with an ionization energy of 1 eV, form a deep donor, meaning they do not take part in n-type conductivity. Therefore, they suggest that unintentional self-doping of β–Ga_2O_3 occurs due to impurities, like hydrogen and silicon, and according to their calculations, behave as shallow donors.

On the other hand, p-type conductivity has no reports showing undoubtedly hole conductivity. Currently, the lack of an appropriate method to synthesize p-type β–Ga_2O_3 is an important challenge that still needs to be overcome. Hence, both types of conductivity have some degree of controversy.

The UWBG of gallium oxide presents great potential for applications in power devices since it is expected that it could be able to deliver exceptional performance due to its estimated high breakdown voltage of 8 MV/cm, which is nearly three times larger than SiC or GaN, and have lower conduction losses than other semiconductors.[12,15,16] Thus gallium oxide may surpass the power handling limits of conventional semiconductors, like SiC and GaN, and be a good candidate to replace them.[3] **Table 2** summarized the most important electrical properties of the current semiconductors and gallium oxide.

Table 2: Electrical properties comparison between major semiconductors and β–Ga_2O_3. (Adapted from Pearton et al.[6]).

Property	Si	GaAs	4H-SiC	GaN	Diamond	β–Ga_2O_3
Bandgap – E_g (eV)	1.10	1.43	3.25	3.4	5.5	4.85 ± 0.1
Breakdown field – E_{br} (MV/cm)	0.3	0.4	2.5	3.3	10	8
Relative dielectric constant – ε	11.8	12.9	9.7	9.0	5.5	10
Electron mobility, μ (cm^2/Vs)	1 480	8 400	1 000	1 250	2 000	300
Baliga's FOM – $\varepsilon\,\mu\,E_{br}$	1	15	340	870	24 664	3 444
Thermal conductivity (W/mK)	150	55	490	230	2 000	[110] 27 [100] 10.9

However, this oxide has a poor thermal conductivity in comparison with other semiconductors and, due to its anisotropy, it varies along different crystal directions. Measured by laser flash methods, its thermal conductivity is 10.9 W/mK along the [100] direction and 27 W/mK along the [110] direction.[4] This characteristic can be problematic in some applications where thermal management is really important, as is the case for high-efficiency power devices, where the inevitable heat generation when poorly dissipated may impair the device performance severely.

Consequently, the lack of solid demonstration of p-type conductivity and the low thermal conductivity led to a severe drawback in a more mainstream Ga_2O_3 application.

As for its catalytic properties, it is believed that the tetrahedral Ga^{3+} sites form Lewis's acid sites. Only β- and γ-Ga_2O_3 have these tetrahedral Ga ions, which explains, on the other hand, why the formation of Lewis sites in α- and δ-Ga_2O_3 is unlikely, since they are composed only by octahedral Ga^{3+} sites.[9] Since the acid-base properties are of the most importance for catalytic activity and selectivity, Zheng et al.[9] has concluded that surface acidity is correlated with the reactivity of the gallium oxide polymorphs. This explains why β–Ga_2O_3 is the polymorph most active, as it has the highest surface acid site density.

1.2. Synthesis methods

Along with the first studies of gallium oxide properties, techniques were developed to synthesize this material. Since then, many techniques have been reported for the growth of bulk crystals, and, more recently, for the growth of thin films and nanostructures.

1.2.1. Gallium oxide bulk crystal growth

As opposed with bulk SiC and GaN single crystal substrates, which are often produced by sublimation techniques, Ga_2O_3 can be synthesized by several melt growth methods at lower costs. Common growth techniques like Verneuil method[17,18], Floating-Zone (FZ) method[19,20], Czochralski (CZ) method[21,22], edge-defined film fed (EFG) method[23,24], and horizontal or vertical Bridgman (HB or VB)

methods[25] have been employed. In fact, Ga_2O_3 wafers are already commercially available, made from CZ and EFG methods.[26]

1.2.1.1. Verneuil method

Also called flame fusion, the Verneuil method was created in 1902 by Auguste Verneuil. It is a crucible-free technique comprising melting the powder material using an oxyhydrogen flame, with the molten droplets then crystallizing into a boule,[17] as shown in **Figure 3**. Although this process is still used today to produce synthetic gemstones (sapphire or ruby) and being considered the precursor of modern industrial crystal growth, the bulk gallium oxide crystals produced by this method have poor quality compared to other more recently developed techniques.

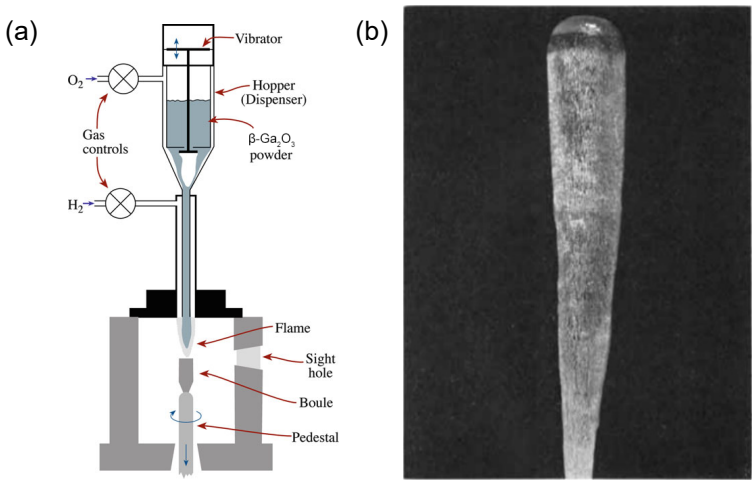

Figure 3: Verneuil method: (a) Scheme of technique's apparat (Adapted from Carter et al.[27]) and (b) β–Ga_2O_3 boule obtained by Verneuil method (Reproduced from Chase [17]).

This method allows crystal growth under oxidizing and reducing conditions. When synthesized under an oxidizing condition, β-Ga_2O_3 crystals were colourless and insulating.[18] While, in a reducing condition, the electron conductivity of the crystals improved and turned bluish.[18,28]

1.2.1.2. Floating zone method

In the floating zone (FZ) method, a rod consisting of a cold isostatic pressed Ga_2O_3 powder sintered at high temperature, at 1450 °C for 10 hours, is melted at one of its extremities.[19,20] This forms a melt zone between the rod, the feed material, and a lower seed material, as shown in **Figure 4**. The melt zone advances along the rod as the heating source rises and allows the crystal growth on the seed. As oxide crystals have low conductivity, halogen lamps are used as heaters.

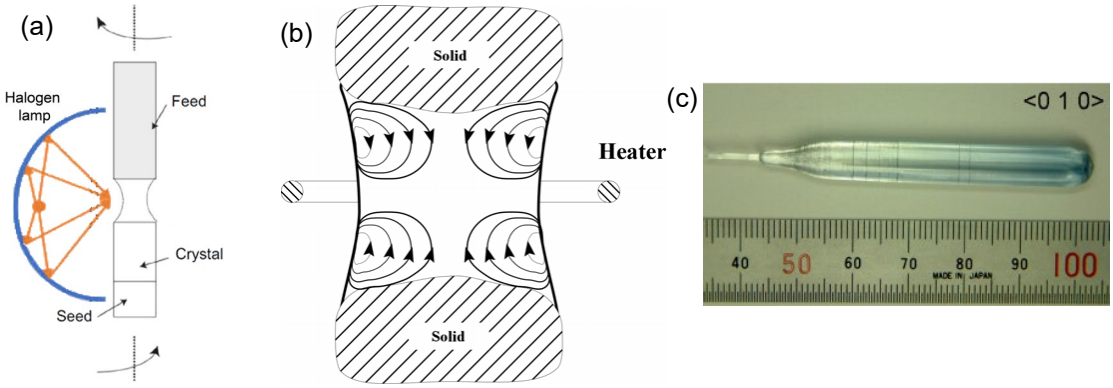

Figure 4: Floating zone method: (a) Scheme of FZ method (Reproduced from Nikolaev et al.[19]) and (b) scheme of the melt zone (Reproduced from Lappa[29]), and (c) β–Ga_2O_3 crystal grown along the <010> axis by the FZ method (Reproduced from Víllora et al.[20]).

The main advantage of this process is that the formed crystal and the melt zone are not in contact with any container. Having no crucible, this method allows the synthesis of crystals with a very low level of contamination. On the other hand, this also turns difficult to keep the melt from collapsing, as it is only held in place by surface tension.[12,19,29]

1.2.1.3. Czochralski method

The CZ method was invented by Czochralski, in 1915, as part of his investigation of the rate of metal crystallization.[30] This process has been used for growing single crystals of metals (Ag, Au, Pd, Pt, etc.), semiconductors (Si, Ge, GaAs, etc.), as well as artificial gemstones, proven to be capable of produce high quality and large diameter single crystals.[12] The method consists of dipping a seed crystal rod into a high purity melt of the desired material within an iridium crucible. Then, as the rod is pulled upwards and rotated simultaneously, a single crystal is formed. With this, a single crystal can be formed into sizable boules or cylindrical ingots (**Figure 5a**).[12,19]

β-Ga_2O_3 single crystals have been synthesized by Tomm et al.[21] and Galazka et al.[22] under a controlled atmosphere mostly of CO_2 in Ar (**Figure 5b**). These studies have shown that CO_2 is able to provide the oxygen partial pressure needed to ensure a good control over the Ga_2O_3 dissociation into volatile species (GaO and Ga_2O) and metallic gallium, which would alloy with the iridium and destroy the crucible. To prevent cracking, the growing crystal is pulled along the [010] direction, so that the cleavage planes (100) and (001) are parallel to the growth direction.

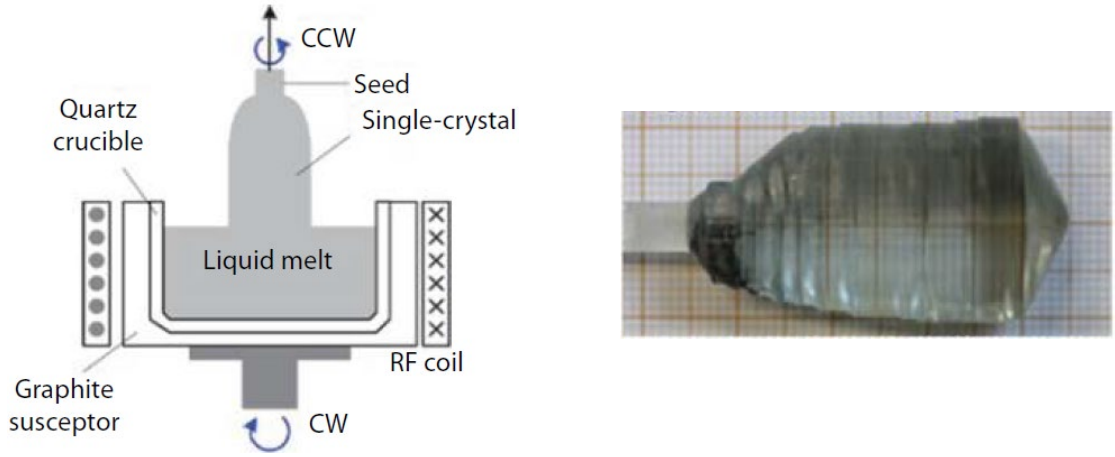

(a) (b)

Figure 5: Schematic of Czochralski method (a) (Reproduced from Mohamed et al.[12]), and (b) Bulk β–Ga_2O_3 synthesized by CZ method (Reproduced from Galazka et al.[22]).

1.2.1.4. Edge-defined film-fed growth method

This method was first developed for the growth of controlled profile crystals of sapphire by LaBelle et al.[31], and it is still being used in the mass production of sapphire wafers. It was found that, by melting a material, the melt will spread out to the edge of the die wetting all its surface. Thus, the geometry of the final crystal was dictated by the shape of the die and not by the column's diameter. Hence, the name of this method is edge-defined film-fed growth (EFG). Currently, bulk Ga_2O_3 crystals are commercially produced by EFG as well.[32] **Figure 6** illustrates how a EFG furnace works.

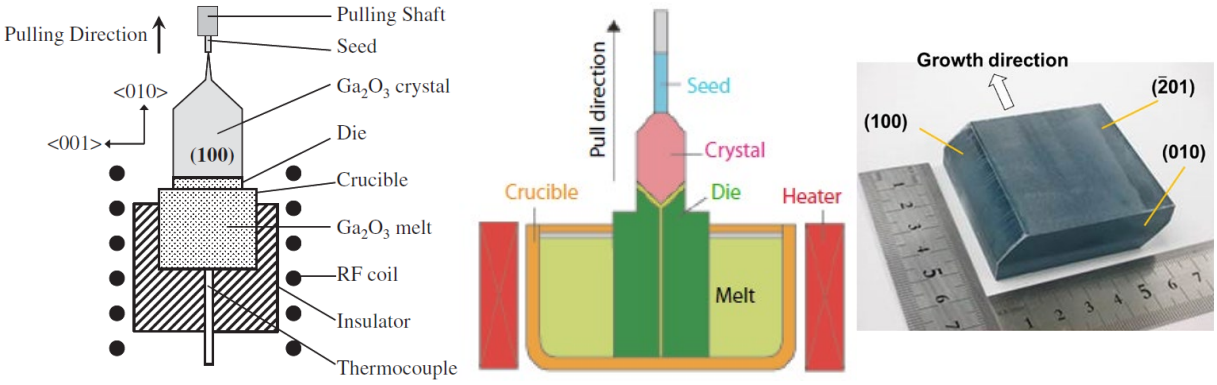

(a) (b) (c)

Figure 6: Schematic diagram of a furnace for EFG process (a)[24] (b)[12], and (c)[23] EFG-grown β-Ga_2O_3 bulk crystal.

The source material, Ga_2O_3 powder, is placed in an iridium crucible jointly with an iridium die under a mixture of 98% nitrogen and 2% oxygen. Around the crucible, a radio-frequency (RF) induction coil heats the powder until reaching β-Ga_2O_3 melting point. Then, the melt is drawn up by capillary action to the top surface of the iridium die through a slit in the die. A β-Ga_2O_3 seed crystal is placed in contact with the melt on the die's top surface to start the crystal growth process. Following this seeding process, the seed is pulled up and the crystals begun to grow on the die top surface.[23,24]

1.2.1.5. Bridgman method (vertical or horizontal)

In the production of bulk β-Ga_2O_3 single crystals, the need for high temperature means a higher chance for the raw material to undergo reductive decomposition. To avoid this, it is beneficial that the crystal grows under an oxidizing atmosphere. However, methods that use iridium crucibles, such as CZ and EFG, have the disadvantage of requiring a controlled atmosphere with no more than 2% of oxygen partial pressure at high temperature. This because iridium has a high reactivity when in contact with oxygen, which readily oxidizes and evaporates, plus (as mentioned before, in the CZ method) the decomposed metallic Ga alloys with Ir and form a volatile specie as well, damaging the crucible and possibly compromising the crystal formed. Furthermore, methods that grow a crystal by pulling a seed from the melt (like FZ, CZ, and EFG) may find hard to control the crystal's diameter.

With the vertical or horizontal Bridgman method (VB or HB), β-Ga_2O_3 crystals may be grown under air, since it allows the possibility of using platinum-based, for example, platinum-rhodium, crucibles in a very low temperature gradient. Moreover, in this process, diameter control is not an issue, as that is established by the inner diameter of the crucible itself.

The system that is used to melt the raw material by RF induction heating is represented in **Figure 7a**. After the complete melt of β–Ga_2O_3, the crucible is raised and lowered vertically or horizontally across the furnace (usually 0.5 mm/h), while its being rotated 3 rpm. This way, the melt is exposed to a gradient of temperatures inside different regions inside the furnace, leading to the graduate growth of a single crystal (**Figure 7b**).[25]

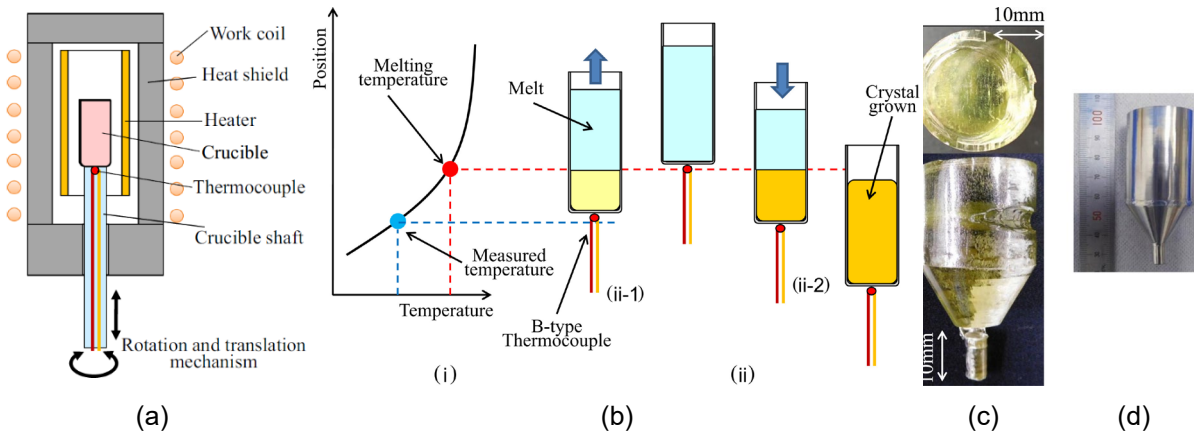

Figure 7: Bridgman method: (a) schematic diagram of a typical furnace. (b) Schematics of (i) the temperature distribution in the furnace, and (ii) the growth processes. (c) β–Ga_2O_3 single crystal grown by VB method and (d) its crucible. (Reproduced from Hoshikawa et al.[25])

1.2.2. Gallium oxide thin film growth

The progress seen in the production of β-Ga_2O_3 wafers and bulk single crystals can already have a huge importance for many applications on its own. However, more complex devices require high quality thin films to be employed as, for example, metal-semiconductor and metal-oxide-semiconductor field-effect transistors (MESFET and MOSFET), or nanostructures with high surface to volume ratio to be used in catalytic applications, for instance. In this chapter, the progress in thin film and nanostructures growth is discussed.

1.2.2.1. Pulsed laser deposition

This technique, known as pulsed laser deposition (PLD), is a very versatile method for the deposition of high-quality films which operates at low temperature, between 200 °C and 800 °C. Laser pulses are employed in this procedure to ablate material from a target, which is the material pretended to produce the thin film of. The material removed from the target then forms a plasma plume that is conduced to the substrate. The target and the substrate are in front of each other, a few centimetres apart, as presented in **Figure 8**. The parameters that control the crystalline quality of these thin films are the laser energy, the growth temperature, and the oxygen partial pressure. Nevertheless, the main drawbacks are the inferior quality of the layers formed, and the lower deposition rate compared to other methods, such as CVD and MBE, which are addressed in this chapter as well.[33]

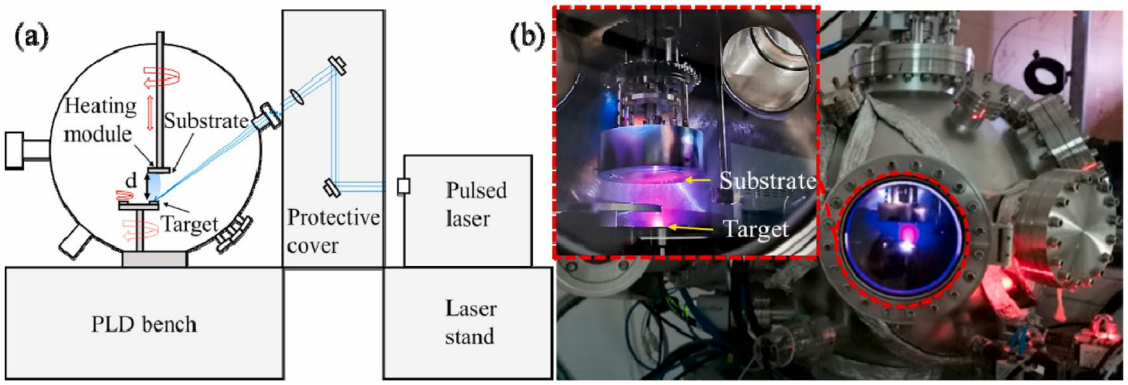

Figure 8: Pulsed laser deposition: (a) schematic diagram of the system, and (b) the plume of high density plasma species during the film deposition process.[34]

Wang et al.[34] studied the influence of the temperature in the growth of Ga_2O_3 thin films by PLD. The PLD chamber was filled with high-purity oxygen and a pressure of 0.1 Pa. Both the target and the substrates were rotated at different speeds so that the film formed had a better uniformity. The study shown that there is an inverse relation between the deposition rate and the substrate temperature, as the deposition rate became lower as higher was the temperature employed.

1.2.2.2. Molecular beam epitaxy

Mostly suited for research purposes, MBE is a well-established technique capable of synthesize high quality β-Ga_2O_3 thin films. However, its low growth rate and high production cost per film turns it unviable for commercial production in power device applications, especially since these usually require thick layers to achieve high breakdown voltages.[3,6]

The epitaxial film grown by this technique occurs under ultra-high vacuum (UHV) with a substrate heated at high temperatures. Víllora et al. and Oshima et al. reported the growth of β-Ga_2O_3 films onto a substrate heated at around 800 °C in a chamber pressure of 3.3×10^{-3} Pa. The film grows by the interaction between the substrate and adsorbed molecules originated from a molecular beam.

This beam is produced by the evaporation or sublimation of the metallic Ga contained an effusion cell, as shown in **Figure 9**. An oxygen plasma produced through a RF activated radical cell is introduced in the growth chamber. The layers formed have the same crystalline structure and a similar lattice parameter of the substrate.[35–37]

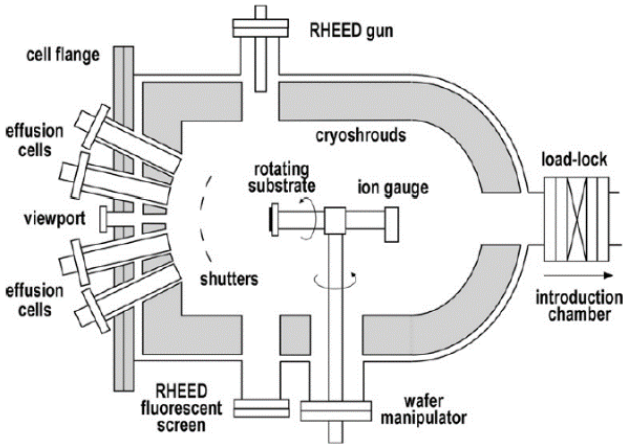

Figure 9: Schematic view of an MBE growth chamber. (Reproduced from Franchi[35])

1.2.2.3. Halide Vapour Phase Epitaxy

In power device applications where thick Ga_2O_3 layers are needed to assure sufficiently high breakdown voltage, Halide Vapour Phase Epitaxy (HVPE) allows to control the Ga_2O_3 film thickness and its electrical conductivity in a cost-effective way.[38] This technique has been recently used to produce GaN bulk substrates.[39] HVPE main advantages are its relatively lower cost, manufacture of higher-quality films, and higher deposition rates than other methods. However, these come at the cost of producing films with an unsuited surface morphology. Hence, chemical or mechanical polishing is compulsory before further processing into any application, which wastes material.[6,38]

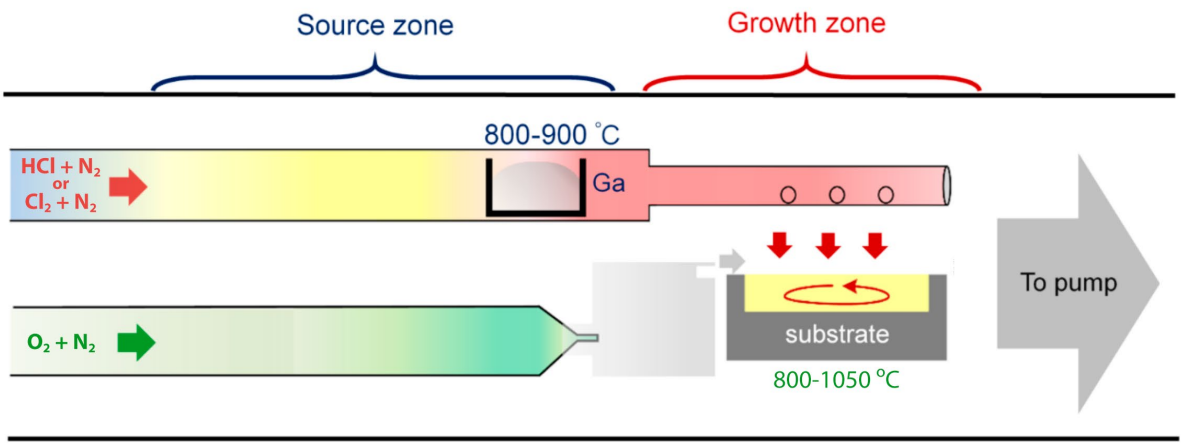

Figure 10: Schematic diagram of the HVPE reactor used for the β–Ga_2O_3 growth. (Adapted from Tasi et al.[40])

As illustrated in **Figure 10**, the HVPE reactor is divided into source zone and growth zone. In the source zone, the source gas, GaCl, is produced by the reaction between high-purity metallic Ga and a chlorine source, HCl or Cl_2, at around 850 °C. At the same, a constant flow of O_2 is introduced in the growth zone as well. Both source gases are carried by a N_2 carrier gas. A substrate is heated at a temperature between 800–1050 °C in the growth zone and, under these source gases, a β-Ga_2O_3 film growths. After reached the desired thickness, the GaCl flow is stopped and the substrate cooled to room temperature.[38,41]

1.2.3. Chemical methods for nanostructures

Usually, chemical synthesis methods are referred to as wet synthesis methods, as they involve the desired material precipitation from a liquid phase containing its precursor. Chemical methods, as opposed to physical methods, do not require (normally) sophisticated and costly equipment, which is a significant benefit on the scale of laboratory research. On an industrial scale, control over materials properties, such as, particle size, morphology and nanostructure are critical properties and chemical methods offer suitable paths to achieve these requirements. Some types of these chemical methods include chemical precipitation, thermal decomposition, solvothermal, microemulsion, and sol-gel processes[42] and two of the most used are addressed in the following chapters.

1.2.3.1. Hydrothermal or solvothermal methods

This technique allows a proper control of materials properties, from its particle size, uniformity, and crystal structure by controlling the type of solvent used, the reaction temperature and pressure, and reagents concentration.[43]

Different types of mediums are employed as solvents, including water, alcohols, and other organic and inorganic solvents. In oppose to physical methods, using solvents provide higher diffusivity of the dissolved ions and, thus, enhances homogeneity of the catalyst obtained.[44] As for the precursors used

for inorganic catalysts synthesis, these are usually salts, such as metal chlorides, nitrates, or acetates. In this method, both the solvent and the precursors are contained in an autoclave (**Figure 11**), usually of stainless steel, coated with a Teflon liner to provide corrosion protection and a chemically inert interior for the reaction.[43]

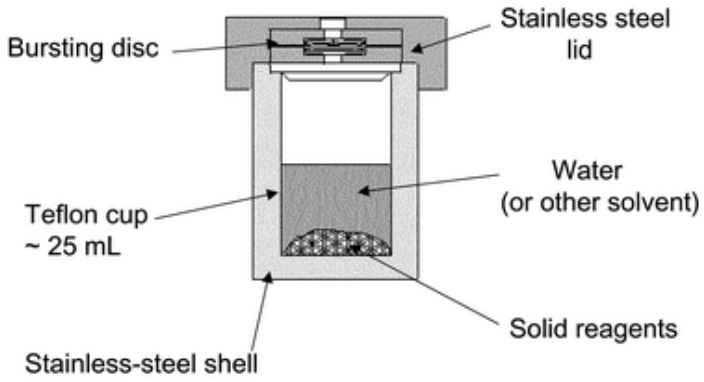

Figure 11: Schematic of a Teflon-lined, stain-less steel autoclave used in solvothermal synthesis. (Reproduced from Walton[45]).

There are some examples of gallium oxide-based catalysts synthesised by this method. Iwamoto et al.[46] prepared and studied a γ-Ga_2O_3-Al_2O_3 catalyst for selective catalytic reduction of NO using methane as a reducing agent. To synthesise this material, they used gallium acetylacetonate and aluminium isopropoxide as precursors, and tried different solvents (such as 1,5-pentanediol, diethylenetriarnine, ethylene glycol, among others) to study their influence in the morphology and catalytic performance. The reactants were placed in an autoclave, heated to 300°C for 2 hours, at a heating rate of 2.5°C/min. Then, after cooling to room temperature, the obtained materials were washed with acetone and centrifuged. The materials prepared in diethylenetriarnine have shown the highest activity for this reaction, with over 90% NO conversion at 500 °C. The γ-Ga_2O_3-Al_2O_3 catalyst prepared by this method presented the best results reported in the literature compared with other methods, like impregnation.[47,48]

On the other hand, Reddy et al.[49] synthesised Ga_2O_3 nanorods to study their morphology and photocatalytic properties. From gallium nitrate dissolved in ammonium hydroxide heated at 95 °C, gallium oxide hydroxide (GaOOH) nanorods were formed. From these, α-Ga_2O_3 and β-Ga_2O_3 phases were obtained from the calcination treatment at 500 and 1000 °C for 3 hours, respectively. Under UV light irradiation, the photodegradation of Rhodamine B solution occurs and after 180 minutes of UV exposure, the α-Ga_2O_3 and β-Ga_2O_3 nanorods photodegeneration efficiency is significant: 62 and 79%, respectively.

1.2.3.2. Sol-gel methods

Between the chemical synthesis methods, sol-gel techniques are widely spread and present several distinct benefits.[50] They are centred on the capacity to generate a solid-state material from a chemically homogenous precursor, allowing the synthesis of inorganic polymers or ceramics from a solution, sometimes with some complexity, the so called 'sol' can undergo transformations to form a nanostructured "gel" network, as it can produce ternary or quaternary oxides, at relatively low temperatures and shorter synthesis time than other methods.[50,51]

A wide variety of precursors can be used, such as metal nitrides, metal alkoxides, metal chlorides, metal acetates, and metal oxides and the versatility of sol-gel methods allows a better particle morphology and size control than other methods. Nevertheless, the homogeneity of the 'sol' may not be enough to detain or control phase segregation throughout the reaction. Hence, this explains the several sol-gel routes tailored to address this issue and other nuances that each case may have.[50] Furthermore, depending on the precursor used, one can divide the sol-gel techniques into three types: the hydrolysis and condensation of metal-alkoxides path, the gelation path when metal-chelates form an aqueous solution, and the polymerizable-complex route (also known as the *Pechini* method).[52]

In 1967, Pechini created and patented its own sol-gel method for the synthesis of homogeneous multicomponent metal oxide materials.[53] His technique based on the transesterification between metal citrate complexes and ethylene glycol is illustrated in **Figure 12**. In this case, a 'sol' is formed when a metal salt is dissolved in water with citric acid and ethylene glycol, thus forming a homogeneous precursor solution. As this solution heats up, the polyesterification begins and the citrate and ethylene glycol form a covalent network. This organic polymeric resign immobilizes the metal complexes and helps to prevent segregation of metal ions particles, thus improving the gel homogeneity. The organic matrix is then eliminated by the calcination at temperatures in the range of 500 to 1000 °C, which generate a pure metal oxide ceramic material.[50,52]

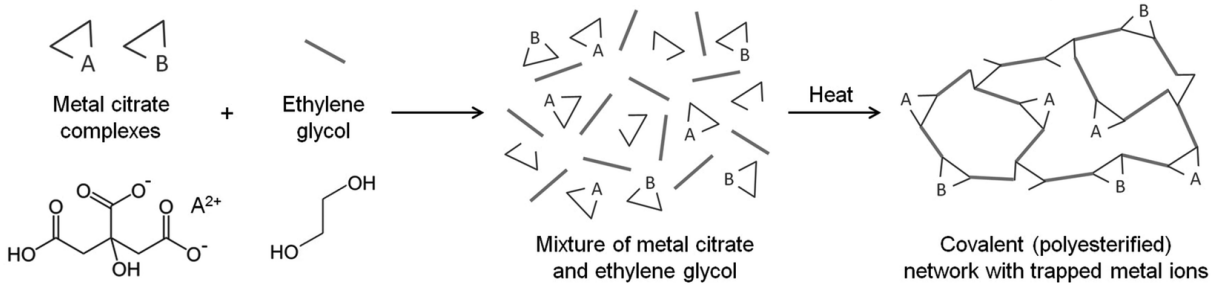

Figure 12: Schematic of the Pechini method for the synthesis of metal-organic gels. (Reproduced from Danks et al.[50])

Shen et al.[54] synthesised nanocrystalline β-Ga_2O_3 using the Pechini process. The precursor used was β-Ga_2O_3 dissolved in diluted hydrochloric acid (HCl) after which citric acid and polyethylene glycol were added and stirred to form a slightly yellow transparent sol. After it dries overnight at 110 °C in an oven, a yellow gel is formed. It was then preheated at 500 °C for 4 hours, grounded and finally calcinated at a range of temperatures between 600 and 1000 °C in air. The material obtained (**Figure 13**) was then characterized and its luminescence properties assessed to be used as a phosphor host material.

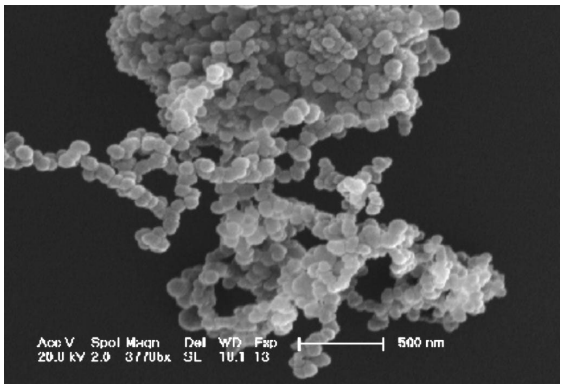

Figure 13: Image of 1.5 atom % Dy^{3+}-doped β-Ga_2O_3 obtained with Field Emission-SEM. (Reproduced from Shen et al.[54])

1.3. Current applications

Having in consideration the high research interest driven by the great potential that Ga_2O_3 has attracted, in this chapter will be presented some examples of fields where there has been major progress in the development of applications for this material. Applications, such as, transparent conducting oxides, flat-panel displays, power and high voltage devices, solar-cell energy conversion, ultraviolet (UV) limiters, gas sensors, antireflection coatings, photodetectors, catalysts, among others, are some examples of the research being developed around gallium oxide.

1.3.1. Gas sensors

Gas sensors are important devices for monitoring gases, either for safety or environmental reasons. This is achieved by exposing a material that has some measurable change in its characteristics when in contact with these gases. As seen in **Table 3**, Ga_2O_3 has been study for various gases detection depending on its crystal structure and working conditions.

Table 3: Examples of Ga_2O_3 gas sensors and performance (Adapted from Pearton et al.[6]).

Sample	Detection gas	Operating temperature (°C)	Detection range
Sputtered, polycrystalline	H_2	400-650	0.5%-3% in Ar
Polycrystalline	CH_4	Up to 700	15%
Nanowires	O_2, CO	100-500	50-500 ppm
Nanocrystallite	NH_3	30	0.5 ppm
Nanobelts	NO_2	25	0.5-1000 ppm

At temperatures higher than 600 °C, Fleischer et al. found that the oxygen vacancy concentration reaches an equilibrium with the partial pressure of atmospheric O_2. The variation of oxygen vacancies upon physisorption of the gases leads to changes in the electric conductivity of the sensor. However, below 600 °C, the electrical conductivity ceases to respond to the variation of oxygen partial pressure.[55] Therefore, Ga_2O_3 sensors can be used as an oxygen sensor in the range 600-1000 °C. For temperatures

between 450 and 600 °C, these sensors are being studied for sensing reducing gases, like CO or H_2.[55,56] Some Ga_2O_3 nanowires have been studied that are able to detect some gases, such as NH_3, NO_2, acetone, methanol, and, to some extent, certain hydrocarbons like toluene.[57,58]

1.3.2. Power and high voltage devices

With the current worldwide urgency to guarantee stable energy supplies and reduced greenhouse gas emissions, there is a need for the development of new technologies able to generate energy and utilize it more efficiently as possible. Some semiconductors, like SiC and GaN, are capable of sustain higher breakdown voltage (V_{br}) and lower conduction loss than Si devices.[16,59] These have already been broadly studied as potential alternative technologies for this purpose. Nevertheless, mass production of power devices with these semiconductors is not workable due to how expensive the production of high-quality substrates is. In this context, the UWBG gallium oxide proves to be a promising material for power device in ultrahigh voltage switching applications, capable of even higher V_{br} and efficiency than SiC and GaN. In addition, it can be synthesized by well-established melt-growth methods using the same relatively low-cost commercial processes used for sapphire substrates manufacturing.[59]

With all this potential in mind, various researchers have studied and developed Ga_2O_3 for power device applications. Among these, Oishi et al. has worked on high-performance Schottky barrier diodes[60], and Higashiwaki et al. has developed MESFETs and MOSFETs.[61,62] However, as discussed in chapter 1.1., the low thermal conductivity and the lack of p-type conductivity are still concerns to be solved and are hindrances to the more broad commercial use of gallium oxide.

1.3.3. Phosphors and electroluminescent devices

Film phosphor materials used in displays applications have been typically made with sulphides. Nevertheless, these have some drawbacks, as they are chemically unstable, especially when in contact with moisture, and its synthesis involves a hydrogen sulphide (H_2S) toxic atmosphere which may be an environmental hazard if leaked.[63]

A material to be a suitable phosphor host material should have a band gap large enough to emit light without absorbing it. Additionally, it should be able to transport efficiently high-energy electrons (>2 eV). This last reason was the major objection for the use of oxide phosphors as a promising substitute to sulphides, since they were thought to be incapable of satisfying that condition, mostly because of their too large band gap (>4 eV).[64,65] However, most recently, many have reported some oxides to be efficient electroluminescent phosphor host materials with important benefits over traditional sulphide phosphors. These advantages are the oxides' chemical inertness, higher thermal stability, longevity, brightness and efficiency.[63–65]

Therefore, gallium oxide, being an UWBD oxide, has drawn the attention of many researchers. When doped with manganese or europium, for instance, gallium oxide emits in the green and red wavelengths, respectively, which are of particular interest in displays.[4,63–65]

1.3.4. Thin film solar-blind UV detectors

The light that reaches Earth's surface has predominantly a wavelength longer than 290 nm because most of the shorter wavelengths are absorbed by the atmosphere, thus protecting all lives from these malicious radiations. Specifically, the stratospheric ozone layer handles the almost complete absorption of wavelengths between 100 and 290 nm. Therefore, it is important that photodetectors operating in this interval have a very high sensitivity to detect weak signals under an intense background of radiations.[6,66] These photodetectors can therefore monitor the ozone layer, along with other applications, such as: intersatellite or underwater communications, biochemical detection, missile guidance or missile detection systems, photolithography, flame detection, automatization, among others.[6,67]

Until recently, most of the research in solar-blind UV detectors was done around WBG and UWBG semiconductors like SiC, AlGaN, AlN, ZnMgO, and diamond. Nevertheless, these materials have drawbacks when it comes to high quality crystal production and their high cost.

Once again, gallium oxide promises to offer a better alternative to these materials for its better chemical and thermal stability, and for promising mass production feasibility.[66,67] For these reasons, Feng et al.[66] and Li et al.[67] have developed β-Ga_2O_3 nanowires that provide large surface-to-volume ratio, which promotes shorter response and decay times in the sensor's performance.

1.3.5. Catalytic applications of gallium oxide

Mainly for the last two decades, various reports have emerged with the increasing research interest around gallium oxide to be used as a catalyst in several chemical reactions such as catalytic combustion, CO oxidation, NOx's selective reduction, oxidative dehydrogenation of ethane, methanol synthesis, among others.[4] The potential seen in this material is explained by its unique structural characteristics of coordinatively unsaturated surface Ga^{3+} cations. These cations are believed to be crucial for Ga_2O_3 catalytic activation role, e.g., hydrocarbon activation in a CO_2 atmosphere, thus, having the potential for methanol production, or methanation of CO_2, for instance.[4,68]

Regarding the catalytic properties of Ga_2O_3, it has been proved that its activity is deeply affected depending on its polymorphism. Several studies have shown that surface acid sites strongly influence the reactivity of the gallium oxide polymorphs. Hence, as pointed out in the previous chapter (**1.1.**), β-Ga_2O_3 being the polymorph with the highest surface Lewis sites density, studies have shown that it is the one with the most activity between them, namely for dehydrogenation of propane to propene[9], decomposition of volatile aromatic[10], and CO_2 hydrogenation to methanol and dimethyl ether.[69]

Since gallium oxide has a UWBG and is transparent up to UV-C radiation, it also shows also a good photocatalytic activity. These processes have advantages over other catalytic reactions, as they can be conducted at room temperature and are cost-effective, efficient, and environmentally friendly.[4,10] Its relatively large over potentials makes it an attractive choice for photoelectrolysis of water, and for the decomposition of volatile aromatic compounds (e.g., toluene, ethylbenzene, and benzene), which according to Hou et al. gallium oxide proved to have higher photocatalytic activity than commercial TiO_2.[10,70,71]

1.4. Challenges in catalytic reactions with Ga_2O_3

As discussed previously, gallium-based materials have been emerged as effective catalysts for some important catalytic reactions, such as selective reduction of NO_x removal using hydrocarbons,[48] dehydration of pentanediol,[72] hydrogenation of CO_2 to methanol,[69,73,74] reverse of water gas shift (RWGS),[75] methanol conversion into hydrocarbons,[76] and dehydrogenation of paraffins to olefins.[77] The last one, in particular dehydrogenation of ethane to ethylene (or ethene), is the focus of this work and it is presented in this chapter.

1.4.1. Oxidative dehydrogenation of ethane

The demand of ethylene (C_2H_4) has been growing over the decades, reaching >200 million metric tons in 2020 and estimating to reach 300 million metric tons by 2025.[78] Ethylene is a key intermediate to produce other value chemicals such as ethylbenzene, acetaldehyde, acetic acid, styrene, ethanol, among others.[79] It can be produced by several methods, e.g., steam cracking, where hydrocarbons and steam are heated to 750–950 ºC, as shown in **Figure 14a**. In Western Europe and Japan, ethylene is obtained mainly from naphtha, gasoil, and condensates. While in North America and Middle East, shale and natural gas are the feedstock mainly used.[80] The market growth predictions for ethylene valorisation and main products derived from it are illustrated in **Figure 14b**.

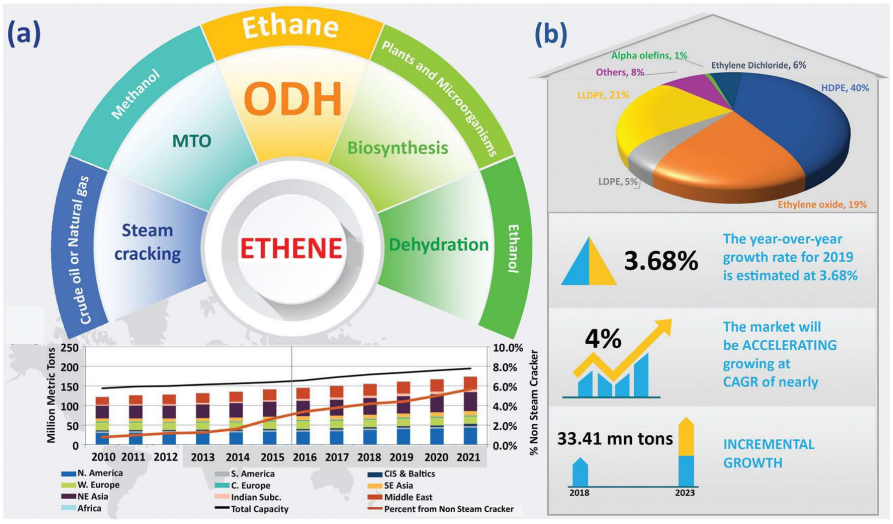

Figure 14: Ethene demand: (a) routes to ethene and its regional production, and (b) main products derived from ethene and predicted ethene market growth (CAGR = Compound annual growth rate). (Reproduced from Najari et al.[80])

On the other hand, ethylene can be also produced through the direct dehydrogenation of ethane (DHE), which is an endothermic reaction and thermodynamically unfavourable (**Equation 1**), that requires high reaction temperatures between 550-700 °C.[81]

$$C_2H_6 \rightleftharpoons C_2H_4 + H_2 \ , \ \Delta H_{298} = 136\ kJ\ mol^{-1} \quad (1)$$

However, the reaction under inert atmosphere tends to form coke, which is a major problem.[82] Thus, the dehydrogenation under oxidative atmosphere (ODHE) is an alternative. This solution, besides decreases the thermodynamic barrier to dehydrogenation, also diminishes coke formation and thus contributes to extend the catalyst lifetime. Nevertheless, an oxidative atmosphere leads to lower ethylene selectivity since ethane combustion to CO_x and H_2O becomes more thermodynamically favourable (**Figure 15**).[82,83]

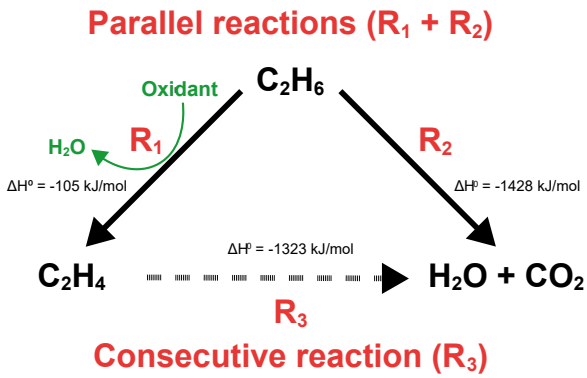

Figure 15: Oxidative dehydrogenation of ethane with side reactions (Adapted from Gärtner et al.[80])

There are three main reactions competing in ODHE: (R_1) the desired ODHE reaction that leads to ethylene formation, (R_2) the total oxidation of ethane to CO_2 and (R_3) the consecutive oxidation to CO_2 of the produced ethylene. This side reactions are the main obstacle for any catalyst tailored for ODHE. Hence, the aim lies in the synthesis of a catalyst able to have a good activity, while suppressing ethane combustion and, subsequently, have a good ethylene selectivity.[83]

1.4.1.1. Role of oxidants in ODHE

Recently, other oxidant agents have been studied to replace O_2, namely N_2O and CO_2.[79] Nakagawa et al. have shown the good efficiency of gallium oxide-based catalysts in the presence of CO_2.[84] Nevertheless, Ga_2O_3 main drawback is his rapidly deactivation, but becomes much more active and stable when together with other oxides.[81]

The use of CO_2 as a "soft oxidant" for ODHE is gaining popularity because it has a number of benefits, including the prevention of over-oxidation of the alkane and improved ethylene selectivity, improved equilibrium conversion by removing hydrogen via the reverse water gas shift reaction (RWGS reaction), decreased coke formation, and mitigation of anthropogenic CO_2 emissions.[85,86]

As for N_2O, being a major green-house gas, its emissions are much lower than CO_2, for instance. Nevertheless, its valorisation as an oxidant in ODHE can be a way to reduce anthropogenic N_2O emissions and to create an environmental added value. Some studies have shown that the replacement of O_2 by N_2O has the potential to increase catalyst's activity and selectivity towards C_2 hydrocarbons like ethylene.[87,88]

1.4.1.2. Types of catalysts for ODHE

The research over ODHE has used, along the past decade, several oxides in the search for a suitable catalyst. As represented in **Table 4**, the list of catalysts studied includes metal oxides, phosphates, and chlorides, and even ternary or quaternary mixed oxides. Within the metal oxides, these can be distributed in three subcategories: reducible oxides (which include transitions metals), non-reducible oxides (which include rare-earth, alkali, alkaline earth, and halide-doped oxides), and noble metal oxides. Gallium oxide has been also considered for this reaction, as Nakagawa et al.[84] work have showed that Ga_2O_3 is a highly active catalyst for the dehydrogenation of ethane. Since then, other studies have reported improved gallium-based catalysts performance and stability.[79,81,89,90]

The choice of catalyst is crucial to a better catalytic performance, as its properties are responsible for all the reactions that take place during the ODHE. These properties, that affect the activity and selectivity of the catalyst in ODHE, are its surface structure and electrical properties, such as, its particle size, morphology, oxidation state, composition. These parameters translate into other important characteristics that control the reaction mechanisms, such as, acid-base properties, the type of oxygen species present in the catalyst's surface, and the catalyst reducibility.[83]

Table 4: The best catalysts for ODHE. (Adapted from Gärtner et al.[80])

Catalyst	Oxidant	T (ºC)	Conv. C_2H_6 (%)	Selectivity (%)	Yield (%)
$YBa_2Cu_3O_{7-0.21}F_{0.16}$	O_2	680	84.1	81.8	68.8
$La_{1.6}Sr_{0.4}CuO_{3.857}X_{0.143}$		660	83.2	76.7	63.8
$Sr_{0.63}Ca_{0.27}CuO_{1.950}X_{0.036}$		680	87.4	74.4	-
$La_{1.85}Sr_{0.15}CuO_{3.930}Cl_{0.053}$		660	82.8	73.2	-
$Bi_2Sr_2CaCU_2O_{7.901}Cl_{0.394}$		680	77.2	76.6	59.1
LiCl-Dy-Mg-O		610	88	87.5	77
$MoV_{0.31}Te_{0.2}Nb_{0.14}O_x$		400	90	87	-
MoVNbTeOx		460	73	85	-
H(Fe)ZSM-5	N_2O	350	62.7	58.4	-
Cr/H-ZSM-5(1900)	CO_2	650	69.5	68.2	-
10%Ce/SBA-15/Al_2O_3/FeCrAl		750	63.9	87.2	55.7
5Cr-10Ce/SBA-15		700	55	96	52.8
5%Cr/SBA-15/Al_2O_3/FeCrAl		750	66.5	95.5	63.5

1.4.1.3. Reaction Mechanisms in ODHE

For a better understanding of ODHE, many have tried to explain its reaction mechanism through kinetic studies. From these, there were developed several kinetic models, such as the Mars-van Krevelen (MvK) model,[80,82,83] the Langmuir–Hinshelwood model,[80,83,91] the Eley Rideal model,[92,93] and combinations between these.[94] The following equations illustrate each step of the MvK (**Equations 2 to 8**) and the Langmuir–Hinshelwood-Hougen-Watson models (**Equations 9 to 19**). (Adapted from Che-Galicia et al.[95])

Mars-van Krevelen model (MvK)

$$C_2H_6 + MO_x \rightarrow C_2H_4 + H_2O + M_{red} \quad (2)$$

$$C_2H_6 + MO_x \rightarrow 2CO_2 + 3H_2O + M_{red} \quad (3)$$

$$C_2H_6 + MO_x \rightarrow 2CO + 3H_2O + M_{red} \quad (4)$$

$$C_2H_4 + MO_x \rightarrow 2CO_2 + 2H_2O + M_{red} \quad (5)$$

$$C_2H_4 + MO_x \rightarrow 2CO + 2H_2O + M_{red} \quad (6)$$

$$C_2H_4 + 4O\text{–}X \leftrightarrow 2CO + 2H_2O\text{–}X + 2X \quad (7)$$

$$M_{red} + mO_2 \rightarrow MO_x \quad (8)$$

Langmuir-Hinshelwood-Hougen-Watson model (LHHW)

$$O_2 + 2S \leftrightarrow 2O\text{–}S \quad (9)$$

$$C_2H_6 + S \leftrightarrow C_2H_6\text{–}S \quad (10)$$

$$C_2H_6\text{–}S + O\text{–}S \rightarrow C_2H_6\text{–}S + H_2O\text{–}S \quad (11)$$

$$C_2H_6\text{–}S + 7O\text{–}S \rightarrow 2CO_2\text{–}S + 3H_2O\text{–}S + 3S \quad (12)$$

$$C_2H_6\text{–}S + 5O\text{–}S \rightarrow 2CO\text{–}S + 3H_2O\text{–}S + S \quad (13)$$

$$C_2H_6\text{–}S + 6O\text{–}S \rightarrow 2CO_2\text{–}S + 3H_2O\text{–}S + 3S \quad (14)$$

$$C_2H_6\text{–}S + 4O\text{–}S \rightarrow 2CO\text{–}S + 3H_2O\text{–}S + S \quad (15)$$

$$C_2H_4\text{–}S \leftrightarrow C_2H_4 + S \quad (16)$$

$$CO_2\text{–}S \leftrightarrow CO_2 + S \quad (17)$$

$$CO\text{–}S \leftrightarrow CO + S \quad (18)$$

$$H_2O\text{–}S \leftrightarrow H_2O + S \quad (19)$$

Essentially, it is largely accepted that the rate-limiting C-H bond cleavage is what triggers the ODHE, and that it is promoted by surface or lattice oxygen species, which have an electrophilic or nucleophilic character, respectively. This first step has been postulated to have many cleavage mechanisms, namely, homolytic, heterolytic, ionic, and synchronous cleavage.[96] Hence, there is not a unique explanation for how ODHE evolves and how it is controlled, being attributed to a different model depending on the type of catalyst used, as **Table 5** illustrates.

Table 5: Postulated reaction mechanisms and respective reactive oxygen species for each type of catalyst. (Reproduced from Najari et al.[83])

Mechanism	Catalyst function	Required properties	Properties to avoid	Oxides fulfilling requirements (ΔH per oxygen atom, kJ mol^{-1})
Group A: redox-mechanism	– Product formation with participation of oxygen from the catalyst – Suppression of total oxidation caused by weakly bound lattice oxygen.	Medium O–Me binding energy: enthalpy of oxide formations (ΔH per oxygen atom in the range −400 to −200 kJ mol^{-1}; reference: V_2O_5 (−310 kJ mol^{-1})		V_2O_5 (−310), Nb_2O_3 (−380) MoO_3 (−248), WO_3 (−281) MnO_2 (−261), Fe_2O_3 (−274) Co_3O_4 (−220), NiO (−240) ZnO (−351), CdO (−260) Ga_2O_3 (−363), In_2O_3 (−309) GeO_2 (−290), SnO_2 (−290)
Group B: activation by adsorbed oxygen	– Activate dioxygen to form chemisorbed oxygen species which activates (gas phase) alkane – Low activity of lattice oxygen toward alkane conversion.	High activity towards oxygen adsorption: high rate of oxygen isotopic exchange.	Low and medium O–Me binding energy: (ΔH per oxygen atom > −400 kJ mol^{-1})	CaO (−636), SrO (−590) Y_2O_3 (−635), La_2O_3 (−598) Gd_2O_3 (−613), CeO_2 (−544) ThO_2 (−613), Nd_2O_3 (−603) Sm_2O_3 (−608)
Group C: activation by lattice oxygen (no redox-mechanism)	– Activation of the alkane by strongly bound lattice oxygen – Low activity towards oxygen adsorption	High O–Me binding energy (ΔH per oxygen atom < −400 kJ mol^{-1})	High rate of oxygen isotopic exchange	BeO (−598), MgO (−602) Al_2O_3 (−559), Sc_2O_3 (−636) ZrO_2 (−550), TiO_2 (−470) SiO_2 (−453), HfO_2 (−559) Ta_2O_3 (−409), B_2O_3 (−418)

For a lot of reducible transition metals and gallium oxide, that belong to Group A, these follow a redox mechanism, like the MvK. As for the Group B, it is composed of rare-earth and alkali oxides. While in Group C are the least reducible oxides, which are harder to activate for ODHE.

In the case of Ga_2O_3, belonging to Group A and following the MvK mechanism, the ethane, and the lattice oxygens of gallium oxide react, leading to the catalyst surface reduction. Following which, the

oxidant gas present re-oxidates it. Therefore, the type of oxygen at the catalyst surface has the most importance to the initial catalytic activation. The ethane C-H bond requires an affinity between the molecule and the catalyst surface, meaning that acid-base properties play a crucial rule in the process.

The charge and radius of a cation influence the acid-base properties of the metal oxides surface. For instance, high valent cations are correlated with electrophilic oxygens, which result in more acidic oxides, while low valent cations are accompanied by nucleophilic oxygens that are associated with more basic oxides. These different oxygen species influence the catalyst activity and selectivity. The electrophilic oxygens adsorbed at the catalyst surface are usually seen as responsible for promoting ethane combustion, whereas the nucleophilic lattice oxygens are linked to selective oxidation enhancement.[83]

1.4.1.4. Future prospects and challenges

Although there are still aspects to address before industrial adoption, there are already catalysts with very good performance under laboratory conditions for ODHE.[97–100] Important aspects like catalyst lifetime, the reactor design, scalability, and optimization of the processes still need to be enhanced, as well as the possibility to use commercially impure hydrocarbon feedstocks still needs to be addressed.[83,101]

On the other hand, emerging technologies are opening new possibilities. For instance, Zhang et al.[102] are studying a novel approach for C-H bond activation promoted by solar energy to allow ODHE (**Figure 16a**). Other study is working on a way to activate the catalyst without heating the reactive gas using microwave heating, leading to a more efficient energy usage, (**Figure 16b**).[103] Lastly, James et al.[104] are developing a fuel cell in which ethane and the oxidant feed are separated by a membrane. With this approach, the aim is to minimize the risk of explosion in autothermal reactor systems (**Figure 16c**).

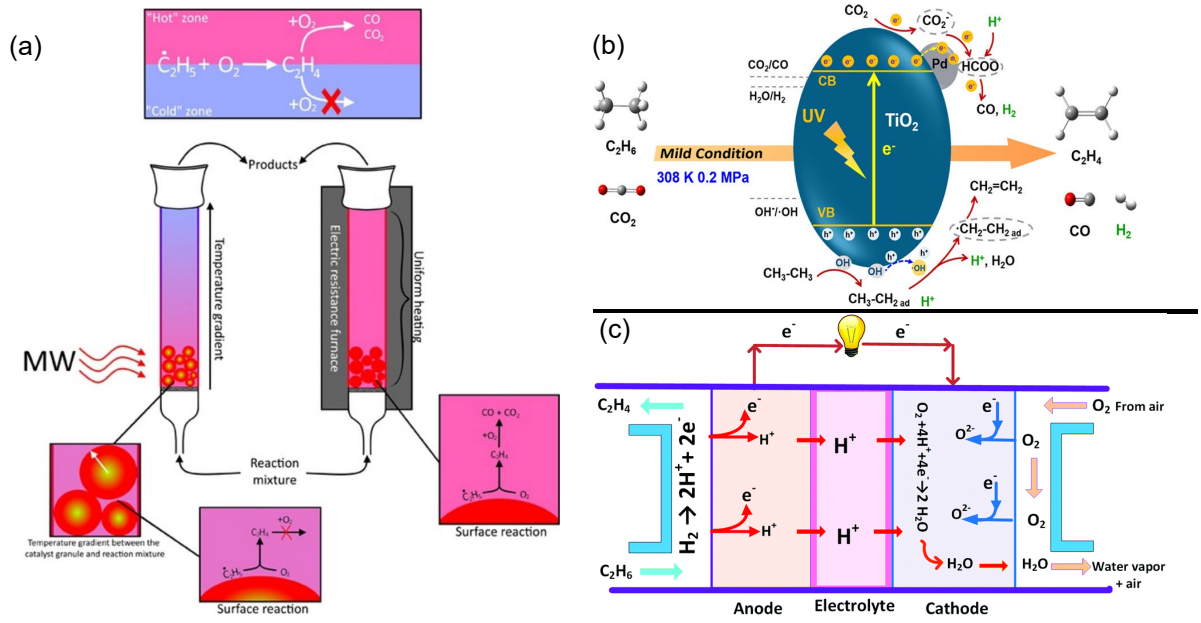

Figure 16: Schematics of (a) microwave heating set-up for ODHE (Reproduced from Bolotov et al.[103]), (b) photocatalytic ODHE (Reproduced from Zhang et al.[102]), and (c) fuel cell membrane reactor (Reproduced from Najari et al.[83]).

As for the gallium oxide-based catalysts, they have been pointed out as a promising solution for the ODHE, with high activity and selectivity in the presence of CO_2.[79,84] However, these catalyst seem to deactivate quickly and their stability is affected by reaction time.[81,90] For these reason, some reports have shown that its performance can be enhanced when mixed with other oxides. Hence, the study of a proper system that can take full advantage of Ga_2O_3 potential is still at early stages. Zhao et al.[105] have demonstrated that the addition of CeO_2 increases the oxygen vacancies on Ga_2O_3, while Fe, Cu, Co, Mo, and V are said to promote redox reactions, which may have an impact on ODHE.[83]

1.5. Objectives

Taking all this information into account, this work aims were the development and characterization of gallium oxide-based materials and to test them as catalysts for the ODHE. For such, Ga_2O_3 and CeO_2 catalysts, with different ratios, were synthesized by the electrospinning technique and by the epoxide addition method. Moreover, copper oxide (CuO) was supported on Ga_2O_3, CeO_2 and Ga-Ce bimetallic oxide with a 1:1 molar ratio to study its influence on this reaction. All the catalysts were characterized by Scanning Electron Microscopy and Energy Dispersive Spectroscopy (SEM-EDS), Powder X-Ray Diffraction (Powder-XRD), nitrogen adsorption−desorption Brunauer−Emmett−Teller (BET) method, temperature programmed reduction under hydrogen (H_2-TPR) and their acid-base properties were measured using a model reaction (dehydrogenation/dehydration of 2-propanol). Furthermore, the study of its catalytic behaviour in the dehydrogenation of ethane, aiming to the production of value-added chemicals such as ethylene, with possible practical applications in the petrochemical industry was the major objective of this master thesis. Additionally, the effect of different oxidants used for this reaction, like N_2O or CO_2, has been considered to replace O_2. This have several benefits, namely the valorisation of anthropogenic pollutants as oxidants in ODHE can be a way to reduce green-house gases emissions and to create an environmental added value for such gaseous pollutants.

2. Experimental methods

2.1. Synthesis of gallium-based catalysts

In this work, the aim was to obtain Ga_2O_3 nanostructures with the highest specific surface area possible, considering that is an important parameter in catalysis, and to study the effect of a co-metal, it was chosen cerium, on its catalytic behaviour. For this reason, three molar ratios of Ga_2O_3 and CeO_2 were prepared, namely Ga_2O_3-$6CeO_2$, Ga_2O_3-$2CeO_2$, $3Ga_2O_3$-$2CeO_2$ — which, from now on, will be referred as Ga:Ce (1:3), (1:1), and (3:1), respectively. Moreover, aiming to study the morphology influence on their performance, two synthesis methods were employed: the epoxide addition method, to produce aerogels, and the electrospinning technique, which leads to the formation of fibres. Hence, in this chapter, these techniques are explained in detail.

2.1.1. Epoxide addition method

Open-cell foams, such as aerogels, have awakened a great research interest, especially for catalytic purposes, due to their unique properties. They provide low density and high surface area materials, with a nanostructure, which have the potential to increase a catalyst activity compared to a bulk or other morphologies counterparts.[106]

Initially, metal oxide aerogels were synthesized with metal alkoxides ($M(OR)_x$) precursors, which under a variety of conditions promptly react. However, since alkoxides might be costly, challenging to synthesize and unstable for most elements, other approach started to be employed. This new method, designated as epoxide addition method (or epoxide-initiated gelation), allow a broader range of compositions. This way, organic epoxides act as initiators for the sol-gel polymerization of inorganic metal salts dissolved in aqueous or alcoholic media.[106,107] **Figure 17** illustrates the reactions that take place in this mechanism.

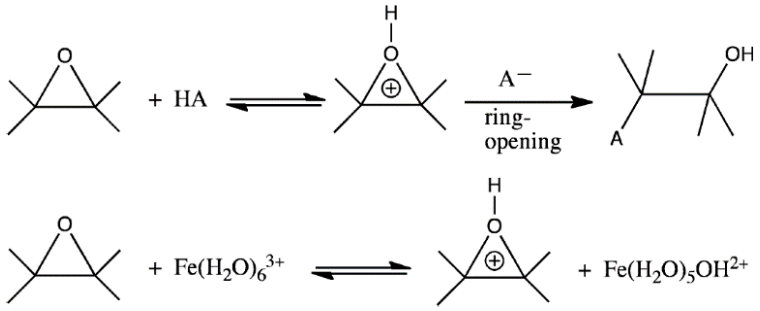

Figure 17: Protonation and ring opening of an epoxide in the presence of an acid. (Adapted from Baumann et al.[106])

Normally, sol-gel processes have three stages. Firstly, a colloid mixture is formed by dissolving metal salts, such as metal nitrates or halides, in an aqueous or alcoholic media. Then, an organic epoxide, like propylene oxide, is added to start the gelation phase. The epoxide drives the hydrolysis and condensation of hydrated metal species by acting as an acid scavenger in the sol-gel process. The

last step allows the formation of the aerogel by drying the wet gel using, for instance, the organic solvent sublimation drying (OSSD) – which consists of using mixtures of acetonitrile and ethanol at 50, 80, and 100% (v/v), respectively, for each concentration a 24 hours period at 50 °C.[106] The steps of this method are summarized in **Figure 18**.

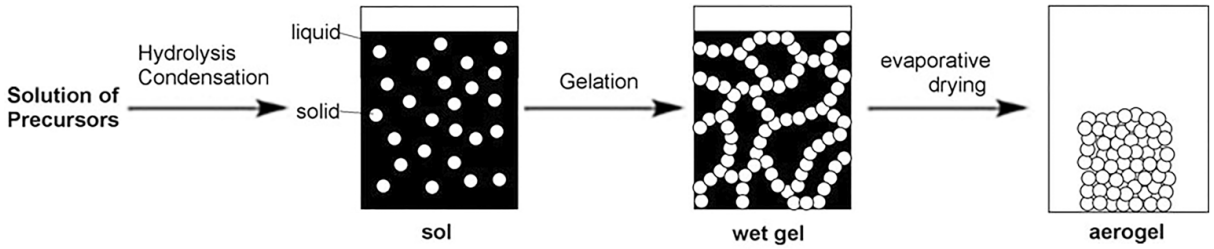

Figure 18: Scheme of the epoxide addition method (Adapted from Baumann et al.[106]).

This method allows the preparation of aerogels using salts as precursors, namely: cerium chloride heptahydrate and gallium nitrate hydrate (Aldrich chemistry, 99%; ThermoFisher, 99.9% purity, respectively) that were completely dissolved in absolute ethanol (Fisher Chemical ≥ 99.8%), in the pretended ratios, Ga:Ce (1:3), (1:1), and (1:3), at room temperature. Following which, propylene oxide (Acros Organics, 99,5% purity) was slowly added to the solution so that the ratio between moles of metals and propylene oxide was 1:9. The solution was stirred for another five minutes, after which it was allowed to stand until a gel had formed. Afterwards the gel was aged in absolute ethanol and sealed in its container for 48 hours at 50 °C, following which it was dried according to the OSSD at the same temperature. Finally, the aerogel was calcined at 800 °C for 2 hours, using a heating rate of 1 °C/minute, and grounded to achieve a grain size of 200 mesh (75 µm).

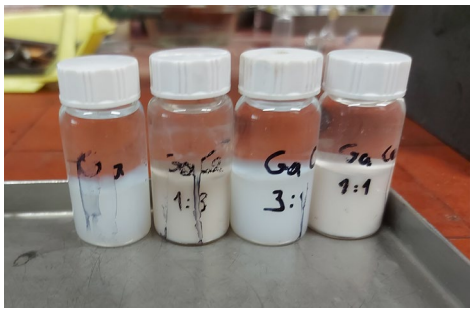

Figure 19: Gel samples before dried with OSSD method.

2.1.2. Electrospinning technique

The catalyst morphology is of great importance to its performance.[108] One of the most interesting morphologies are the nanofibres and electrospinning is a versatile technique that allows the synthesis of fibres in many configurations and diameters. This method consists of an electrohydrodynamic

process, where a liquid droplet generates a jet when electrified, making it stretch and elongate, forming a fibre.[109] Ga_2O_3 fibres were already obtained by this technique.[110–112]

What makes a solution suitable for electrospinning is determined by the sol-gel precursor and the carrier polymer used, its viscosity, and its electrical conductivity. As precursors, the most frequently utilized are metal salts, like alkoxides, nitrates, acetates, chlorides, and sulphates. While the most common carrier polymer is polyvinylpyrrolidone (PVP) for its high solubility in ethanol and water and suited compatibility with several sol-gel precursors. The viscosity can be manipulated by adjusting either the precursor or the carrier concentration.

The setup needed for this technique depends on the production volume intended, but regardless, **Figure 20** exemplifies the components normally required. They include a high-voltage power supply, either direct current (DC) or alternating current (AC), a syringe pump, and a conductive collector, that can be an aluminium foil, for example.

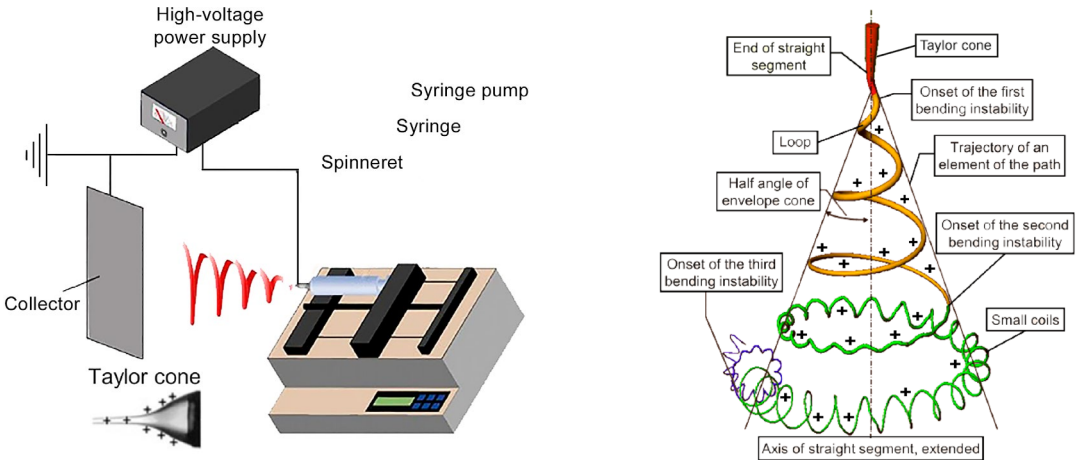

Figure 20: Diagram of (a) a typical electrospinning set-up and (b) the electrospun jet path. (Adapted from Xue et al.[109])

The process starts when a current is applied, a charged jet is released from the electrified droplet towards the target, allowing the formation of solid fibres that are then deposited on the grounded collector as a result of the jet's rapid solidification upon being stretched to very small diameters.[109]

In this work, the solutions were prepared by dissolving 42wt.% of polyvinylpyrrolidone (PVP) in 50 mL absolute ethanol (Fisher Chemical ≥ 99.8%) followed by the addition of 4 mmol of cerium and gallium (III) nitrates (Aldrich, 99.9 % purity, hexahydrate; ThermoFisher, 99.9% purity, respectively) in three ratios – Ga:Ce (1:3), (1:1), and (1:3). These solutions were collected in a syringe with a ≈0.9 mm interior diameter stainless steel flat-tip needle and pumped continuously by a syringe pump (KW scientific) at a rate of 1 mL/h with an electric field of 16 kV applied between the syringe tip needle and a collector, in this case, a grounded aluminium foil placed at 10 cm from the needle tip, as seen in **Figure 21**. Finally, the electrospun material was calcined at 800 °C for 2 hours, under a heating rate of 1 °C/min.

(a) (b)

Figure 21: Pictures of (a) the electrospinning set-up used; (b) fibres after calcination at 800 °C.

2.1.3. Incipient wetness impregnation

Taking advantage of the high surface area given by the support, impregnation techniques have a crucial role to improve the performance and stability of catalysts active phases. In this way, it is possible to prepare active heterogeneous catalysts using a cheaper support and smaller quantities of an active material.[113,114]

In this work, Ga_2O_3, CeO_2 and Ga:Ce (1:1) aerogels were used as supports for the impregnation of copper oxide. For this, copper (II) nitrate hexahydrate (AlfaAesar, 98% purity) was dissolved in distilled water, so that the equivalent mass of copper represented 25% of the total mass of the impregnated catalyst. Then, the solution was poured into a crucible containing the support and, under constant stirring, left to dry at 60 °C, as exemplified in **Figure 22**. After the water has completely evaporated, the catalyst was calcined at 500 °C for 2 hours under a heating rate of 1 °C/min, and grounded to achieve a grain size of 200 mesh (75 µm).

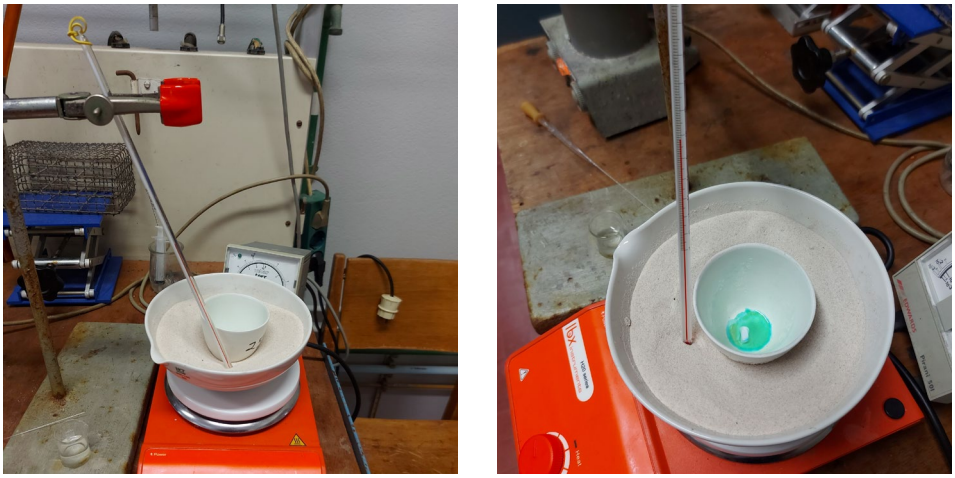

Figure 22: Incipient wetness impregnation set-up.

2.2. Characterization methods

After the synthesis of the catalysts, a complete characterization of their physical and chemical properties is essential to a better understanding of the role of each element and structure of each catalyst in the reaction studied in the following chapter. In this regard, this chapter will briefly describe each one of the characterization methods employed.

2.2.1. Scanning Electron Microscopy and Energy Dispersive Spectroscopy (SEM/EDS)

Towards a better understanding of the morphology and microstructure of a sample, between the various techniques available, one of the most broadly used is the Scanning Electron Microscope (SEM). This technique is relatively easy to operate and provides fast results. The images obtained can have a magnification between 20 and 100 000 times. Moreover, SEM is normally accoupled with Energy Dispersive Spectroscopy (EDS) for a semi-quantitative surface analysis.

To generate an image, a focused electron beam (1-40 kV) bombards a single point at a time on the surface of a specimen. These electron beams are emitted from an electron gun and guided through a series of electromagnetic lenses and apertures to hit the sample's surface as a condensed probe. It's the size of the electron probe that controls the SEM resolution. The electrons bombardment on the surface sample generates either elastic or inelastic electron scattering. The first produces Backscattered Electrons (BSE), which are incident electrons scattered by the sample and provide an elemental composition contrast. While the last gives Secondary Electrons (SE), which are electrons ejected from atoms at the surface sample and are used to obtain topographic contrast. These SE are also responsible for generating characteristic X-rays emitted by the sample atoms. This radiation allows the identification of the chemical elements present in the sample using EDS.[115]

The samples surface morphology was recorded using a benchtop SEM Phenom ProX G6 with CsB6 filament (**Figure 23**), operating at 15 keV and 74 μA and the surface chemical composition was determined by EDS using a B-U Bruker Quantax 400 EDS-SDD system.

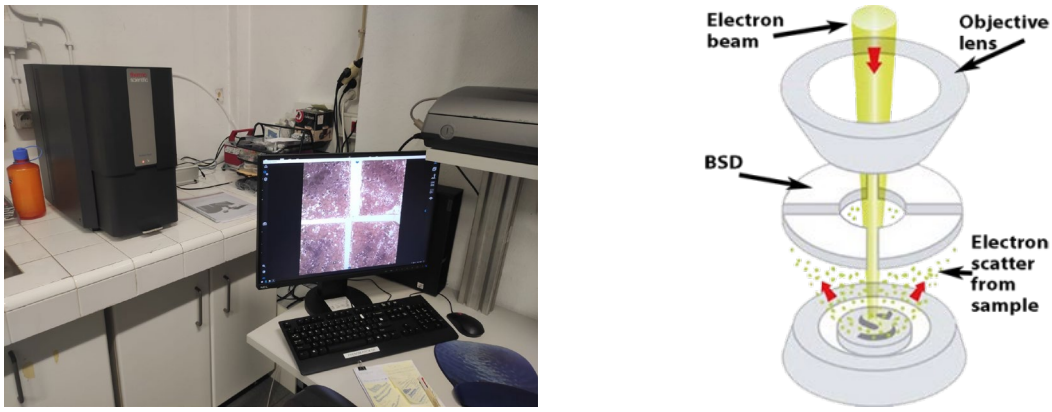

(a) (b)

Figure 23: Scanning electronic microscope: (a) Phenom Pro Desktop SEM from IST – Microlab. (b) Schematic of a backscattered detector (BSD) for a SEM (Reproduced from ref.[116]).

2.2.2. Powder X-ray diffraction

During the catalytic studies, the catalysts are subject to conditions, like high temperatures and pressure, which are prompt to alter their entire structure and morphology. Therefore, it is of foremost importance to study the crystal structure before and after the various treatments and reactions where it is tested. For this reason, X-ray diffraction (XRD) is a powerful technique employed to confirm the main crystalline phases, determine the lattice parameters of these materials, and possibly identify their modifications after treatments and catalytic tests.

X-rays are electromagnetic waves with a wavelength small enough, on the order of 1 Å, to interact with the crystal structure. Thus, XRD consists of the measurement of this radiation intensity that reaches a detector, scattered from the sample atom's electrons. These waves arrive to a detector with different phase shifts, thus, providing information about the relative position of the atoms.

To interpret the data collected in XRD and determine the crystal structure of a sample, the Bragg's equation is used. This equation (**20**) provides an explanation on how the peaks observed in XRD patterns are related to sets of lattice planes.

$$n\lambda = 2d_{hkl} \cdot \sin\theta \tag{20}$$

Hence, although Bragg's law was thought to explain light reflection by a mirror, X-rays can also be treated as light, with a specific wavelength (λ) being specularly reflected at the lattice planes. These planes are usually identified by the index triplet *hkl*, known by Miller indices. When crystallographic planes share the same indices, they are parallel and separated by a constant distance, d_{hkl}. As X-rays have higher energy than visible light, these can penetrate inside the material's surface and be reflected by thousands of parallel planes, which may lead to superposition between them. As a result, constructive or destructive interference occurs depending on the phase shifts, n, of each scattered wave (**Figure 24**). Such signal interferences, which occur at specific diffraction angles (2θ), arrive to the detector and are registered as peaks.[117]

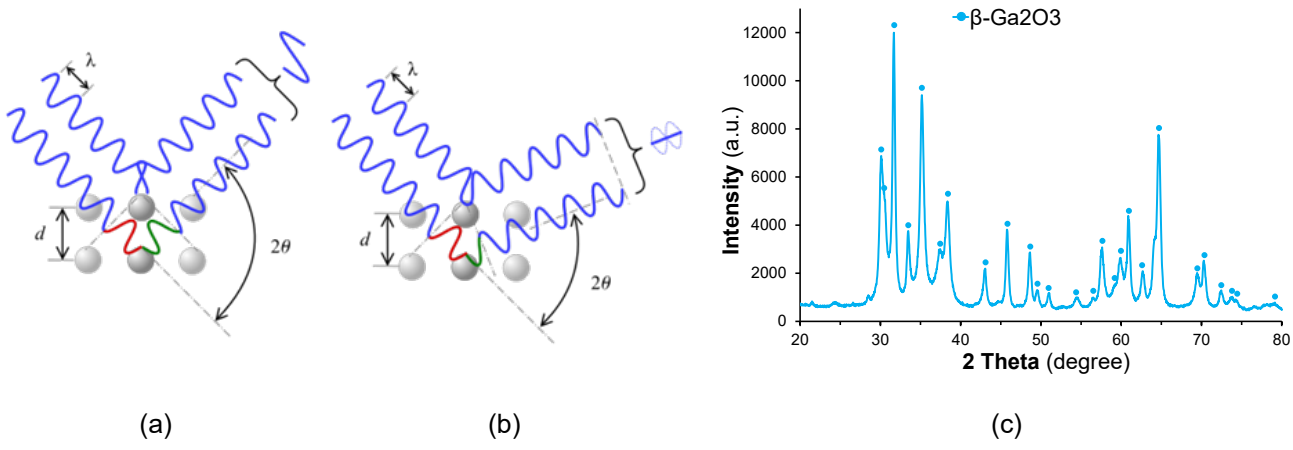

(a) (b) (c)

Figure 24: Powder X-ray diffraction: Scheme of (a) constructive or (b) destructive interference caused by different phase shifts between two scattered waves, and (c) example of X-ray diffractogram from the Ga_2O_3 aerogel.

Another useful information that is possible to extract from the XRD peaks is the mean crystallite size of the samples, meaning it is possible to measure an approximation size of the homogeneous domains on the sample's surface that give rise to coherent diffraction, which are represented by the peaks themselves. This concept was first introduced by Scherrer[118] were he relates this with the half width of a peak, *β*, which corresponds to the range of *2θ* in which the peaks intensity is larger or equal to half of its hight, in order words, the FWHM, full width at half maximum. From this, the crystallite size, D, can be deduced from equation **21**,

$$D = \frac{K\lambda}{\beta \cos\theta} \tag{21}$$

Where K is the Scherrer constant, which is commonly accepted to be 0.9, and *θ* is the Bragg angle.[119]

The crystalline structure of the synthesized materials was analysed using a D2Phaser Bruker diffractometer (Cu, kα monochromatic radiation, λ=1.5406 Å) with the operational settings for all scans being voltage=30kV voltage, current=10mA, and 2θ scan range between 20 – 80° using a step size of 0.03° with a time per step of 3.5 s.

2.2.3. Specific surface area measurement by the BET method

The Brunauer-Emmett-Teller (BET) method is commonly applied to calculate specific surface areas on the basis of nitrogen adsorption isotherm measurements at 77 K. Typically, data from the 0.05 to 0.3 relative pressure range are employed.[120]

Nitrogen physisorption, being weak and reversible, forms layers at the surface of the catalyst. Hence, BET theory assumes that by considering the volume of gas needed to create a monolayer at the catalyst surface, it is possible to estimate the area covered. Specific surface area (SSA) can be, therefore, calculated from the following equation:[121]

$$SSA = \frac{V_m \cdot N_A \cdot a_m}{v_m \cdot m_s} \tag{22}$$

Where V_m is the volume of the monolayer, N_A is the Avogadro's number, a_m is the cross-section area of one adsorbed N_2 molecule, v_m is the volume of one mole of adsorbed N_2, and m_s is the mass of the catalyst.

Figure 25: BET set-up in a Micrometrics ChemiSorb 2720 – ChemiSoft TPx system.

In this work, the measurements (monopoint) were conducted using a Micrometrics ChemiSorb 2720 – ChemiSoft TPx system (**Figure 25**). Under a flux of 30% N_2 in helium ($P/P_0 = 0.3$) of 20 mL/min, the catalysts were submitted to 3 cycles of N_2 adsorption (using liquid nitrogen, negative peaks) and desorption (when the liquid nitrogen is removed and the sample is allowed to return to room temperature, positive peaks), as **Figure 26** illustrates.

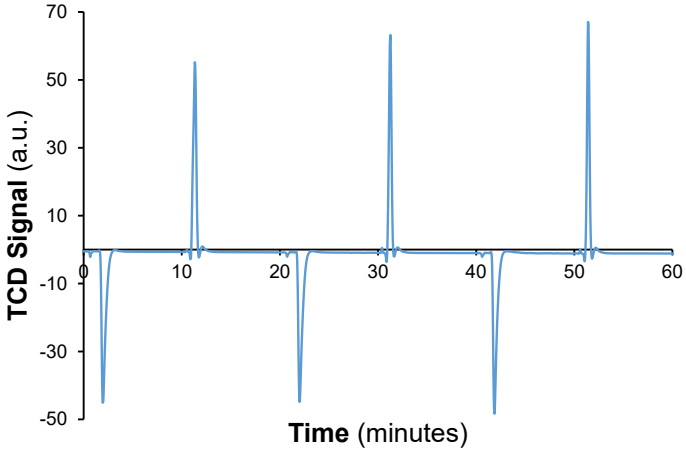

Figure 26: Typical BET measurement.

A downstream thermal conductivity detector (TCD), integrated in the Micrometrics ChemiSorb 2720 – ChemiSoft TPx system, monitors the gas stream's and allows nitrogen absorption/desorption quantifications through a calibration curve (**Figure 27**), which has been previously obtained by measuring the detector's response to the addition of known N_2 volumes where *x* is the desorption peak areas and *y* the volume of N2 adsorbed.

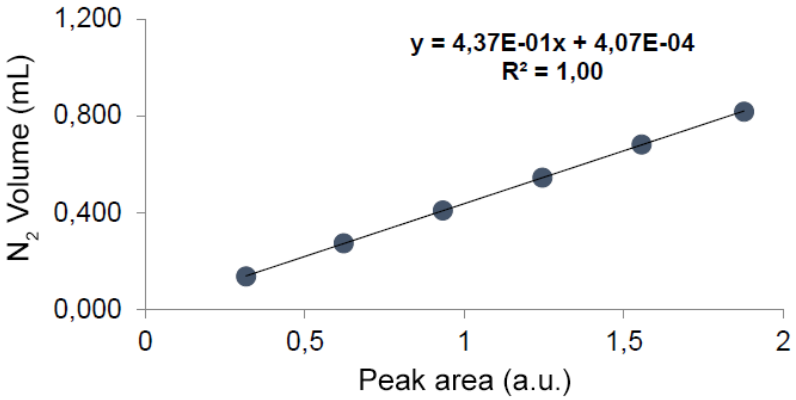

Figure 27: Calibration curve of N_2 consumption.

The specific surface areas measured by the BET method are presented in **Table 6**. They clearly illustrate the differences between the two morphologies synthesized, fibres and powders. Comparing the fibres diameters, measured in **Table 7**, it is noticeable that the increase in Ga content lowers the diameters of the fibres and, in turn, as expected, increases the SSA. A similar tendency is visible for the aerogels, where Ga content favours the increase of SSA but Ga_2O_3 and CeO_2, when mixed, appear to have lower SSA than their pure counterparts. The Cu supported materials have a slightly higher SSA than their respective supports, except the $25_{wt.\%}Cu/Ga_2O_3$.

Table 6: Specific surface areas measured by the BET method.

Catalyst		Specific Surface Area (m^2/g)
Fibres		
Ga:Ce	1:3	15.9 ± 2.9
	1:1	23.8 ± 3.0
	3:1	29.1 ± 4.2
Aerogels		
CeO_2		11.8 ± 0.7
Ga:Ce	1:3	3.5 ± 0.2
	1:1	6.8 ± 0.8
	3:1	7.4 ± 0.7
Ga_2O_3		25.5 ± 0.7
Impregnated		
25wt.%Cu/Ga:Ce		8.6 ± 0.1
25wt.%Cu/CeO_2		12.1 ± 0.7
25wt.%Cu/Ga_2O_3		18.8 ± 0.9

2.2.4. Temperature Programmed Reduction (H_2–TPR)

The catalytic behaviour can be affected by a number of significant parameters, one of which is the reducibility of the catalysts. Thus, temperature programmed reduction (TPR) studies were performed using the Micrometrics ChemiSorb 2720 – ChemiSoft TPx system, a specific Micromeritics quartz type U reactor, and a mixture of 10% H_2 in argon, total flow of 20 mL/min, at a heating rate of 10 ºC/min from room temperature to 1050 °C (**Figure 28**). Just like in the case of the BET measurement, a TCD monitors the gas stream's quantification. The sample weight use was established between 10 to 20 mg.

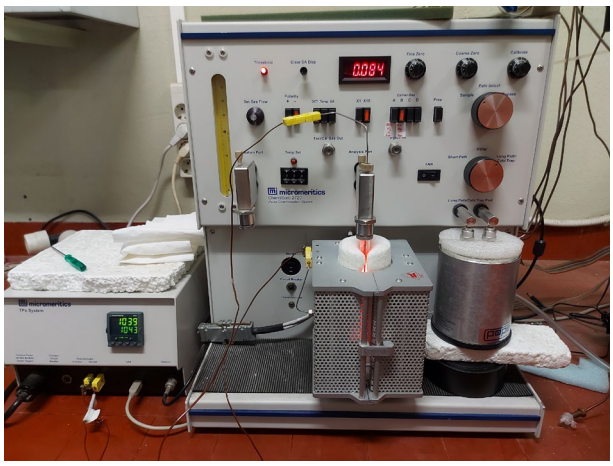

Figure 28: H_2-TPR set-up in a Micrometrics ChemiSorb 2720 – ChemiSoft TPx system.

For the calibration of the detector response, measurements were made using known quantities of NiO powder (Aldrich, 99.9995 purity) to assess known quantitative H_2 consumptions (**Figure 29**) and by integrating the experimental H_2-TPR profiles, to access the corresponding areas (**Equation 23**).

$$NiO + H_2 \rightarrow Ni + H_2O,\ H_2 - uptakes\ (mol) = 4.9313 \times 10^{-6} \times peak\ area \quad (23)$$

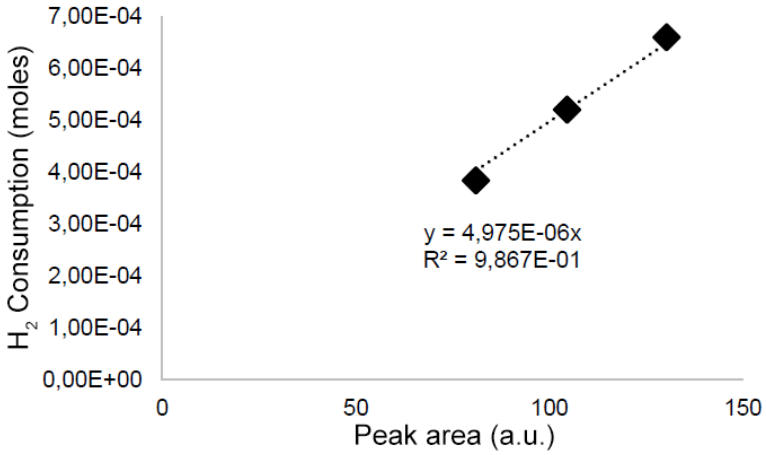

Figure 29: Calibration curve for H_2 consumption in a TPR, obtained from a reference of nickel oxide.

By analysing each H_2-TPR profile (**Figure 30**), it is possible to do study the reactions undertaking during the treatment and, thus, make a qualitative and quantitative analysis. A qualitative analysis can be done by understanding each reduction step and correlating the different peaks to them. Therefore, a maximum reduction temperature is identified for each reduction step of the catalysts. While through the monitorization of the H_2 consumption related to each stage, a quantitative analysis allows to verify the theoretical and qualitative presumptions of the whole process.

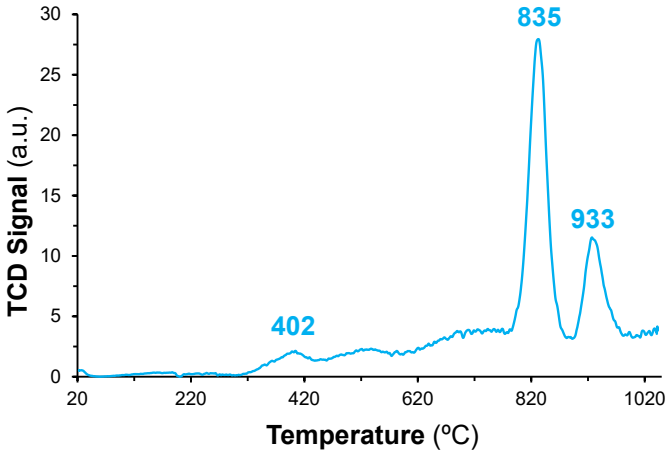

Figure 30: H_2-TPR profile of Ga-Ce (1:1) bimetallic oxide aerogel calcinated at 800°C.

From the calibration measurements with NiO powder (**Equation 23**), it is feasible to assess the quantitative H_2 consumption by the integration of the experimental H_2-TPR profiles (**Figure 30**).

2.2.5. Acid-Base properties

In order to assess the acid-base properties of the catalysts, studies using a model reaction, the dehydrogenation/dehydration of 2-propanol (isopropanol) were undertaken. Two main competitive reactions may occur, the dehydrogenation of isopropanol leading to the production of acetone and hydrogen, and the dehydration of isopropanol, where propene and water are produced (**Figure 31**). Evaluating the quantity produced of propene or acetone, it is possible to understand the acid-base properties of a catalyst, and how many acid or basic sites there are at its surface, its distribution and strength.[122,123]

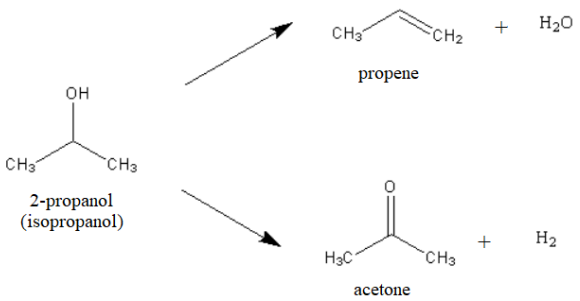

Figure 31: Dehydrogenation/dehydration of 2-propanol reaction scheme.

The tests were performed in a fixed-bed U-shaped Pyrex reactor at atmospheric pressure, in a temperature range between 175 to 275 °C. The reaction was conducted under a continuous flow of a mixture of 0.25% (v/v) of isopropanol in air N_2/O_2:80/20 (v/v) (Air Liquide, 99.9995% purity) with a Gas Hourly Space Velocity (GHSV) of 1012 mL /g_{cat}·h and a O_2 to isopropanol molar ratio of 10. Gas chromatography was used to analyse the composition of the reactor outlet gas. An Agilent 7280D chromatograph equipped with a flame ionization detector (FID) and a capillary column HP_PLOT_U, L = 25 m, ID = 0.32 mm was used for such purpose. **Figure 32** shows the experimental set-up.

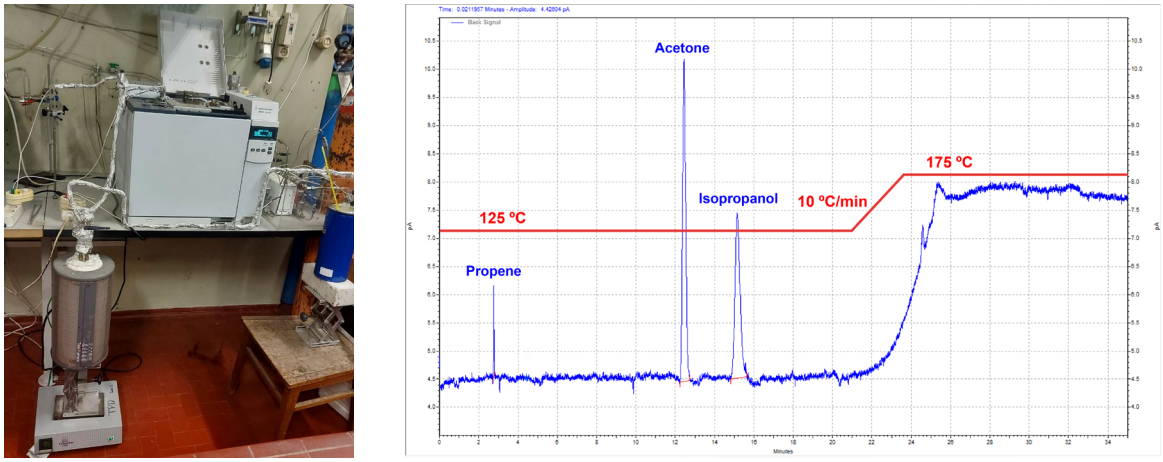

(a) (b)

Figure 32: Set-up used during the dehydrogenation/dehydration of 2-propanol (a) reaction with the Agilent 7280D GC. (b) Typical chromatogram (blue line) and heating rate (red line).

The values reported in this work represent the steady state activities after 1 h on stream at each temperature and the activity defined as the volume of isopropanol converted per gram of catalyst per hour (mL/g_{cat}.h). Isopropanol conversion and acetone and propene selectivity's were calculated following the equations **24** to **26**. **Equation 27** represents the ratio between the selectivity of acetone (νA) and propene (νP), used to build a relative scale of basicity.

$$Isopropanol\ conversion\ (\%) = \frac{[acetone] + [propene]}{[acetone] + [propene] + [isopropanol]} \times 100 \quad (24)$$

$$Acetone\ selectivity\ (\%) = \frac{[acetone]}{[acetone] + [propene]} \times 100 \quad (25)$$

$$Propene\ selectivity\ (\%) = \frac{[propene]}{[acetone] + [propene]} \times 100 \quad (26)$$

$$relative\ basicity\ = \frac{\nu A}{\nu P} = \frac{acetone\ selectivity\ (\%)}{propene\ selectivity\ (\%)} \quad (27)$$

2.3. Catalytic studies – Oxidative Dehydrogenation of Ethane

ODHE studies were conducted with different oxidants (O_2, N_2O and CO_2), at atmospheric pressure, in the temperature range 400-700 ºC. The catalysts were placed in a U-shaped fixed bed quartz plug-flow reactor, which in turn was inserted into a tubular oven. The reaction temperature was controlled by a thermocouple placed near the catalytic bed. For the reaction itself, a gas mixture with C_2H_6, oxidant and He was used, molar ratio Oxidant/C_2H_6 of 10, together with a Gas Hourly Space Velocity (GHSV) of 7500 mL C_2H_6/g of catalyst per hour (mL $C_2H_6/g_{cat}\cdot h$) and, to prevent any diffusional problems, an optimized catalyst mass between 10-20 mg was used. To control each gas flows, mass flows controllers (Aalborg series A) were used. The reaction was followed by chromatography using a gas chromatograph, the Agilent 4890D GC, equipped with a TCD and a Restek ShinCarbon ST column (L=2.0 m, Φ=1/8 in, ID=1mm, 100/200 mesh), the composition of the reactor outlet gas was analysed online. The set-up used is shown in **Figure 33a**, and **33b** illustrates a typical chromatogram obtained and the heating rate used during the catalytic tests.

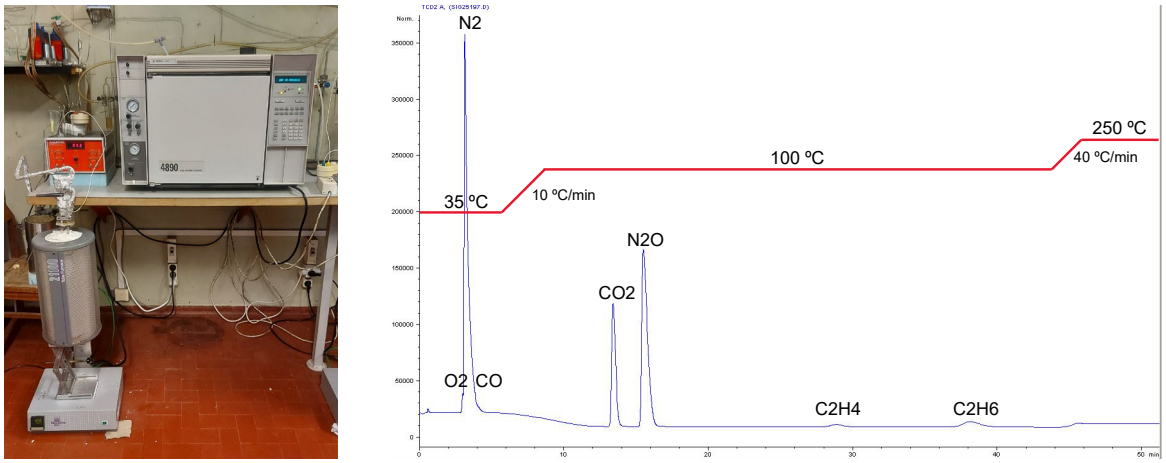

(a) (b)

Figure 33: Catalytic studies: (a) Set-up used for ODHE studies with the Agilent 4890D GC and (b) Typical chromatogram obtained from Agilent 4890D GC and the representation (red line) of the heating rate during the reaction.

From the peak areas measured in a chromatogram and from the calibration curve equations, it is possible to quantify the evolution of each reactant and product during the time of a reaction. The catalytic activity, namely the C_2H_6 conversion, was evaluated employing the equations **28-33**. All reported results represent catalytic activity values after 1 hour of reaction.

$$C_2H_6\ conversion\ (\%) = \frac{[CO] + [CO_2] + [CH_4] + [C_2H_4]}{[CO] + [CO_2] + [CH_4] + [C_2H_4] + [C_2H_6]} \times 100 \quad (28)$$

$$CO\ selectivity\ (\%) = \frac{[CO]}{[CO] + [CO_2] + [CH_4] + [C_2H_4] + [C_2H_6]} \times 100 \quad (29)$$

$$CH_4\ selectivity\ (\%) = \frac{[CH_4]}{[CO] + [CO_2] + [CH_4] + [C_2H_4] + [C_2H_6]} \times 100 \quad (30)$$

$$CO_2\ selectivity\ (\%) = \frac{[CO_2]}{[CO] + [CO_2] + [CH_4] + [C_2H_4] + [C_2H_6]} \times 100 \quad (31)$$

$$C_2H_4\ selectivity\ (\%) = \frac{[C_2H_4]}{[CO] + [CO_2] + [CH_4] + [C_2H_4] + [C_2H_6]} \times 100 \quad (32)$$

$$C_2H_4\ yield\ (\%) = \frac{[C_2H_6]\ conversion \times [C_2H_4]\ selectivity}{[CO] + [CO_2] + [CH_4] + [C_2H_4] + [C_2H_6]} \times 100 \quad (33)$$

3. Results and Discussion

3.1. Catalyst's characterization

Several analytical techniques were used to characterize the synthesized catalysts. SEM/EDS was used to study the catalysts surface morphology and to access their composition. XRD was used to identify the crystalline phases of the prepared materials before and after any previous treatment, e.g., after H_2–TPR studies and after the catalytic studies aiming an understanding of the catalysts' evolution and the identification of the active species. Nitrogen adsorption−desorption Brunauer−Emmett−Teller (BET) method was used to measure the catalysts specific surface areas. H_2–TPR provided an understanding of the catalyst oxygen's lability. Their acid-base properties were evaluated by testing the catalyst behaviour in a model reaction (dehydrogenation/dehydration of 2-propanol). All the obtained results will be addressed in this chapter.

3.1.1. Morphology and composition: SEM/EDS

As an example, **Figure 34** shows SEM images of the Ga:Ce (1:1) fibres obtained by the electrospinning technique before (**34a**) and after (**34b**) the calcination treatment at 800 °C. The loss in diameter after calcination is significant (**Table 7**) and 74% smaller in the case of the Ga:Ce (1:1) fibres. This is associated to the elimination of polymer (PVP) from their structure after the calcination treatment. Images of the remain ratios of fibres, being similar to the ones here presented, can be found in the appendix **A** (**Figure A1**).

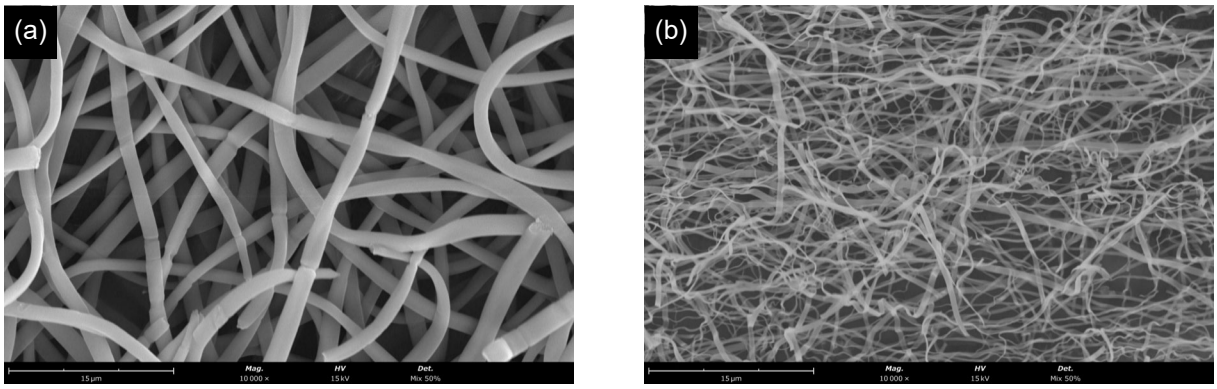

Figure 34: SEM images of Ga:Ce (1:1) fibres (a) before, and (b) after calcination at 800 °C (magnification 10 000x).

Before calcination, it seems that increasing Ga content, diminishes the fibres' diameter, while after calcination such tendency is not so evident. This fact can be related to the different viscosity of the precursor solutions: solutions with more Ce are more viscous: Ga:Ce (3:1) < Ga:Ce (1:1) < Ga:Ce (1:3). Viscosity is an important parameter that strongly influences the fibre quality, uniformity, and size, when it is higher induces the enlargement of the fibre diameter.[109]

These results are in agreement with those already published in the literature, which normally indicate a smaller fibre diameter for β-Ga_2O_3 (around 340 nm)[110] compared to CeO_2 nanofibres (around 350 nm).[124]

Table 7: Average and Standard Deviation of fibres' diameters.

Fibres		Diameter (nm)		Loss (%)
		Before calcination	After calcination	
Ga:Ce	(1:3)	1947 ± 446	900 ± 154	54
	(1:1)	1430 ± 159	375 ± 135	74
	(3:1)	1070 ± 129	393 ± 125	63

For what concerns the aerogels prepared by the epoxide addition method, SEM images obtained show a spongy appearance (**Figure 35**) which is very different from the fibres. Again, images of the remain ratios of aerogels, being similar to the ones here presented, can be found in the appendix **A** (**Figure A2**).

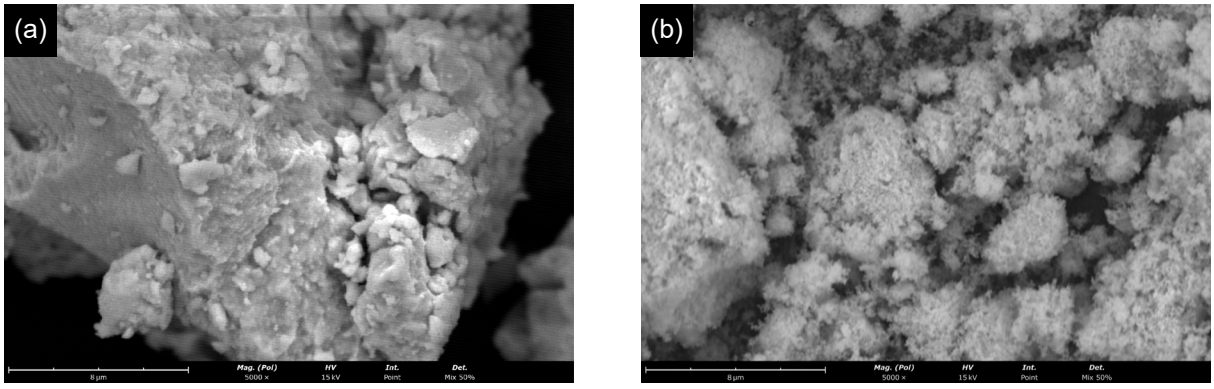

Figure 35: SEM images of (a) Ga:Ce (1:1) bimetallic oxide (b) CeO_2 aerogels (5 000x magnification).

In the case of the copper supported catalysts ($25_{wt.\%}Cu$) obtained by impregnation over pure metal oxides (CeO_2 and Ga_2O_3) and over the Ga:Ce (1:1) bimetallic oxide aerogels, a needle-like structure can be seen that is typically associated with copper oxide, which was confirmed by EDS (**Figure 36**).

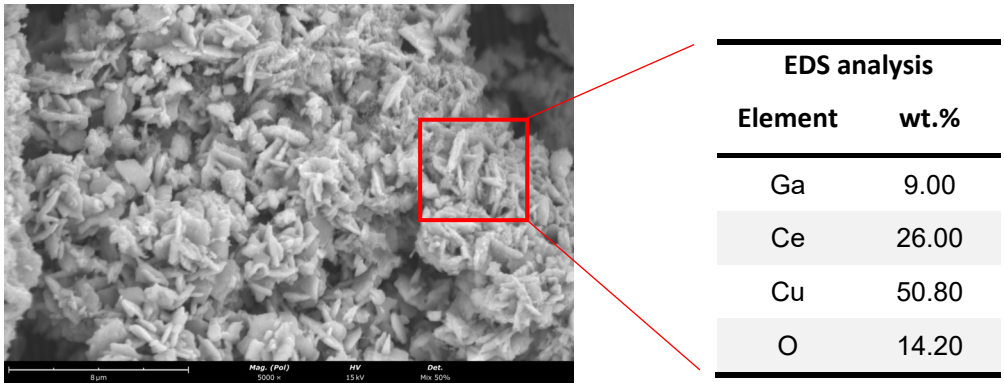

EDS analysis	
Element	**wt.%**
Ga	9.00
Ce	26.00
Cu	50.80
O	14.20

Figure 36: SEM images of $25_{wt.\%}Cu$ impregnated on Ga:Ce (1:1) (5 000x magnification) and local EDS analysis.

Table 8 summarizes all materials compositions obtained by EDS. It is clear that gallium is often in lower quantities while cerium is in higher quantities than predicted, especially in Ga:Ce (3:1) materials. A mistake in the catalyst synthesis or a gallium underestimation by the EDS analysis, as a peak of Ga at 1.098 keV was probably not identified as a Ga peak, may explain the lower wt.%Ga. This can be seen in **Figure 37**, where one EDS spectrum of the Ga:Ce(3:1) aerogel and the X-ray emission lines of gallium[125,126] are presented. Considering that Ga wt.% is systematically lower than that expected, the human error was excluded, and the differences obtained attributed to the EDS analysis itself. In regard to the copper oxide materials, these are overestimated mainly due to the fact cooper oxide being at the surface blocks gallium and cerium signals, which explains also the lower content found for such metals.

Table 8: Catalysts' composition: EDS semi-quantitative analysis.

Catalyst		EDS analysis (wt.%) %Ga Exp.	%Ga Theo.	%Ce Exp.	%Ce Theo.	%O Exp.	%O Theo.	%Cu Exp.	%Cu Theo.	Ratio Ga/Ce Exp.	Ratio Ga/Ce Theo.
Fibres											
Ga:Ce	(1:3)	5.6	11.4	63.9	68.9	30.6	19.7	-	-	0.18	**0.33**
	(1:1)	26.7	26.2	48.3	52.7	24.3	21.1	-	-	1.11	**1.00**
	(3:1)	33.3	46.2	34.8	30.9	32.0	22.9	-	-	1.92	**3.00**
Aerogels											
CeO_2		-	-	74.8	81.4	25.3	18.6	-	-	-	-
Ga:Ce	(1:3)	10.1	11.4	75.5	68.9	14.4	19.7	-	-	0.27	**0.33**
	(1:1)	19.9	26.2	57.6	52.7	22.4	21.1	-	-	0.92	**1.00**
	(3:1)	35.7	46.2	43.2	30.9	21.1	22.9	-	-	2.05	**3.00**
Ga_2O_3		67.1	74.4	-	-	32.9	25.6	-	-	-	-
Impregnated											
$25_{wt.\%}Cu/Ga:Ce$		13.1	18.1	33.2	36.4	19.1	19.7	34.6	24.7	0.78	**1.00**
$25_{wt.\%}Cu/CeO_2$		-	-	56.2	57.1	15.9	19.6	27.9	23.3	-	-
$25_{wt.\%}Cu/Ga_2O_3$		45.8	52.2	-	-	25.0	24.0	29.2	23.8	-	-

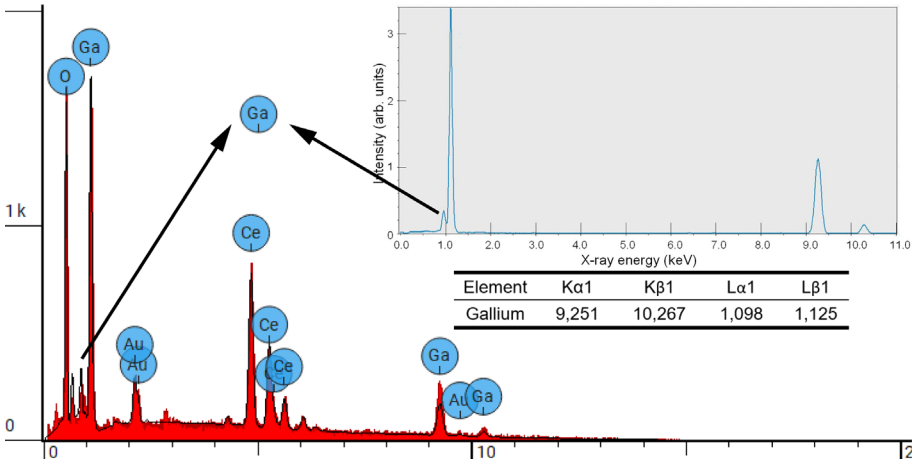

Figure 37: EDS spectrum of Ga:Ce (3:1) bimetallic oxide aerogel (inset show X-ray emission lines of gallium).

3.1.2. Powder X-ray diffraction

Figure 38 presents the XRD patterns of Ga_2O_3, CeO_2, obtained by the epoxide addition method and those of the Ga-Ce bimetallic oxides obtained by electrospinning technique and epoxide addition method. Pure Ga_2O_3 and CeO_2 present diffraction patterns that are consistent with the ones present in the ICSD (Inorganic Crystal Structure Database) – ICSD 83645 and ICSD 88759 for the monoclinic phase of β–Ga_2O_3 and cubic phase of CeO_2, respectively. The diffraction pattern of the Ga-Ce bimetallic oxides (1:3) only show those peaks corresponding to CeO_2. β–Ga_2O_3 peaks are visible in Ga:Ce (3:1) and (1:1), but they are weak, which could be due amorphization or X-ray inaccessibility due to incorporation of Ga^{3+} cations into cerium oxide cubic structure either by simple insertion in its interstices or by Ce^{4+} substitution.

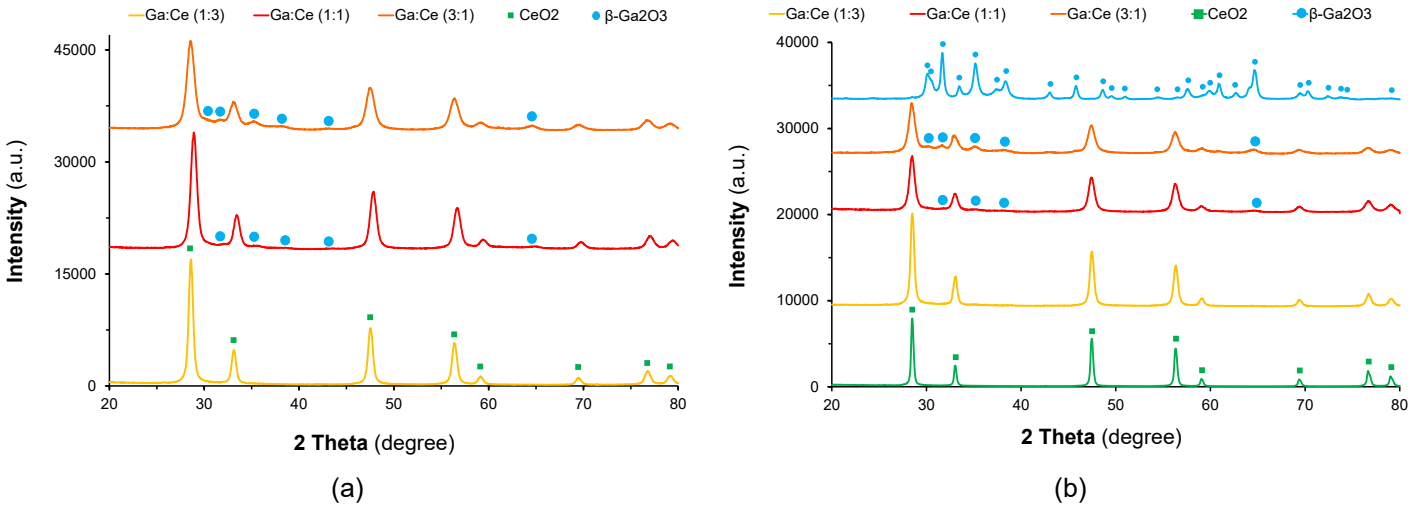

Figure 38: XRD patterns of Ga:Ce bimetallic oxides either as (a) fibres, (b) aerogels and those of pure CeO_2 and Ga_2O_3 aerogels.

Table 9 show the lattice parameter and the crystallite sizes, estimated by the Scherer equation **(21)** using the EVA software, obtained for either the pure oxides or the Ga-Ce bimetallic oxides. These values seem to indicate the formation of a CeO_2–Ga_2O_3 solid solution, which can be a substitutional or interstitial type.[127] In fact, the ionic radius of Ga^{3+} being inferior to that of Ce^{4+} or Ce^{3+} (0.62 versus 0.97 or 1.01 Å, respectively)[128] explains the lattice deviation from the pure CeO_2 materials synthesized by each method.

Table 9: Mean crystallite size and lattice parameter of Ga_2O_3, CeO_2 and Ga-Ce bimetallic oxides.

Catalyst		After calcination			
		Phase	*D* (nm)	Lattice parameter (Å)[a]	Cell Volume (Å^3)
Fibres					
CeO_2		CeO_2	10.50 ± 0.01	5.406 (5.411)	159.302
Ga:Ce	1:3	CeO_2	14.90 ± 0.03	5.403 (5.411)	157.704
		Ga_2O_3	-	-	-
	1:1	CeO_2	10.90 ± 0.02	5.348 (5.411)	152.990
		Ga_2O_3	19.70 ± 0.03	a = 12.16116 (12.214) b = 3.037 (3.037) c = 5.746 (5.798)	103.320
	3:1	CeO_2	8.70 ± 0.04	5.407 (5.411)	158.109
		Ga_2O_3	8.60 ± 0.01	a = 12.173 (12.214) b = 3.053 (3.037) c = 5.777 (5.798)	207.943
Aerogels					
CeO_2		CeO_2	26.50 ± 0.08	5.421 (5.411)	159.302
Ga:Ce	1:3	CeO_2	17.60 ± 0.04	5.419 (5.411)	159.138
		Ga_2O_3	-	-	-
	1:1	CeO_2	12.40 ± 0.09	5.426 (5.411)	159.711
		Ga_2O_3	15.40 ± 0.77	a = 12.216 (12.214) b = 3.046 (3.037) c = 5.799 (5.798)	208.955
	3:1	CeO_2	10.70 ± 0.21	5.429 (5.411)	160.017
		Ga_2O_3	11.10 ± 0.03	a = 12.208 (12.214) b = 3.042 (3.037) c = 5.812 (5.798)	209.4505
Ga_2O_3		Ga_2O_3	23.80 ± 0.08	a = 12.224 (12.214) b = 3.040 (3.037) c = 5.808 (5.798)	209.545

[a] Between parentheses are the ICSD values.

In the case of the fibers (**Figure 39a**), these values are consistent with CeO_2 lattice contraction and confirms the hypothesis of Ga incorporation by substitution of Ce atoms on the CeO_2 matrix that is especially important for the Ga:Ce (1:1). In the case of the aerogels (**Figure 39b**), such contraction also exists for the Ga-Ce bimetallic oxide with 1:3 molar ratio, whereas the increase of gallium content (1:1 and 3:1 molar ratios) increases the lattice parameters that are consistent with an interstitial incorporation of gallium into the CeO_2 matrix. It seems to exist a crystallite size dependence on the lattice parameters of CeO_2, the lattice parameter "*a*" increase with decreasing nanoparticle size, which explains the evolution of the CeO_2 crystallite sizes when the gallium content increases.

It is known from the literature that a complete substitution is only possible if the host ion and the substitutional ion have a similar size.[127] Therefore, due to the large difference in ionic radius between Ce^{4+} and Ga^{3+}, there seems to be a limit for the Ce^{4+} substitution by Ga^{3+}, which in the literature is reported to be near 25 % mol/mol of Ga.[72,129–132] The results from this work suggest that this limit may be higher, closer to 33% in the case of the aerogels and closer to 50% in the case of the fibres.

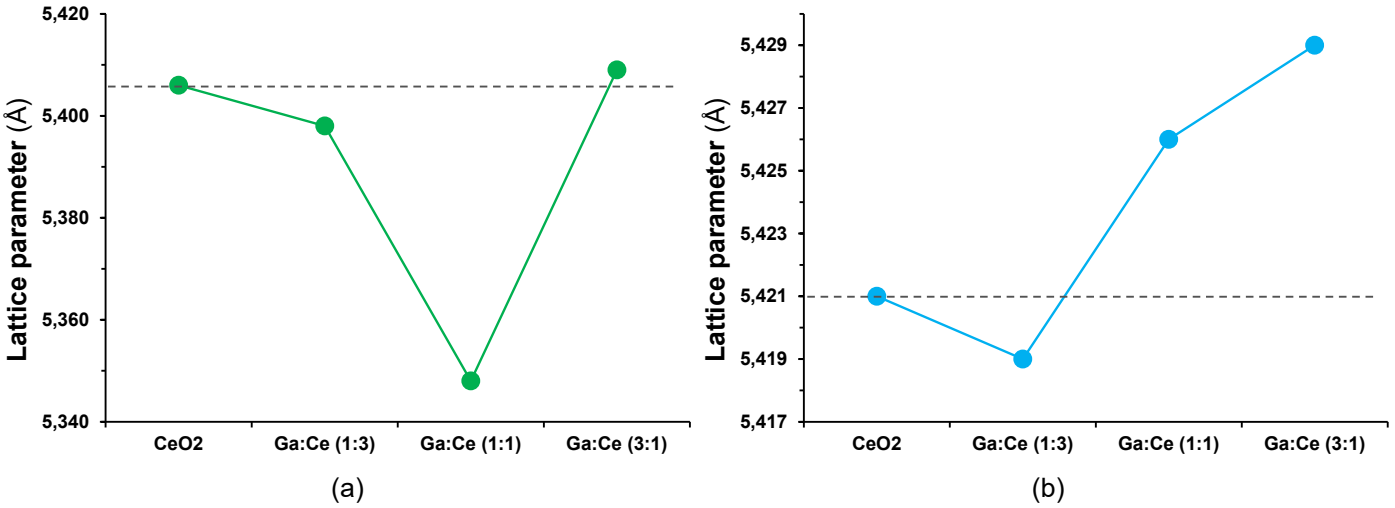

Figure 39: Ga-Ce bimetallic oxides lattice parameter evolution for (a) fibres and (b) aerogels: comparison with pure CeO_2.

After the H_2–TPR measurements, **Figure 40** shows the diffraction patterns obtained. Accordingly, pure CeO_2 and Ga_2O_3 are stable since neither the formation of Ce_2O_3, nor other known phases of gallium oxide were observed after this study. For what concerns the Ga-Ce bimetallic oxides, increasing the gallium content seems to enhance the redox behaviour of CeO_2 as the formation of new phases, such as the hexagonal phase of Ce_2O_3 (hexagonal phase, ICSD 96197) and the tetragonal phase of $CeGaO_3$ (tetragonal phase, ICSD 55629) appear in Ga:Ce (1:1) and Ga:Ce (3:1), respectively, which proves that Ce^{4+} was reduced to Ce^{3+}.

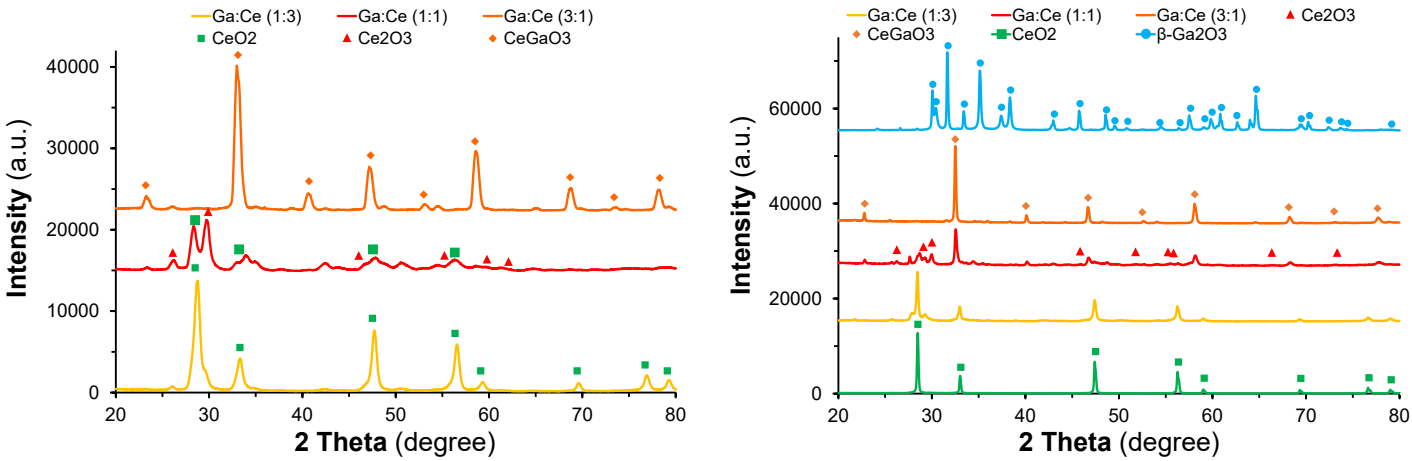

Figure 40: XRD patterns of Ga-Ce bimetallic oxides obtained as (a) fibres, (b) aerogels and those of pure CeO_2 and Ga_2O_3 aerogels after H_2–TPR.

The formation of $CeGaO_3$ has already been reported by other authors due to its properties, such as ferromagnetism.[133] Usually, this material is obtained by arc-melting, under an inert atmosphere[134,135] or under a reducing atmosphere.[136,137] Nevertheless, these studies have reported that pure $CeGaO_3$ is quite difficult to synthesized, without complete CeO_2 reduction. Only at 1300 °C in vacuum,[136] or

1000 °C using a mixture of 6% H_2 in Ar[137], large amounts of such perovskite were identified by X-ray diffraction patterns. In this work, $CeGaO_3$ was easily obtained, and the amount of this perovskite seems to increase with the content of gallium in the samples, with the diffraction pattern of $CeGaO_3$ being the only observed for the highest molar ratio (Ga-Ce; 3:1) which confirm its purity via either of the preparation methods used in this work.

After H_2–TPR, the peaks of CeO_2 and Ga_2O_3 become narrower and the crystallites sizes and the lattice parameters increase, as can be seen in **Table 10**, which can be explained by the high temperature (>1000 °C) attained in such studies.

Table 10: Mean crystallite size and lattice parameter of Ga_2O_3, CeO_2 and Ga-Ce bimetallic oxides after H_2–TPR.

Catalyst		After H_2–TPR			
		Phase	***D* (nm)**	**Lattice parameter (Å)[a]**	**Cell Volume (Å^3)**
Fibres					
Ga:Ce	1:3	CeO_2	11.40 ± 0.03	5.413 (5.411)	158.631
		Ga_2O_3	-	-	-
	1:1	CeO_2	12.1 ± 0.05	5.453 (5.411)	162.151
		Ce_2O_3	13.10 ± 0.04	a = 3.894 (3.941) c = 6.283 (6.182)	82.496
		Ga_2O_3	-	-	-
	3:1	$CeGaO_3$	35.50 ± 0.14	a = 3.890 (3.873) c = 3.882 (3.880)	58.726
Aerogels					
CeO_2		CeO_2	43.70 ± 0.02	5.423 (5.411)	159.483
Ga:Ce	1:3	CeO_2	34.90 ± 0.66	5.429 (5.411)	160.034
		Ga_2O_3	-	-	-
	1:1	CeO_2	17.50 ± 0.05	5.386 (5.411)	156.249
		Ce_2O_3	29.40 ± 0.28	a = 3.972 (3.941) b = 6.178 (6.182)	84.423
		$CeGaO_3$	34.10 ± 0.31	a = 3.885 (3.873) c = 3.877 (3.880)	58.51
	3:1	$CeGaO_3$	43.10 ± 0.10	a = 3.891 (3.873) c = 3.878 (3.880)	58.708
Ga_2O_3		Ga_2O_3	47.30 ± 0.15	a = 12.231 (12.214) b = 3.043 (3.037) c = 5.813 (5.798)	210.112

[a] Between parentheses are the ICSD values.

Regarding the $25_{wt.\%}$Cu supported materials, they show the diffraction patterns of the supports and additionally the diffraction patterns of CuO (monoclinic phase, ICSD 43179), as shown in **Figure 41**.

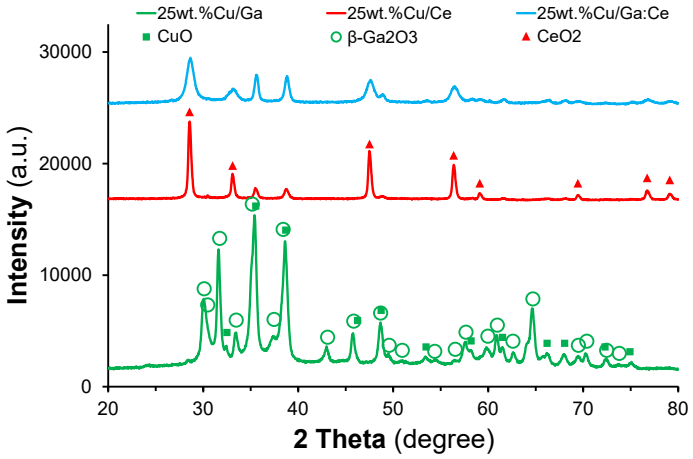

Figure 41: XRD patterns of $25_{wt.\%}Cu/Ga:Ce$, $25_{wt.\%}Cu/CeO_2$, and $25_{wt.\%}Cu/Ga_2O_3$ obtained after calcination.

Table 11 presents the respective mean crystallite sizes and lattice parameters. The values obtained for the lattice parameters are very similar, which agree with the preparation of a copper supported based catalysts with minor intervention of the support. In comparison with their supports, their CeO_2 and Ga_2O_3 crystallites are slightly smaller.

Table 11: Mean crystallite size and lattice parameter of 25wt.%Cu supported on Ga:Ce (1:1), Ga_2O_3, and CeO_2 after calcination.

Catalyst	After calcination			
	Phase	*D* (nm)	Lattice parameter (Å)[a]	Cell Volume (Å^3)
Impregnated				
25wt.%Cu/Ga:Ce	CeO_2	9.40 ± 0.10	5.393 (5.411)	156.884
	CuO	16.20 ± 0.07	a = 4.693 (4.683) b = 3.423 (3.420) c = 5.120 (5.125)	81.085
	Ga_2O_3	-	-	-
Ga:Ce 1:1	CeO_2	12.40 ± 0.09	5.426 (5.411)	159.711
	Ga_2O_3	15.40 ± 0.77	a = 12.216 (12.214) b = 3.046 (3.037) c = 5.799 (5.798)	208.955
25wt.%Cu/CeO_2	CeO_2	22.70 ± 0.06	5.406 (5.411)	157.963
	CuO	17.60 ± 0.30	a = 4.679 (4.683) b = 3.422 (3.420) c = 5.131 (5.125)	81.046
CeO_2	CeO_2	26.5 ± 0.08	5.421 (5.411)	159.302
25wt.%Cu/Ga_2O_3	Ga_2O_3	22.60 ± 0.07	a = 12.241 (12.214) b = 3.024 (3.037) c = 5.820 (5.798)	209.158
	CuO	15.10 ± 0.10	a = 4.688 (4.683) b = 3.428 (3.420) c = 5.131 (5.125)	81.29
Ga_2O_3	Ga_2O_3	23.8 ± 0.08	a = 12.224 (12.214) b = 3.040 (3.037) c = 5.808 (5.798)	209.545

[a] Between parentheses are the ICSD values.

Nevertheless, after the H_2–TPR studies, the diffraction patterns are very different, except for the cerium oxide supported copper catalyst (**Figure 42**). In this case, CeO_2 remains stable but CuO was reduced to metallic Cu (cubic phase, ICSD 53246). As for the $25_{wt.\%}Cu$ supported on Ga_2O_3, Ga_2O_3 did not reduce, but a new intermetallic phase is formed, the cubic phase of Ga_4Cu_9 (cubic phase, ICSD 627389). While in the case of $25_{wt.\%}Cu$ supported on Ga-Ce (1:1), a partial reduction of CeO_2 to $CeGaO_3$ occurs, together with the formation of metallic Cu.

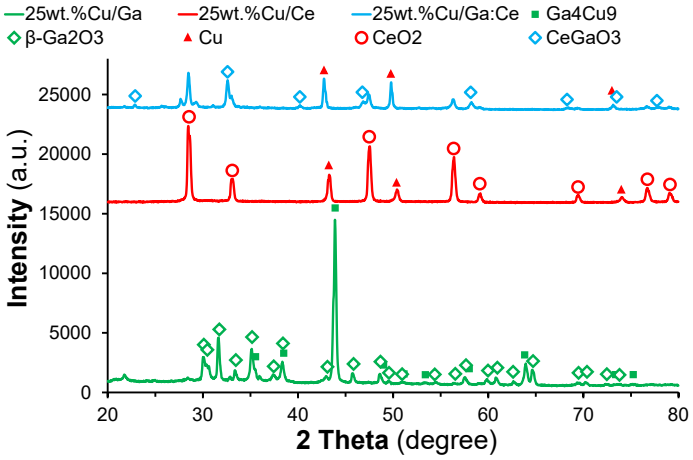

Figure 42: XRD patterns of $25_{wt.\%}Cu/Ga:Ce$, $25_{wt.\%}Cu/CeO_2$, and $25_{wt.\%}Cu/Ga_2O_3$ after H_2–TPR.

Table 12 presents the crystallites sizes and lattice parameters of these materials. As before, the H_2–TPR studies (T>1000 °C) are responsible for increasing the crystallite sizes of CeO_2 and Ga_2O_3 phases.

Table 12: Mean crystallite size and lattice parameter of 25$_{wt.\%}$Cu supported on Ga:Ce (1:1), Ga_2O_3, and CeO_2 aerogels (as well as their respective supports) after H_2–TPR.

Catalyst	Phase	*D* (nm)	After H_2–TPR Lattice parameter (Å)[a]	Cell Volume (Å^3)
Impregnated				
25$_{wt.\%}$Cu/Ga:Ce	CeO_2	27.70 ± 0.98	5.422 (5.411)	159.417
	Cu	28.80 ± 0.29	3.661 (3.621)	49.087
	$CeGaO_3$	24.40 ± 0.28	a = 3.876 (3.873) b = 3.891 (3.880)	58.467
Ga:Ce 1:1	CeO_2	17.50 ± 0.05	5.386 (5.411)	156.249
	Ce_2O_3	29.40 ± 0.28	a = 3.972 (3.941) b = 6.178 (6.182)	84.423
	$CeGaO_3$	34.10 ± 0.31	a = 3.885 (3.873) c = 3.877 (3.880)	58.51
25$_{wt.\%}$Cu/CeO_2	CeO_2	21.00 ± 0.03	5.417 (5.411)	158.925
	Cu	23.10 ± 0.10	3.617 (3.621)	47.331
CeO_2	CeO_2	43.70 ± 0.02	5.423 (5.411)	159.483
25$_{wt.\%}$Cu/Ga_2O_3	Ga_2O_3	31.50 ± 0.15	a = 12.198 (12.214) b = 3.048 (3.037) c = 5.806 (5.798)	209.530
	Ga_4Cu_9	26.60 ± 0.28	8.744 (8.743)	668.441
Ga_2O_3	Ga_2O_3	47.30 ± 0.15	a = 12.231 (12.214) b = 3.043 (3.037) c = 5.813 (5.798)	210.112

[a] Between parentheses are the ICSD values.

All catalysts were also analysed by XRD after the ODHE reaction, the diffraction patterns obtained for the fibres and aerogels are presented in **Figure 43**. Besides a rise of the crystallite sizes and reduction of the cell volumes (**Table 13**), when compared with the measurements obtained before reaction (calcined samples, **Table 9**), any changes of crystalline phases were observed.

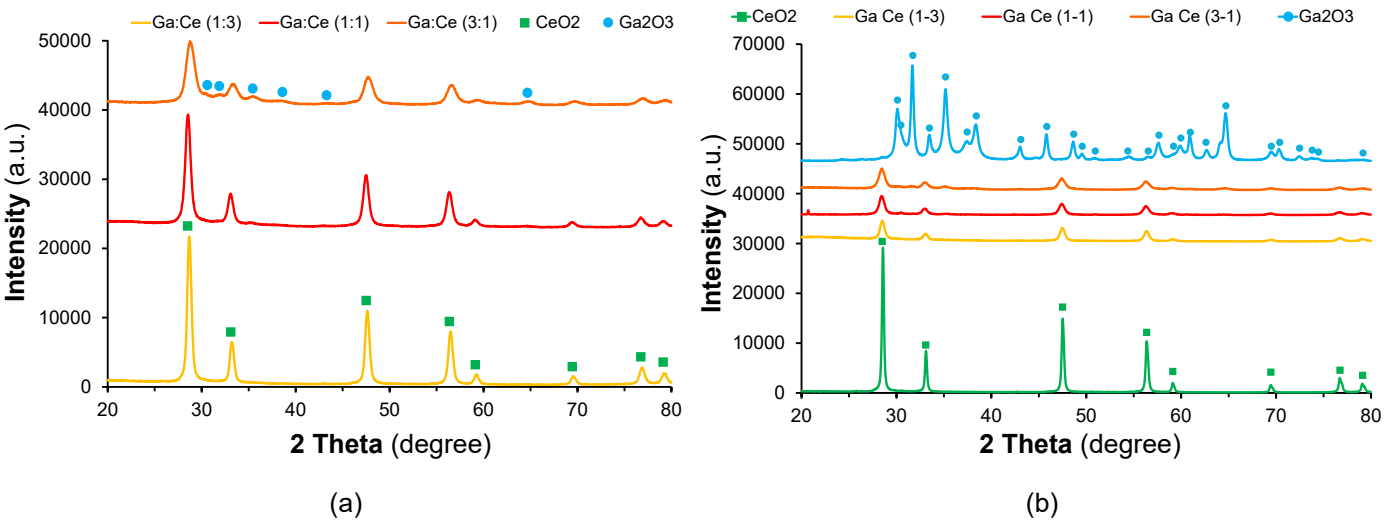

Figure 43: XRD patterns of Ga-Ce bimetallic oxides obtained as (a) fibres, (b) aerogels and those of pure CeO_2 and Ga_2O_3 aerogels after ODHE.

Table 13: Mean crystallite size and lattice parameter of Ga_2O_3, CeO_2 and Ga-Ce bimetallic oxides after ODHE.

Catalyst		After ODHE reaction			
		Phase	*D* (nm)	Lattice parameter (Å)[a]	Cell Volume (Å^3)
Fibres					
Ga:Ce	1:3	CeO_2	15.40 ± 0.02	5.386 (5.411)	156.223
		Ga_2O_3	-	-	-
	1:1	CeO_2	12.30 ± 0.02	5.412 (5.411)	158.533
		Ga_2O_3	-	-	-
	3:1	CeO_2	7.80 ± 0.08	5.365 (5.411)	154.461
		Ga_2O_3	10.10 ± 0.09	a = 12.031 (12.214) b = 3.047 (3.037) c = 5.756 (5.798)	205.746
Aerogels					
CeO_2		CeO_2	33.50 ± 0.06	5.405 (5.411)	157.898
Ga:Ce	1:3	CeO_2	14.80 ± 0.07	5.418 (5.411)	159.043
		Ga_2O_3	-	-	-
	1:1	CeO_2	12.8 ± 0.04	5.429 (5.411)	160.027
		Ga_2O_3	14.00 ± 0.52	a = 12.246 (12.214) b = 3.032 (3.037) c = 5.778 (5.798)	207.895
	3:1	CeO_2	11.20 ± 0.11	5.427 (5.411)	159.836
		Ga_2O_3	19.20 ± 0.07	a = 12.234 (12.214) b = 3.029 (3.0371) c = 5.820 (5.798)	209.348
Ga_2O_3		Ga_2O_3	26.00 ± 0.11	a = 12.212 (12.214) b = 3.043 (3.037) c = 5.800 (5.798)	209.337

[a] Between parentheses are the ICSD values.

On the opposite, important changes could be observed for the 25$_{wt.\%}$Cu supported materials after ODHE reaction (**Figure 44**). If the cooper catalysts supported on CeO_2 and Ga:Ce (1:1) did not show any new crystalline phase, only an increase in the crystallite sizes and an expansion of the cell volume could be confirmed (**Table 14**), in the case of 25wt.%Cu supported on gallium oxide, two new crystalline phases had formed: Cu_2O (cubic phase, ICSD 1626403) due to partial reduction of CuO, a phase recently used by Shibasaki et al.[138] to produce thin film solar cells (they used reactive sputtering to produce this material by cautiously controlling the O_2 flow), and a spinel oxide phase Ga_2CuO_4 (cubic phase, ICSD 1624580). This spinel oxide phase has been studied as an active catalyst for steam reforming of dimethyl-ether (DME), which is a promising hydrogen source[139], as a photocatalyst for solar hydrogen production[140], and as a sensor for inflammable and toxic gases, such as, hydrogen, liquified petroleum gas, and ammonia. Gingasu et al.[141] have also reported two wet chemical routes to produce this material, by a precursor method and by self-propagating combustion. Both phases, could be responsible, or not, for the good catalytic behaviour of such materials (as it is shown later).

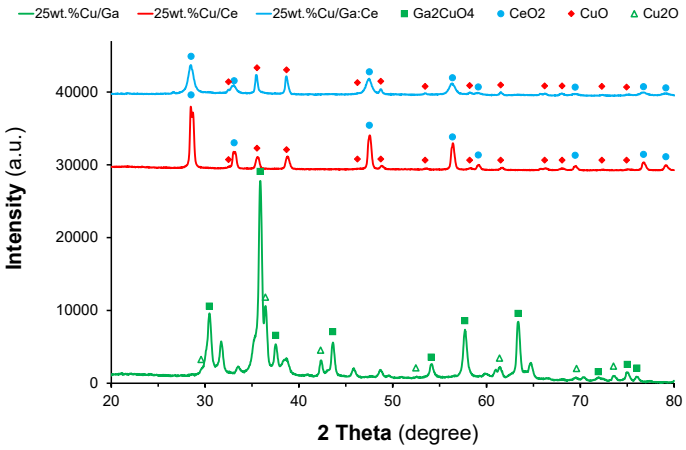

Figure 44: XRD patterns of $25_{wt.\%}Cu/Ga:Ce$, $25_{wt.\%}Cu/CeO_2$, and $25_{wt.\%}Cu/Ga_2O_3$ after ODHE.

Table 14: Mean crystallite size and lattice parameter of $25_{wt.\%}Cu$ supported on Ga:Ce (1:1), Ga_2O_3, and CeO_2 aerogels (as well as their respective supports) after ODHE.

Catalyst	After ODHE reaction			
	Phase	*D* (nm)	Lattice parameter (Å)[a]	Cell Volume (Å^3)
Impregnated				
$25_{wt.\%}Cu/Ga:Ce$	CeO_2	12.40 ± 0.10	5.424 (5.411)	159.552
	CuO	24.80 ± 0.05	a = 4.685 (4.683) b = 3.430 (3.420) c = 5.134 (5.125)	81.399
	Ga_2O_3	-	-	-
Ga:Ce 1:1	CeO_2	12.30 ± 0.02	5.412 (5.411)	158.533
	Ga_2O_3	-	-	-
$25_{wt.\%}Cu/CeO_2$	CeO_2	17.20 ± 0.02	5.408 (5.411)	158.174
	CuO	18.30 ± 0.12	a = 4.675 (4.683) b = 3.429 (3.420) c = 5.115 (5.125)	80.857
CeO_2	CeO_2	33.50 ± 0.06	5.405 (5.411)	157.898
$25_{wt.\%}Cu/Ga_2O_3$	Ga_2O_3	22.80 ± 0.31	a = 12.214 (12.214) b = 3.035 (3.037) c = 5.789 (5.798)	208.254
	Cu_2O	22.90 ± 0.56	4.264 (4.267)	77.509
	Ga_2CuO_4	25.00 ± 0.16	8.292 (8.298)	570.090
Ga_2O_3	Ga_2O_3	26.00 ± 0.11	a = 12.212 (12.214) b = 3.043 (3.037) c = 5.800 (5.798)	209.337

[a] Between parentheses are the ICSD values.

3.1.3. Oxide phases reducibility and stability

The reducibility of the materials synthesized was assessed by H_2–TPR. The profiles obtained allow a better understanding of the redox behaviour of each oxide phase by correlating them with the respective XRD pattern obtained after H_2–TPR analysis. This way, it is possible to correlate hydrogen consumption during H_2–TPR, with the oxide phase reduction.

In the case of pure β–Ga_2O_3, its profile (**Figure 45b**) presents a small peak at 469 °C which others authors have associated to its surface reduction into GaH_x species[142] and formation of oxygen vacancies sites.[143] This, however, is not significant since its XRD patterns obtained after H_2–TPR does not show an oxide phase change. These GaH_x species reoxidize upon cooling to room temperature,[142] which corroborates reports saying that β–Ga_2O_3 is hardly reducible[144] and its H_2–TPR profile does not present any significant H_2 consumption peak.[143,145]

Regarding pure CeO_2, the first peak at 430 °C is also reported to be related to easily reducible surface oxygen of cerium oxide, while the second peak at 784 °C is associated with bulk reduction of CeO_2 to Ce_2O_3.[72,129–131,146] Just like in the case of β–Ga_2O_3, the XRD pattern after H_2–TPR does not show any phase change in the material, thus the reduction being complete at the bulk seems non-existent at a surface easily oxidized as soon as the materials enter in contact with air.

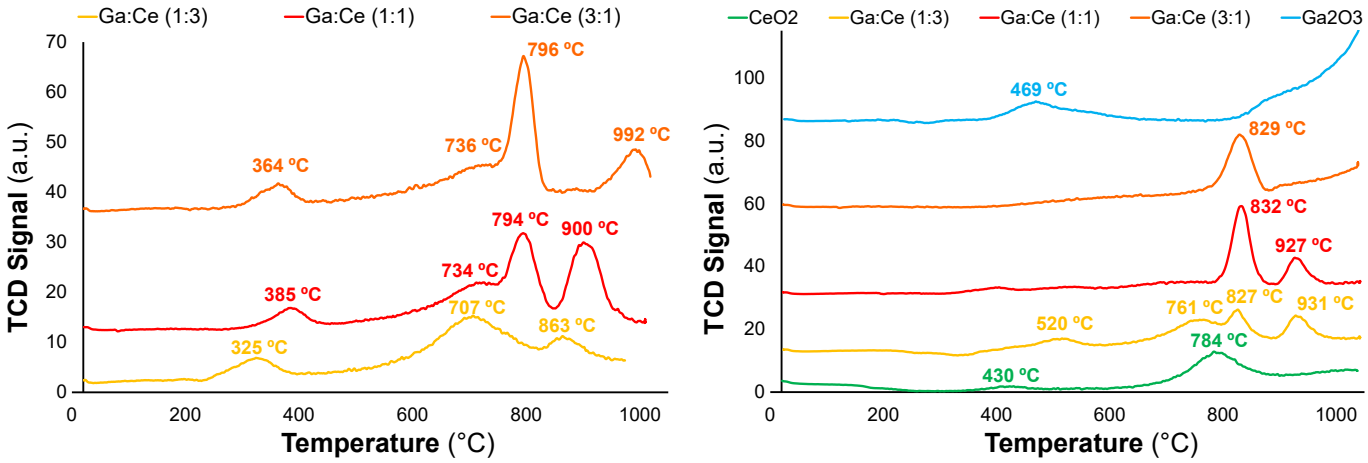

Figure 45: H_2–TPR profiles of Ga-Ce bimetallic oxides obtained as (a) fibres and (b) aerogels; for comparison purposes those of pure CeO_2 and Ga_2O_3 aerogels were also performed and included.

Concerning the Ga-Ce bimetallic oxides, fibres and aerogels similar compositions generated slightly different profiles, as shown in **Figure 45a** and **45b**, probably due to their different morphologies and surface areas.[146] It is noticeable that the addition of more gallium into cerium oxide shifts the peak associated with bulk reduction of CeO_2 to lower temperatures, more visible for the samples with higher CeO_2 content, 734 versus 784 °C or 761 versus 784 °C, for the fibres or aerogels, respectively, that accordingly with the literature could be assigned to a contribution of gallium to improve the reducibility of CeO_2.[72,130–132] It is important to note that it was found a good correlation between the experimental and the theoretical values for the consumption of hydrogen (**Table 15**), which confirms the excepted

global reduction mechanism (**Equations 34a-36**) based on the crystalline phases observed on XRD analyses after H_2-TPR measurements.

Ga:Ce (1:3) fibres: $6\ CeO_2 + Ga_2O_3 \rightarrow 3\ CeO_2 + 1.5\ Ce_2O_3 + Ga_2O_3 + 1.5\ H_2O$ (34a)

Ga:Ce (1:3): $6\ CeO_2 + Ga_2O_3 \rightarrow 4\ CeO_2 + Ce_2O_3 + Ga_2O_3 + H_2O$ (34b)

Ga:Ce (1:1) fibres: $4\ CeO_2 + 2\ Ga_2O_3 \rightarrow CeO_2 + 1.5\ Ce_2O_3 + 2\ Ga_2O_3 + 1.5\ H_2O$ (35a)

Ga:Ce (1:1): $2\ CeO_2 + Ga_2O_3 \rightarrow 2\ CeO_2 + 0.5\ Ce_2O_3 + CeGaO_3 + 1.5\ Ga_2O_3 + 1.5\ H_2O$ (35b)

Ga:Ce (3:1): $2\ CeO_2 + 3\ Ga_2O_3 \rightarrow 2\ CeGaO_3 + 2\ Ga_2O_3 + H_2O$ (36)

Furthermore, Vecchietti et al.[132], have described a relaxation phenomenon, illustrated in **Figure 46**, which may be the explanation behind the rule of Ga in facilitating CeO_2 reduction. Here, after the oxygen atom inside the blue circle is removed, the Ga atom binds to an oxygen site in the CeO_2 matrix, increasing the synergism and facilitating the reduction.

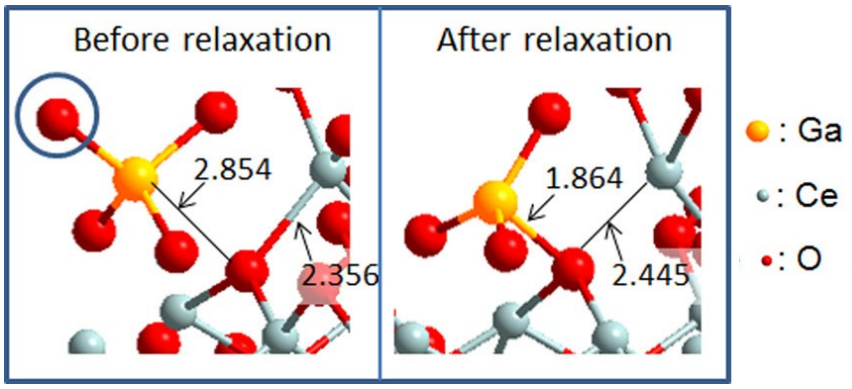

Figure 46: Ga_2O_3 role in CeO_2 reduction. (Adapted from Vecchietti et al.[132])

It is also perceptible that for the fibres and aerogels new peaks appears at higher temperatures, which may be related with the formation of the $CeGaO_3$ phase, as shown by **Equations 35b** and **36**, and the X-ray analysis performed after H_2–TPR. These peaks are shifted to higher temperatures, in the case of aerogels, thus seeming to suggest they are more difficultly reduced and more stable. However, further work is needed in order to confirm such conclusions, namely using pure $CeGaO_3$ perovskites for the H_2–TPR studies, which clearly goes beyond the scope of this work.

Regarding the copper supported catalysts (**Figure 47**), new peaks appears at 184 and 241 °C that can be assigned to the reduction of CuO to metallic copper.[73] In the case of $25_{wt.\%}$Cu supported on CeO_2, those peaks appear at lower temperatures than those of $25_{wt.\%}$Cu supported on Ga_2O_3 or Ga:Ce (1:1). This may be related to the fact that over CeO_2, Cu did not form an intermetallic phase with Ce, favouring, instead, the formation of metallic Cu.

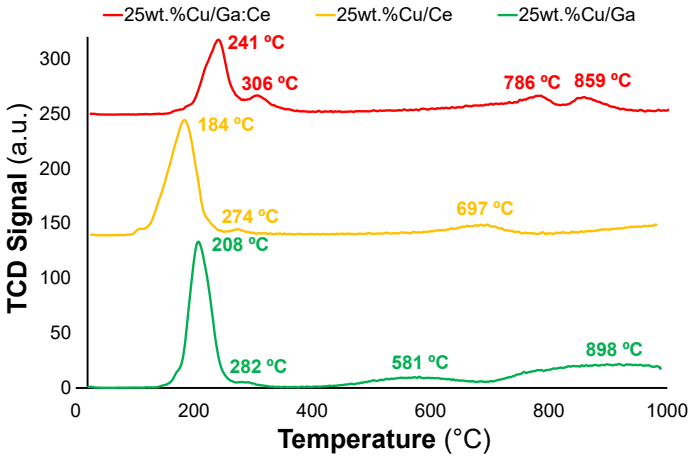

Figure 47: H_2–TPR profiles of copper supported catalysts; $25_{wt.\%}Cu/Ga:Ce$, $25_{wt.\%}Cu/CeO_2$, and $25_{wt.\%}Cu/Ga_2O_3$.

In the case of the other supports that involve Ga, the analysis by XRD shows the formation of a Ga-Cu intermetallic phase (Ga_4Cu_9) in $25_{wt.\%}Cu/Ga_2O_3$ and lattice expansion of metallic Cu phase in $25_{wt.\%}Cu/Ga:Ce$, that could explain the drift to higher temperatures.[73,74] The peaks at higher temperatures (786 and 859 °C) correspond to the same already observed at the Ga:Ce (1:1), meaning the reduction of CeO_2 and the formation of $CeGaO_3$ (Equations **37-39**). Considering the H_2 consumed during the H_2–TPR measurements, the good agreement between experimental and theoretical values confirms the assumptions made (**Table 15**)

$25_{wt.\%}Cu/CeO_2$: $3\ CeO_2 + 2\ CuO \rightarrow 3\ CeO_2 + 2\ Cu + 2\ H_2O$ (37)

$25_{wt.\%}Cu/Ga_2O_3$: $12\ Ga_2O_3 + 9\ CuO \rightarrow 10\ Ga_2O_3 + Ga_4Cu_9 + 15\ H_2O$ (38)

$25_{wt.\%}Cu/Ga:Ce$: $4\ CeO_2 + 2\ Ga_2O_3 + 4\ CuO \rightarrow 2\ CeO_2 + 2\ CeGaO_3 + Ga_2O_3 + 4\ Cu + 5\ H_2O$ (39)

Table 15: H_2 consumptions obtained during the H_2–TPR analysis for the different materials used in this work.

Catalyst		H_2 Consumption (µmoles)[a]	Exp./Theo.
Fibres			
Ga:Ce	1:3	14.8 (15.6)	0.95
	1:1	16.1 (17.8)	0.91
	3:1	10.9 (11.4)	0.96
Aerogels			
CeO_2		-	-
Ga:Ce	1:3	10.3 (10.4)	0.99
	1:1	11.0 (11.8)	0.93
	3:1	11.2 (11.4)	0.98
Ga_2O_3		-	-
Impregnated			
$25_{wt.\%}Cu/Ga:Ce$		33.7 (34.4)	0.98
$25_{wt.\%}Cu/CeO_2$		34.6 (31.4)	1.10
$25_{wt.\%}Cu/Ga_2O_3$		51.3 (52.6)	0.98

[a] Between parentheses are the theoretical values

3.1.4. Acid-base properties

Catalysts' acid-base properties were evaluated using a model reaction, the dehydrogenation/dehydration of 2-propanol. These properties are important aiming an explanation of the catalysts catalytic behaviour for other reactions, namely the one studied in this work, the oxidative dehydrogenation of ethane (ODHE). **Table 16** presents the catalytic results of this model reaction and the respective relative basicity (νA/νP) (**Equation 27**) for each synthesized material. The values here displayed were obtained at 300 °C, with a GHSV of 1012.4 mL/g_{cat}.h under an oxidative atmosphere. Clearly, all materials are strongly basic, selectivity to acetone > 90%, but nuances are perceptible between them that will be explored and correlated later with the catalytic results obtained for ODHE.

Table 16: Dehydrogenation/dehydration of 2-propanol over the fibres, aerogels, and 25$_{wt.\%}$Cu supported materials under oxidative atmosphere.

Catalyst		Conversion 2-propanol (%)	Selectivity (%)		νA/νP
			Acetone	Propene	
Fibres					
Ga:Ce	1:3	44.6	91.9	2.4	38.0
	1:1	50.0	98.6	1.4	71.9
	3:1	29.5	98.8	1.2	83.3
Aerogels					
CeO_2		50.0	93.5	6.5	14.4
Ga:Ce	1:3	18.5	94.8	5.2	18.2
	1:1	12.8	96.7	3.8	25.4
	3:1	3.9	97.4	1.9	51.6
Ga_2O_3		42.7	87.9	12.1	7.3
Impregnated					
25$_{wt.\%}$Cu/Ga:Ce		17.1	97.2	2.8	35
25$_{wt.\%}$Cu/CeO_2[a]		100	100	0.0	100
25$_{wt.\%}$Cu/Ga_2O_3		42.4	97.4	2.6	38.0

[a] The only product observed was the acetone and the value for the basicity (va/vP) is infinit. The option was to use 100 in order to have a rational trend for the basicity.

3.2. Catalytic Studies

In this chapter, the catalytic results are presented and discussed, evaluating the synthesized material's catalytic performance in the oxidative dehydrogenation of ethane (ODHE). For this, it was studied the influence of the oxidant chosen, the temperature, the effect of gallium content in the catalysts prepared, the method of synthesis and respective morphology and the catalyst's basicity. Other preliminary studies conducted in this work are presented and briefly commented in the appendix **B**.

3.2.1. Effect of the oxidizing agent

In order to access the effect of the oxidant in ODHE, Ga:Ce (1:1) aerogel was tested using three different oxidants: molecular oxygen (O_2), nitrous oxide (N_2O) and carbon dioxide (CO_2); across a wide range of temperatures. **Figure 48** shows the results obtained. Clearly, the best results are those obtained using N_2O as oxidizing agent: higher conversion of ethane and higher yields for ethylene across all range of temperatures studied. Using O_2 and CO_2 atmospheres, higher temperatures are required to obtain similar C_2H_6 conversions and C_2H_4 yields. In fact, CO_2 having the highest levels of selectivity towards C_2H_4, it is the oxidant with the lowest conversions and yields, while O_2 having a slightly better activity than CO_2, present lower values in conversions and yields than N_2O. Therefore, it was decided to conduct further tests under N_2O.

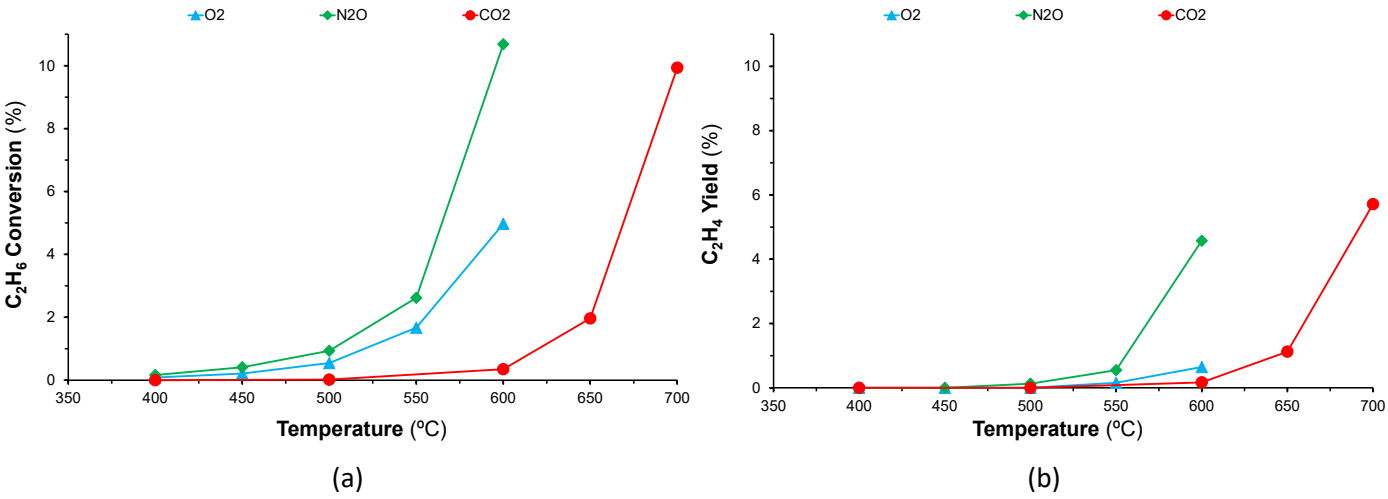

Figure 48: Study of ODHE over Ga:Ce (1:1) aerogel using different oxidizing agent: (a) Ethane conversion and (b) Ethylene yield (Reaction conditions: oxidant/C_2H_6=10, GHSV=7500 mL $C_2H_6/g_{cat}.h$).

3.2.2. Effect of the N_2O/C_2H_6 molar ratio

The study of the N_2O/C_2H_6 molar ratio is an important parameter in order to optimize the reaction performance. Hence, a study of its effect was conducted, as well, and **Figure 49** shows the results obtained over $25_{wt.\%}Cu/Ga_2O_3$ in a range of N_2O/C_2H_6 molar ratios from 2 to 15. It is possible to see that by increasing this value, the C_2H_6 conversion rises until it reaches a maximum conversion at N_2O/C_2H_6=10, which is clearly the best oxidant to reagent molar ratio. Therefore, further studies were done under this condition.

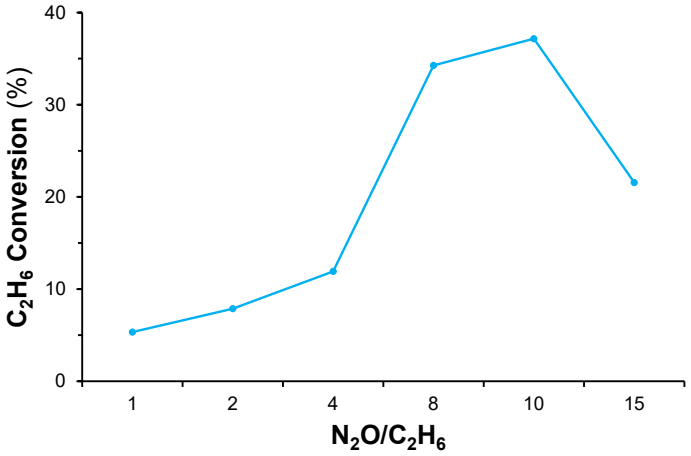

Figure 49: Effect of the oxidant to ethane molar ratio over $25_{wt.\%}Cu/Ga_2O_3$ (Reaction conditions: GHSV=7500 $mL/g_{cat}.h$, T=550 °C).

3.2.3. Effect of temperature

The temperature is a crucial parameter in any reaction that have a great influence on the catalysts' performance. The effect of temperature on the ODHE reaction over the Ga-Ce bimetallic oxides fibres and aerogels are presented in **Figure 50** and **Figure 51**, respectively. As expected, the increase in temperature is followed by the raise of C_2H_6 conversion and C_2H_4 selectivity. It is clear that the best results are those obtained over the fibres, which present higher ethane conversion and ethylene selectivity and yield.

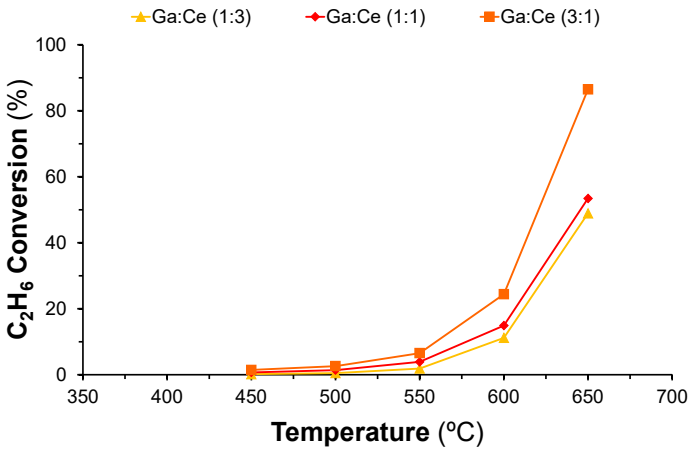

(a)

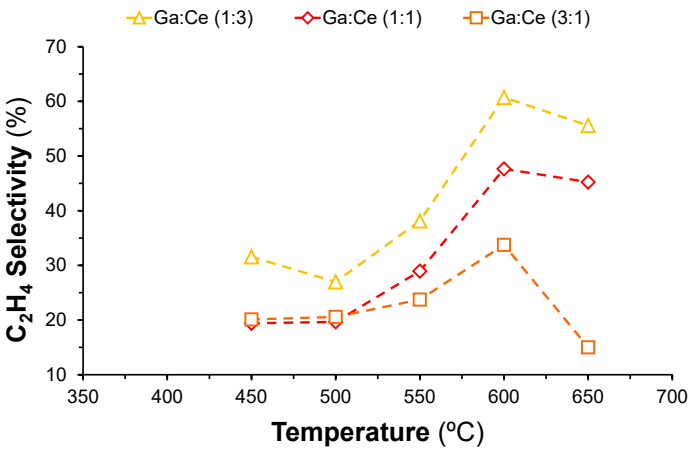

(b)

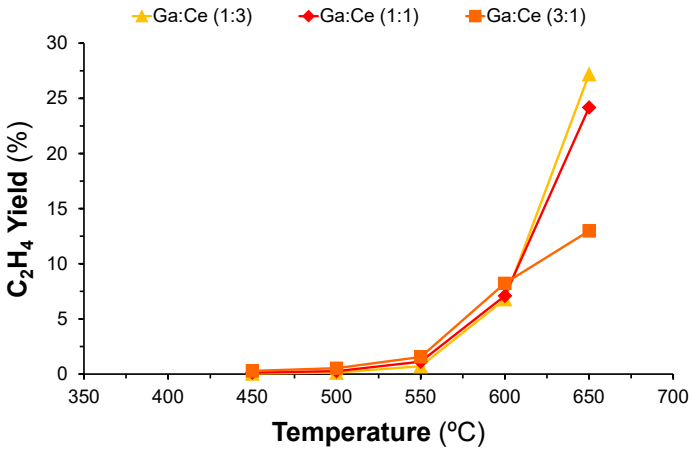

(c)

Figure 50: Effect of temperature on ODHE reaction over fibres, regarding (a) C_2H_6 conversion, (b) C_2H_4 selectivity, and (c) C_2H_4 yield. (Reaction conditions: N_2O/C_2H_6=10, GHSV=7500 mL $C_2H_6/g_{cat}.h$).

For the aerogels (**Figure 51**), the best results are those obtained over pure metal oxides, cerium and gallium, that unfortunately were not possible to prepare as fibres. However, the ethylene selectivity is only around 13 % in the case of cerium oxide, but higher over gallium oxide (around 54 %). Comparing to the Ga-Ce bimetallic oxides, it seems that the addition of gallium to cerium oxide has a positive effect, contributing to increase ethylene selectivity. It is also important to mentioned that blank tests were performed without catalysts (not shown for clarity purposes) and that C_2H_6 conversions and C_2H_4 yields are residual until 550 °C (≤ 0.7%), becoming significative at temperatures above 600 °C (≥ 6%). For this reason, all the results will be compared at 550 °C, the highest temperature that can ashore that the results obtained are not influenced by any spontaneous reaction due to temperature.

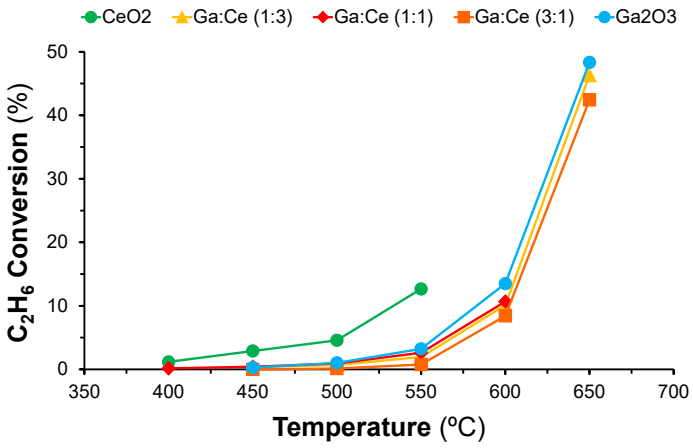

(a)

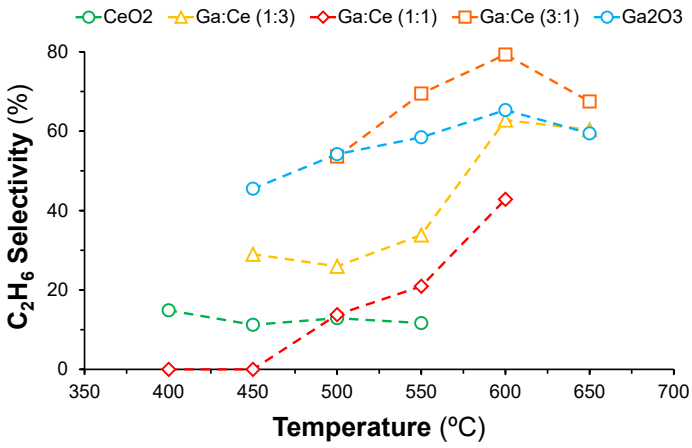

(b)

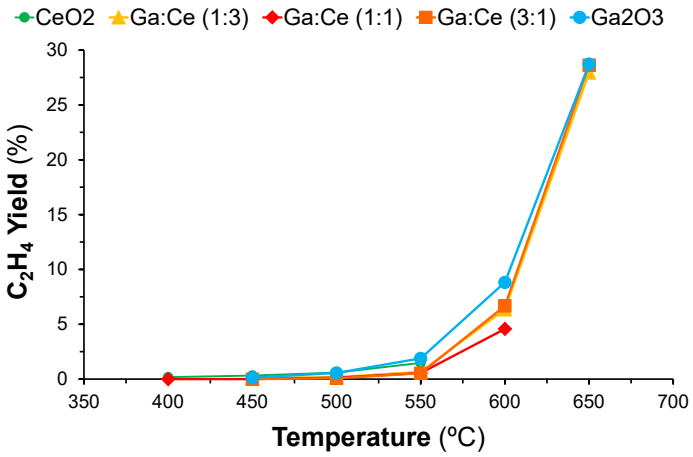

(c)

Figure 51: Effect of temperature on ODHE reaction over aerogels, regarding (a) C_2H_6 conversion, (b) C_2H_4 selectivity, and (c) C_2H_4 yield. (Reaction conditions: N_2O/C_2H_6=10, GHSV=7500 mL $C_2H_6/g_{cat}.h$).

On the other hand, applying the Arrhenius equation, apparent activation energies (E_a) were also calculated for all catalysts (**Figure 52**) and conclusions about the kinetic and thermodynamic regimes achieved, namely: 1) pure metal oxides present the lowest E_a (35 and 62 kJ/mol for CeO_2 and Ga_2O_3, respectively; 2) the values obtained for the fibres are always higher than those obtained for the aerogels (81 versus 68, 61 versus 56 kJ/mol for the catalysts with Ga/Ce molar ratios of 1:3 and 1:1, respectively). The exception seems to be those prepared with a Ga/Ce molar ratio of 3:1 (57 versus 113 kJ/mol). Therefore, kinetically speaking, it was expected higher catalytic activity over the aerogels, which seems not the case and pointing to the existence of other key factors influencing the reaction.

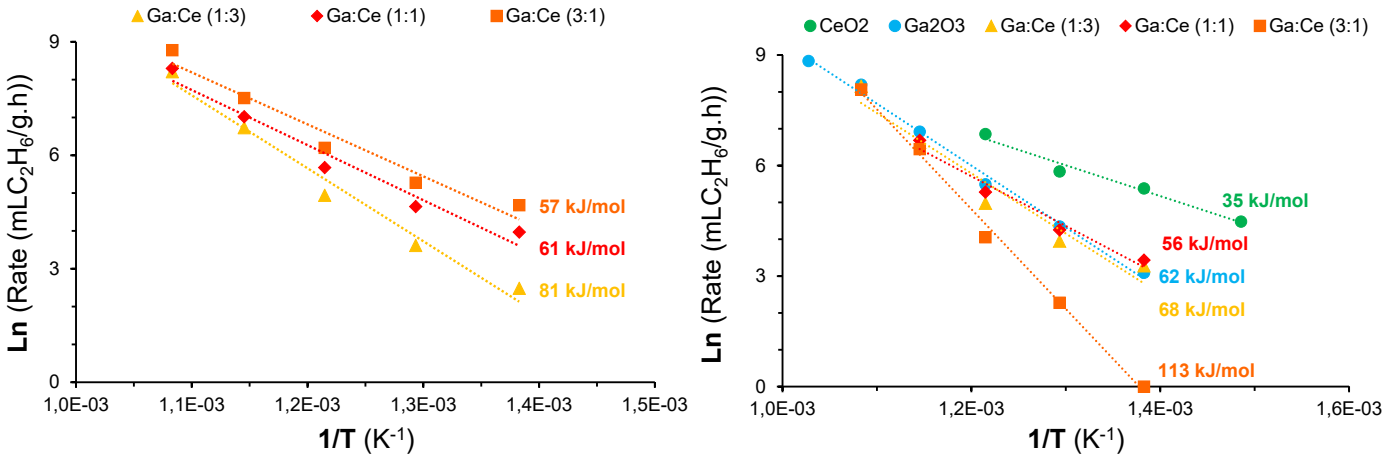

(a) (b)

Figure 52: Arrhenius plots obtained for (a) fibres and (b) aerogels aiming the estimation of ODHE apparent activation energies (shown in figures).

3.2.4. Effect of gallium content and preparation method

In order to evaluate the effect of the addition of gallium on the catalytic behaviour, the results of the pure CeO_2 and Ga_2O_3 aerogels (the later not show for clarity reasons) were compared with those of the bimetallic oxide aerogels at 550 °C (**Figure 53**). The results obtained show that regardless the type of morphology, the addition of gallium to cerium does not have any beneficial effect compared to pure CeO_2, either in terms of C_2H_6 conversion or C_2H_4 yield. On the other hand, it can be also said that the increase of gallium content on the bimetallic oxides seems to be beneficial either for the conversion of ethane or ethylene production, which agrees also with the decrease of E_a reported before.

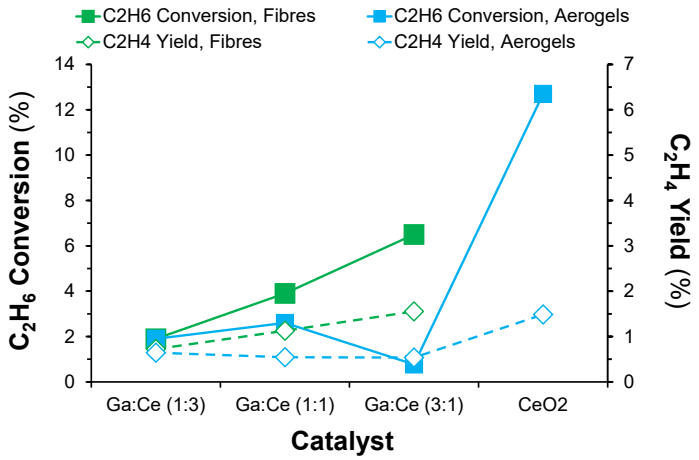

Figure 53: Effect of the gallium addition and synthesis method on the catalytic behaviour for ODHE reaction. (Reaction conditions: N_2O/C_2H_6=10, GHSV=7500 mL C_2H_6/g_{cat}.h, T=550 °C).

3.2.5. Effect of crystallite size and acid-base properties

The crystallite size of the active phases is of great importance in a catalytic reaction, as the materials' performance is largely related to the particles size and morphology.[147] **Figure 54** presents an evolution of the ethylene yield measured at 550 °C with the catalysts crystallite sizes. It was found that the smaller the crystallite size of CeO_2, the better is the catalytic activity for the production of ethylene, either for the fibres or the aerogels. Moreover, as the Ga content rises, the C_2H_4 yield increases, which confirm the conclusions reported before for the temperature effect.

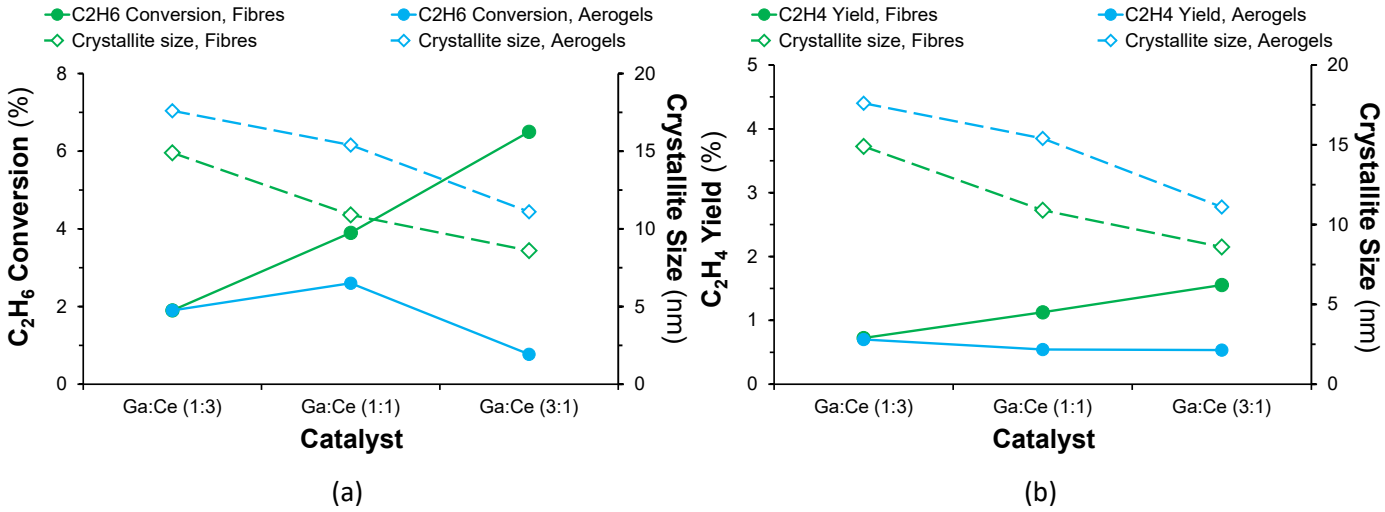

Figure 54: Effect of the CeO_2 crystallite size of fibres and aerogels regarding (a) the C_2H_6 conversion and (b) C_2H_4 yield (Reaction conditions: N_2O/C_2H_6=10, GHSV=7500 mL C_2H_6/g_{cat}.h, T=550 °C).

Since any catalytic behaviour is related to materials electronics, other important way to understand the catalysts activity evolution is to study their acid-base properties. Usually a correlation between such properties and the catalysts catalytic behaviour may occur but need to be confirmed.[148] **Figure 55** shows the trends obtained for the aerogels and fibres basicity and their activity for the production of ethylene. As discussed before, using isopropanol as a molecular probe, the formation of acetone is linked to the presence of basic sites at the catalysts surface and the higher the acetone yield, the higher the basicity.

Gärtner et al.[80] related a higher concentration of basic sites to a higher ethane dehydrogenation, whereas acid sites favour ethane oxidation. The results obtained in this work are in line with these statements (**Figure 55**). It is possible to observe a trend common to both the aerogels and fibres showing the higher the basicity, the higher the yield towards C_2H_4. It is also important to stress that although the basicity of CeO_2 is higher and ethylene yield lower than those measured over Ga_2O_3 (14 and 1.5% versus 7 and 1.9%, respectively), the higher the gallium content, the higher the basicity and activity, which seems to confirm the existence of a synergetic interaction between gallium and cerium already pointed by the XRD analysis that appear to indicate the formation of a CeO_2–Ga_2O_3 solid solution, mainly of the substitutional type.

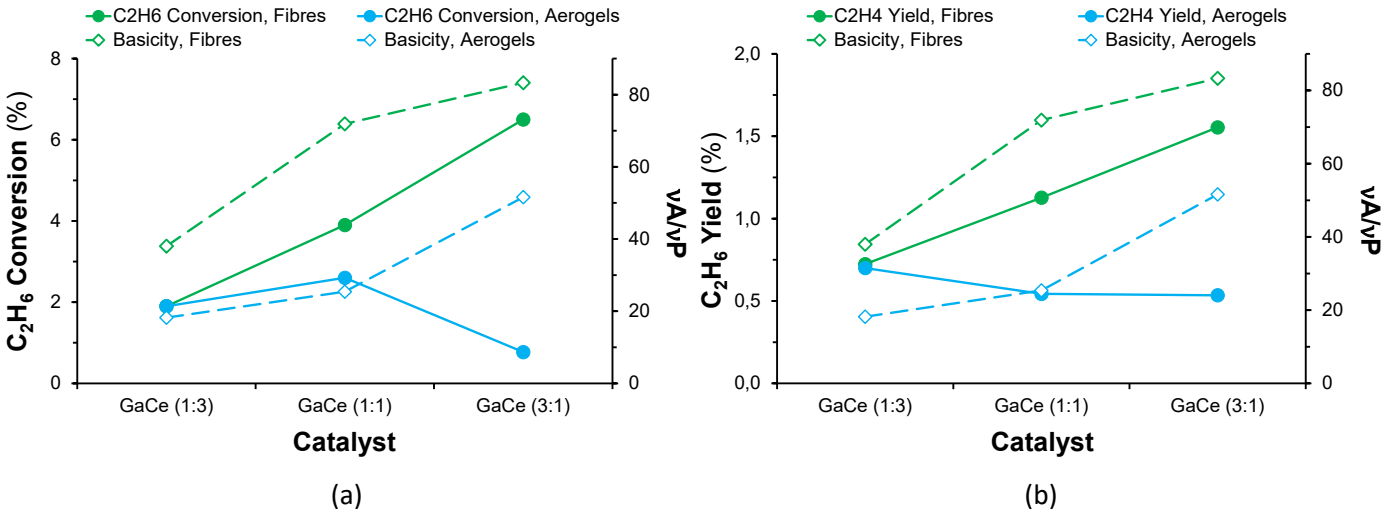

Figure 55: Effect of acid-base properties regarding (a) C_2H_6 conversion and (b) C_2H_4 yield (N_2O/C_2H_6=10, GHSV=7500 mL $C_2H_6/g_{cat}.h$, T=550 °C).

3.2.6. Use as supports for copper-based catalysts

The Pt, Pd containing systems are common catalysts for the selective dehydrogenation of hydrocarbons.[149] However, due to high cost of those catalysts, Ni-Ga alloys, which exhibited comparable catalytic performance of ODHE to noble metal catalysts, emerge as good candidates to replace expensive noble metals-based catalysts.[150] The other successful substitution of noble metal catalysts are chromium-containing materials.[149]

Copper based catalysts have been extensively studied in many reactions, with particular success for the production of methanol,[151] among others. Therefore, considering the results obtained, copper-based materials were prepared by the incipient wetness impregnation method using CeO_2, Ga_2O_3 and the Ga-Ce bimetallic oxide with a molar ratio of 1:1, prepared by the epoxide addition method, as supports and tested as catalysts. The results obtained are presented in **Figure 56**.

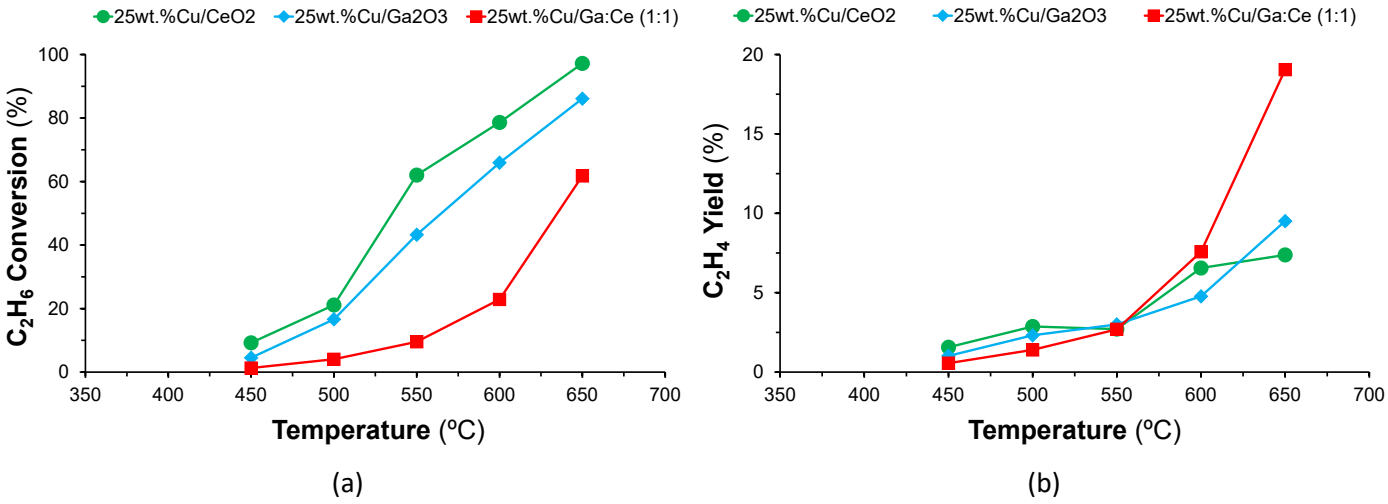

Figure 56: Effect of temperature on ODHE reaction over the 25$_{wt.\%}$Cu supported materials, regarding (a) C_2H_6 conversion, and (b) C_2H_4 yield. (Reaction Conditions: N_2O/C_2H_6=10, GHSV=7500 mL C_2H_6/g_{cat}.h)

It can be said that the best results were those obtained with pure metal oxides as supports and among them the copper supported catalyst on gallium oxide presents the highest activity towards ethylene, which was reinforced by the analysis of the results obtained at 550 °C (**Figure 57**).

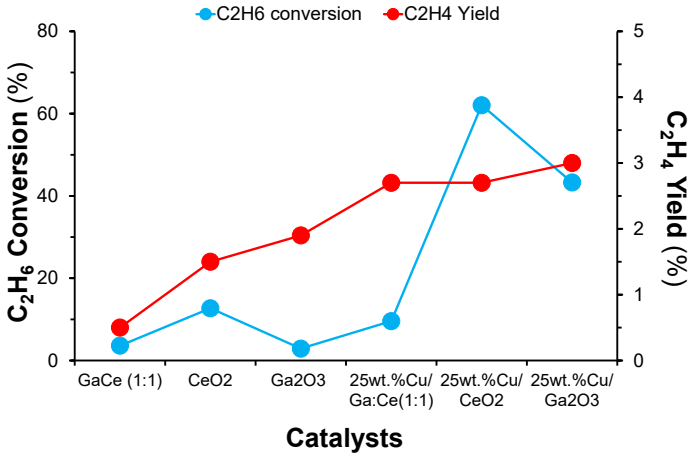

Figure 57: 25$_{wt.\%}$Cu supported materials and their respective supports, in respect of their C_2H_6 conversion and C_2H_4 yield (N_2O/C_2H_6=10, GHSV=7500 mL C_2H_6/g_{cat}.h, T=550 °C).

These results highlight the effect of copper and the enhancement of the reaction using CeO_2 and Ga_2O_3 as support: the conversion increases two-fold between the copper supported on CeO_2 and Ga_2O_3, and their respective supports. It is also worth noting that 25$_{wt.\%}$Cu supported on CeO_2 and Ga_2O_3 shows conversions considerably higher (≈60 and ≈40 %, respectively) than the material supported on Ga:Ce (1:1) (≈10 %), which stress again the advantage of using pure metal oxide supports.

Once again, applying the Arrhenius equation, apparent activation energies (E_a) were calculated for the copper supported materials (**Figure 58**). The values obtained are lower than those of the supports (see **Figure 52b**), which correlates very well with the higher catalytic activity of the copper supported catalyst. (53 versus 56, 34 versus 35, and 41 versus 62 kJ/mol for 25wt.%Cu supported on Ga:Ce (1:1), CeO_2 and Ga_2O_3, respectively).

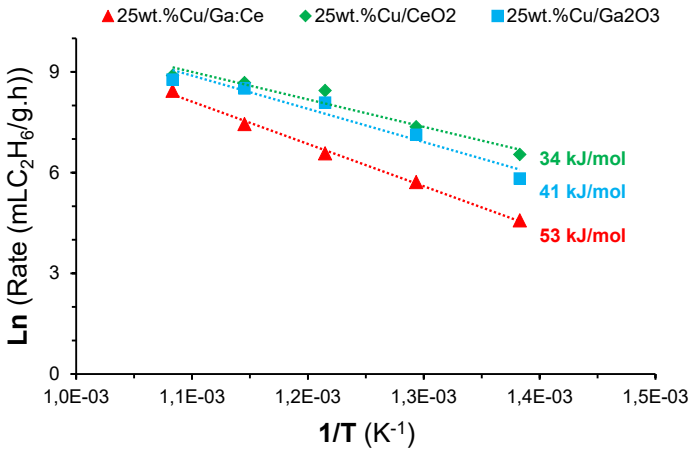

Figure 58: Arrhenius law application to study the apparent activation energies of $25_{wt.\%}$Cu supported materials.

It was also found that the catalysts' crystallite sizes and the acid-base properties have a significative influence on their catalytic behaviour (**Figure 59** and **Figure 60**, respectively). Once again, although slight, the increase in C_2H_4 yield is followed by a downward trend of the CuO crystallite size of the $25_{wt.\%}$Cu supported materials (**Figure 59**). Comparing with the crystallite size of the supports, $25_{wt.\%}$Cu supported on CeO_2 and Ga_2O_3 crystallite sizes are smaller, thus favouring a higher performance confirmed by these results.

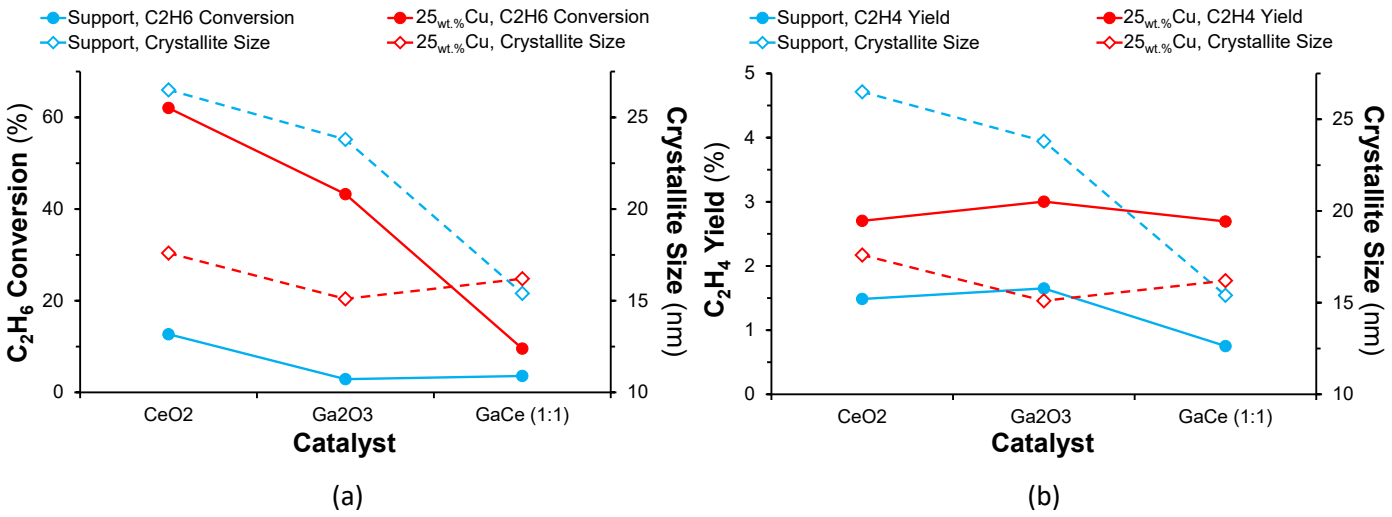

Figure 59: Effect of the active phase's crystallite size of $25_{wt.\%}$Cu supported materials regarding (a) the C_2H_6 conversion and (b) C_2H_4 yield (Reaction conditions: N_2O/C_2H_6=10, GHSV=7500 mL C_2H_6/g_{cat}.h, T=550 °C).

Regarding the basicity effect (**Figure 60**), the same trend could be found, that is: the higher the basicity of the copper supported materials, the higher the conversion of ethane. As for the basicity effect on the yield to ethylene, is difficult to find a specific trend since the decrease yields for ethylene are not followed by an unquestionable decrease in basicity.

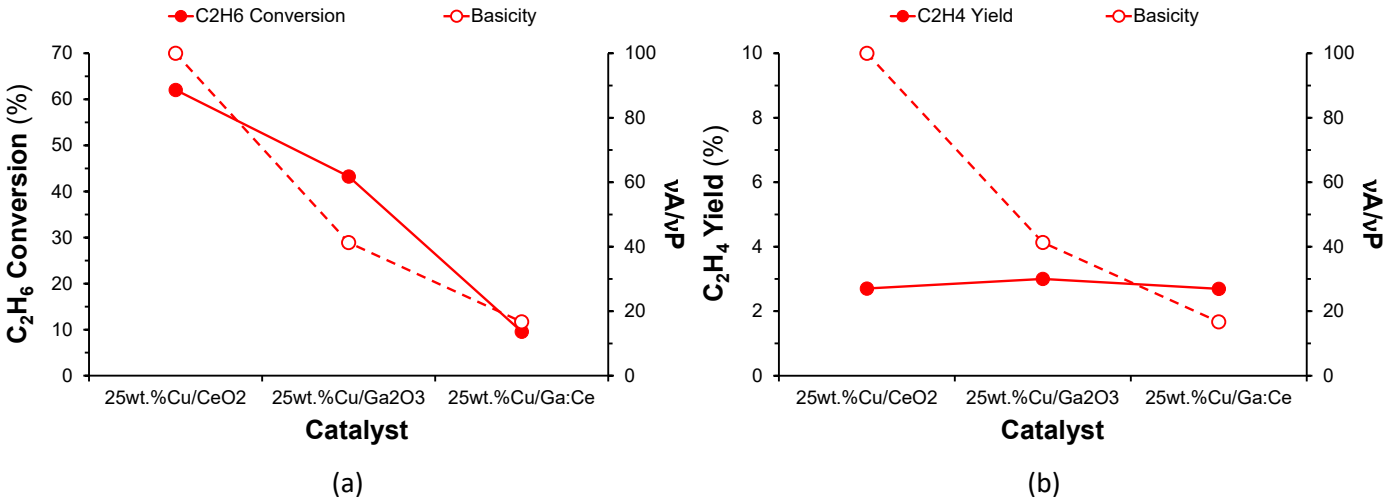

Figure 60: Effect of acid-base properties in 25wt.%Cu supported materials, regarding (a) C_2H_6 conversion and (b) C_2H_4 yield. (N_2O/C_2H_6=10, GHSV=7500 mL C_2H_6/g_{cat}.h, T=550 °C).

4. Conclusions and future perspectives

The work developed in this thesis comprised the preparation of gallium-cerium bimetallic oxides with three molar ratios (Ga:Ce=1:3, 1:1 and 3:1) by two methods: electrospinning technique and epoxide addition method (sol-gel method), aiming at the synthesis of compounds with different morphologies (fibres or aerogels). Besides, Ga_2O_3, CeO_2 and Ga:Ce (1:1) bimetallic oxide obtained as aerogels were also used as supports for copper oxide aiming the investigation of its impact in catalytic behaviour. All materials were characterized by SEM-EDS, Powder-XRD, nitrogen adsorption−desorption Brunauer−Emmett−Teller (BET) method, H_2-TPR studies and their acid-base properties were measured using a model reaction (dehydrogenation/dehydration of 2-propanol).

The two different morphologies were successfully obtained: the aerogels prepared by the epoxide addition method that present a spongy appearance, which is very different from the fibres obtained by electrospinning technique. These materials are better described as oxide solid solutions of gallium-cerium that arise from Ga^{3+} incorporation on the CeO_2 matrix, by substitution of Ce^{4+}, which increases the synergetic interaction between the two metals and contribute to its better catalytic behaviour compared to pure metal gallium and cerium oxides. Moreover, H_2-TPR studies allowed to understand how the pure oxide (Ga_2O_3 and CeO_2) were unable to reduce, while the bimetallic oxides proved that gallium insertion into CeO_2 matrix facilitated its reduction and, inclusive, the formation of a perovskite phase ($CeGaO_3$). Some reports had already studied the formation of this perovskite, however in this work, an easier path to obtain this material with a good purity is presented.

The catalytic studies of dehydrogenation of ethane, aiming to the production of value-added chemicals such as ethylene, with possible practical applications in the petrochemical industry, demonstrated that catalytic behaviour of Ga-Ce bimetallic oxides for ODHE depends on the type of oxidant used, catalyst morphology, aerogels or fibres, crystallite size and catalysts acid-base properties, namely their basicity. From the oxidizing agents tested, N_2O presented the best results. Among the bimetallic Ga-Ce oxides, the best results were those obtained over the fibres with the highest gallium content (Ga-Ce molar ratio 3:1), with 87% of ethane conversion and 13% of ethylene yield at 650 ºC. Furthermore, with the introduction of copper, the catalysts activity increases significantly, especially over copper supported on CeO_2, with 97% ethane conversion and 7% ethylene yield at 650 ºC, showing that copper has an enhanced effect on the catalyst's behaviour. It was also found that the catalytic activity depends on the crystallites size and catalysts acid-base properties and as expected, the smaller the crystallite sizes and the higher the basicity, the higher the catalytic activity towards ethylene. To our knowledge, this is the first time that such type of results using gallium-based catalysts are reported in the literature.

As future work, the copper-based materials could be subjected to a reduction treatment before the catalytic studies, the effect of metallic copper on this reaction studied and they can be also optimized, namely in terms of wt.% of copper used. The stability of all catalysts should be assessed, to better understand their catalytic activity over time. Additionally, and in complement to aerogels, fibres could be also used as supports for copper or other metals that have proven to be more active in ODHE, such as, V, Mo, Ni, or Co.[80,83]

References

(1) de Boisbaudran, L. On the Chemical and Spectroscopic Characters of a New Metal (Gallium). *The London, Edinburgh, and Dublin Philosophical Magazine and Journal of Science* **1875**, *50* (332), 414–416. https://doi.org/10.1080/14786447508641312.

(2) Kumar, S.; Singh, R. Nanofunctional Gallium Oxide (Ga_2O_3) Nanowires/Nanostructures and Their Applications in Nanodevices: Nanofunctional Gallium Oxide (Ga_2O_3) Nanowires/Nanostructures and Their Applications in Nanodevices. *Phys. Status Solidi RRL* **2013**, *7* (10), 781–792. https://doi.org/10.1002/pssr.201307253.

(3) Chi, Z.; Asher, J. J.; Jennings, M. R.; Chikoidze, E.; Pérez-Tomás, A. Ga2O3 and Related Ultra-Wide Bandgap Power Semiconductor Oxides: New Energy Electronics Solutions for CO2 Emission Mitigation. *Materials* **2022**, *15* (3), 1164. https://doi.org/10.3390/ma15031164.

(4) Stepanov, S. I.; Nikolaev, V.; Bougrov, V. E.; Romanov, A. Gallium Oxide: Properties and Applications - A Review. **2016**, *44*, 63–86.

(5) *Web of Science: Analyze Results*. https://www.webofscience.com/wos/woscc/analyze-results/599005b7-99c0-4aa3-8678-81ebba763a34-46f6dccc (accessed 2022-08-03).

(6) Pearton, S. J.; Yang, J.; Cary, P. H.; Ren, F.; Kim, J.; Tadjer, M. J.; Mastro, M. A. A Review of Ga_2O_3 Materials, Processing, and Devices. *Applied Physics Reviews* **2018**, *5* (1), 011301. https://doi.org/10.1063/1.5006941.

(7) Roy, R.; Hill, V. G.; Osborn, E. F. Polymorphism of Ga_2O_3 and the System Ga_2O_3—H_2O. *J. Am. Chem. Soc.* **1952**, *74* (3), 719–722. https://doi.org/10.1021/ja01123a039.

(8) von Wenckstern, H. Group-III Sesquioxides: Growth, Physical Properties and Devices. *Adv. Electron. Mater.* **2017**, *3* (9), 1600350. https://doi.org/10.1002/aelm.201600350.

(9) Zheng, B.; Hua, W.; Yue, Y.; Gao, Z. Dehydrogenation of Propane to Propene over Different Polymorphs of Gallium Oxide. *Journal of Catalysis* **2005**, *232* (1), 143–151. https://doi.org/10.1016/j.jcat.2005.03.001.

(10) Hou, Y.; Wu, L.; Wang, X.; Ding, Z.; Li, Z.; Fu, X. Photocatalytic Performance of α-, β-, and γ-Ga_2O_3 for the Destruction of Volatile Aromatic Pollutants in Air. *Journal of Catalysis* **2007**, *250* (1), 12–18. https://doi.org/10.1016/j.jcat.2007.05.012.

(11) Jamwal, N. S.; Kiani, A. Gallium Oxide Nanostructures: A Review of Synthesis, Properties and Applications. *Nanomaterials* **2022**, *12* (12), 2061. https://doi.org/10.3390/nano12122061.

(12) Mohamed, H. F.; Xia, C.; Sai, Q.; Cui, H.; Pan, M.; Qi, H. Growth and Fundamentals of Bulk β-Ga_2O_3 Single Crystals. *J. Semicond.* **2019**, *40* (1), 011801. https://doi.org/10.1088/1674-4926/40/1/011801.

(13) Ueda, N.; Hosono, H.; Waseda, R.; Kawazoe, H. Synthesis and Control of Conductivity of Ultraviolet Transmitting β-Ga2O3 Single Crystals. *Appl. Phys. Lett.* **1997**, *70* (26), 3561–3563. https://doi.org/10.1063/1.119233.

(14) Varley, J. B.; Weber, J. R.; Janotti, A.; Van de Walle, C. G. Oxygen Vacancies and Donor Impurities in β-Ga2O3. *Appl. Phys. Lett.* **2010**, *97* (14), 142106. https://doi.org/10.1063/1.3499306.

(15) Hudgins, J. L.; Simin, G. S.; Santi, E.; Khan, M. A. An Assessment of Wide Bandgap Semiconductors for Power Devices. *IEEE Trans. Power Electron.* **2003**, *18* (3), 907–914. https://doi.org/10.1109/TPEL.2003.810840.

(16) Higashiwaki, M.; Sasaki, K.; Murakami, H.; Kumagai, Y.; Koukitu, A.; Kuramata, A.; Masui, T.; Yamakoshi, S. Recent Progress in Ga_2O_3 Power Devices. *Semicond. Sci. Technol.* **2016**, *31* (3), 034001. https://doi.org/10.1088/0268-1242/31/3/034001.

(17) Chase, A. O. Growth of β-Ga_2O_3 by the Verneuil Technique. *J American Ceramic Society* **1964**, *47* (9), 470–470. https://doi.org/10.1111/j.1151-2916.1964.tb14442.x.

(18) Lorenz, M. R.; Woods, J. F.; Gambino, R. J. Some Electrical Properties of the Semiconductor β-Ga2O3. *Journal of Physics and Chemistry of Solids* **1967**, *28* (3), 403–404. https://doi.org/10.1016/0022-3697(67)90305-8.

(19) Nikolaev, V. I.; Stepanov, S. I.; Romanov, A. E.; Bougrov, V. E. Gallium Oxide. In *Single Crystals of Electronic Materials*; Elsevier, 2019; pp 487–521. https://doi.org/10.1016/B978-0-08-102096-8.00014-8.

(20) Víllora, E. G.; Shimamura, K.; Yoshikawa, Y.; Aoki, K.; Ichinose, N. Large-Size β-Ga2O3 Single Crystals and Wafers. *Journal of Crystal Growth* **2004**, *270* (3–4), 420–426. https://doi.org/10.1016/j.jcrysgro.2004.06.027.

(21) Tomm, Y.; Reiche, P.; Klimm, D.; Fukuda, T. Czochralski Grown Ga2O3 Crystals. *Journal of Crystal Growth* **2000**, *220* (4), 510–514. https://doi.org/10.1016/S0022-0248(00)00851-4.

(22) Galazka, Z.; Uecker, R.; Irmscher, K.; Albrecht, M.; Klimm, D.; Pietsch, M.; Brützam, M.; Bertram, R.; Ganschow, S.; Fornari, R. Czochralski Growth and Characterization of β-Ga2O3 Single Crystals. *Crystal Research and Technology* **2010**, *45* (12), 1229–1236. https://doi.org/10.1002/crat.201000341.
(23) Kuramata, A.; Koshi, K.; Watanabe, S.; Yamaoka, Y.; Masui, T.; Yamakoshi, S. High-Quality β-Ga_2O_3 Single Crystals Grown by Edge-Defined Film-Fed Growth. *Jpn. J. Appl. Phys.* **2016**, *55* (12), 1202A2. https://doi.org/10.7567/JJAP.55.1202A2.
(24) Aida, H.; Nishiguchi, K.; Takeda, H.; Aota, N.; Sunakawa, K.; Yaguchi, Y. Growth of β-Ga_2O_3 Single Crystals by the Edge-Defined, Film Fed Growth Method. *Jpn. J. Appl. Phys.* **2008**, *47* (11), 8506–8509. https://doi.org/10.1143/JJAP.47.8506.
(25) Hoshikawa, K.; Ohba, E.; Kobayashi, T.; Yanagisawa, J.; Miyagawa, C.; Nakamura, Y. Growth of β-Ga_2O_3 Single Crystals Using Vertical Bridgman Method in Ambient Air. *Journal of Crystal Growth* **2016**, *447*, 36–41. https://doi.org/10.1016/j.jcrysgro.2016.04.022.
(26) Higashiwaki, M. B-Gallium Oxide Devices: Progress and Outlook. *Phys. Status Solidi RRL* **2021**, *15* (11), 2100357. https://doi.org/10.1002/pssr.202100357.
(27) Carter, C. B.; Norton, M. G. Growing Single Crystals. In *Ceramic Materials*; Springer New York: New York, NY, 2013; pp 523–542. https://doi.org/10.1007/978-1-4614-3523-5_29.
(28) Aubay, E.; Gourier, D. Magnetic Bistability and Overhauser Shift of Conduction Electrons in Gallium Oxide. *Phys. Rev. B* **1993**, *47* (22), 15023–15036. https://doi.org/10.1103/PhysRevB.47.15023.
(29) Lappa, M. Review: Possible Strategies for the Control and Stabilization of Marangoni Flow in Laterally Heated Floating Zones. *Fluid Dynamics and Materials Processing* **2005**, *1*, 171–187. https://doi.org/10.3970/fdmp.2005.001.171.
(30) Czochralski, J. Ein Neues Verfahren Zur Messung Der Kristallisationsgeschwindigkeit Der Metalle. *Zeitschrift für Physikalische Chemie* **1918**, *92U* (1), 219–221. https://doi.org/10.1515/zpch-1918-9212.
(31) LaBelle, H. E.; Mlavsky, A. I. Growth of Controlled Profile Crystals from the Melt: Part I - Sapphire Filaments. *Materials Research Bulletin* **1971**, *6* (7), 571–579. https://doi.org/10.1016/0025-5408(71)90006-7.
(32) Higashiwaki, M.; Murakami, H.; Kumagai, Y.; Kuramata, A. Current Status of Ga_2O_3 Power Devices. *Jpn. J. Appl. Phys.* **2016**, *55* (12), 1202A1. https://doi.org/10.7567/JJAP.55.1202A1.
(33) Tak, B. R.; Kumar, S.; Kapoor, A. K.; Wang, D.; Li, X.; Sun, H.; Singh, R. Recent Advances in the Growth of Gallium Oxide Thin Films Employing Various Growth Techniques—a Review. *J. Phys. D: Appl. Phys.* **2021**, *54* (45), 453002. https://doi.org/10.1088/1361-6463/ac1af2.
(34) Wang, C.; Li, S.-W.; Fan, W.-H.; Zhang, Y.-C.; Zhang, X.-Y.; Guo, R.-R.; Lin, H.-J.; Lien, S.-Y.; Zhu, W.-Z. Structural, Optical and Morphological Evolution of Ga2O3/Al2O3 (0001) Films Grown at Various Temperatures by Pulsed Laser Deposition. *Ceramics International* **2021**, *47* (21), 29748–29757. https://doi.org/10.1016/j.ceramint.2021.07.147.
(35) Franchi, S. Molecular Beam Epitaxy. In *Molecular Beam Epitaxy*; Elsevier, 2013; pp 1–46. https://doi.org/10.1016/B978-0-12-387839-7.00001-4.
(36) Víllora, E. G.; Shimamura, K.; Kitamura, K.; Aoki, K. Rf-Plasma-Assisted Molecular-Beam Epitaxy of β-Ga2O3. *Appl. Phys. Lett.* **2006**, *88* (3), 031105. https://doi.org/10.1063/1.2164407.
(37) Oshima, T.; Arai, N.; Suzuki, N.; Ohira, S.; Fujita, S. Surface Morphology of Homoepitaxial β-Ga2O3 Thin Films Grown by Molecular Beam Epitaxy. *Thin Solid Films* **2008**, *516* (17), 5768–5771. https://doi.org/10.1016/j.tsf.2007.10.045.
(38) Xiu, X.; Zhang, L.; Li, Y.; Xiong, Z.; Zhang, R.; Zheng, Y. Application of Halide Vapor Phase Epitaxy for the Growth of Ultra-Wide Band Gap Ga_2O_3. *J. Semicond.* **2019**, *40* (1), 011805. https://doi.org/10.1088/1674-4926/40/1/011805.
(39) Fujito, K.; Kubo, S.; Nagaoka, H.; Mochizuki, T.; Namita, H.; Nagao, S. Bulk GaN Crystals Grown by HVPE. *Journal of Crystal Growth* **2009**, *311* (10), 3011–3014. https://doi.org/10.1016/j.jcrysgro.2009.01.046.
(40) Tasi, C.-T.; Wang, W.-K.; Tsai, T.-Y.; Huang, S.-Y.; Horng, R.-H.; Wuu, D.-S. Reduction of Defects in AlGaN Grown on Nanoscale-Patterned Sapphire Substrates by Hydride Vapor Phase Epitaxy. *Materials* **2017**, *10* (6), 605. https://doi.org/10.3390/ma10060605.
(41) Murakami, H.; Nomura, K.; Goto, K.; Sasaki, K.; Kawara, K.; Thieu, Q. T.; Togashi, R.; Kumagai, Y.; Higashiwaki, M.; Kuramata, A.; Yamakoshi, S.; Monemar, B.; Koukitu, A. Homoepitaxial Growth of β-Ga_2O_3 Layers by Halide Vapor Phase Epitaxy. *Appl. Phys. Express* **2015**, *8* (1), 015503. https://doi.org/10.7567/APEX.8.015503.
(42) Hachem, K.; Ansari, M. J.; Saleh, R. O.; Kzar, H. H.; Al-Gazally, M. E.; Altimari, U. S.; Hussein, S. A.; Mohammed, H. T.; Hammid, A. T.; Kianfar, E. Methods of Chemical Synthesis in the Synthesis

of Nanomaterial and Nanoparticles by the Chemical Deposition Method: A Review. *BioNanoSci.* **2022**, *12* (3), 1032–1057. https://doi.org/10.1007/s12668-022-00996-w.
(43) Nunes, D.; Pimentel, A.; Santos, L.; Barquinha, P.; Pereira, L.; Fortunato, E.; Martins, R. Synthesis, Design, and Morphology of Metal Oxide Nanostructures. In *Metal Oxide Nanostructures*; Elsevier, 2019; pp 21–57. https://doi.org/10.1016/B978-0-12-811512-1.00002-3.
(44) Yoshimura, M.; Byrappa, K. Hydrothermal Processing of Materials: Past, Present and Future. *J Mater Sci* **2008**, *43* (7), 2085–2103. https://doi.org/10.1007/s10853-007-1853-x.
(45) Walton, R. I. Subcritical Solvothermal Synthesis of Condensed Inorganic Materials. *Chem. Soc. Rev.* **2002**, *31* (4), 230–238. https://doi.org/10.1039/B105762F.
(46) Iwamoto, S.; Inoue, M. Solvothermal Synthesis of Inorganic Materials and Their Performance as Catalysts. *Journal of the Japan Petroleum Institute* **2008**, *51* (3), 143–156. https://doi.org/10.1627/jpi.51.143.
(47) Song, J.; Wang, Z.; Cheng, X.; Wang, X. State-of-Art Review of NO Reduction Technologies by CO, CH4 and H2. *Processes* **2021**, *9* (3), 563. https://doi.org/10.3390/pr9030563.
(48) Watanabe, T.; Miki, Y.; Miyahara, Y.; Masuda, T.; Deguchi, H.; Kanai, H.; Hosokawa, S.; Wada, K.; Inoue, M. Enhancement of the Activities of γ-Ga2O3–Al2O3 Catalysts for Methane-SCR of NO by Treatment with NH3. *Catal Lett* **2011**, *141* (9), 1338. https://doi.org/10.1007/s10562-011-0654-7.
(49) Reddy, L. S.; Ko, Y. H.; Yu, J. S. Hydrothermal Synthesis and Photocatalytic Property of β-Ga2O3 Nanorods. *Nanoscale Res Lett* **2015**, *10* (1), 364. https://doi.org/10.1186/s11671-015-1070-5.
(50) Danks, A. E.; Hall, S. R.; Schnepp, Z. The Evolution of 'Sol–Gel' Chemistry as a Technique for Materials Synthesis. *Mater. Horiz.* **2016**, *3* (2), 91–112. https://doi.org/10.1039/C5MH00260E.
(51) Zha, J.; Roggendorf, H. Sol–Gel Science, the Physics and Chemistry of Sol–Gel Processing, Ed. by C. J. Brinker and G. W. Scherer, Academic Press, Boston 1990, Xiv, 908 Pp., Bound—ISBN 0-12-134970-5. *Advanced Materials* **1991**, *3* (10), 522–522. https://doi.org/10.1002/adma.19910031025.
(52) Lin, J.; Yu, M.; Lin, C.; Liu, X. Multiform Oxide Optical Materials via the Versatile Pechini-Type Sol−Gel Process: Synthesis and Characteristics. *J. Phys. Chem. C* **2007**, *111* (16), 5835–5845. https://doi.org/10.1021/jp070062c.
(53) Pechini, M. P. Method of Preparing Lead and Alkaline Earth Titanates and Niobates and Coating Method Using the Same to Form a Capacitor. US3330697A, July 11, 1967.
(54) Shen, W. Y.; Pang, M. L.; Lin, J.; Fang, J. Host-Sensitized Luminescence of Dy3 + in Nanocrystalline β - Ga2 O 3 Prepared by a Pechini-Type Sol-Gel Process. *J. Electrochem. Soc.* **2004**, *152* (2), H25. https://doi.org/10.1149/1.1847674.
(55) Fleischer, M.; Giber, J.; Meixner, H. H2-Induced Changes in Electrical Conductance of β-Ga2O3 Thin-Film Systems. *Appl. Phys. A* **1992**, *54* (6), 560–566. https://doi.org/10.1007/BF00324340.
(56) Schwebel, T.; Fleischer, M.; Meixner, H.; Kohl, C.-D. CO-Sensor for Domestic Use Based on High Temperature Stable Ga2O3 Thin Films. *Sensors and Actuators B: Chemical* **1998**, *49* (1), 46–51. https://doi.org/10.1016/S0925-4005(97)00334-1.
(57) Huang, Y.; Yue, S.; Wang, Z.; Wang, Q.; Shi, C.; Xu, Z.; Bai, X. D.; Tang, C.; Gu, C. Preparation and Electrical Properties of Ultrafine Ga2O3 Nanowires. *J. Phys. Chem. B* **2006**, *110* (2), 796–800. https://doi.org/10.1021/jp055844p.
(58) Arnold, S. P.; Prokes, S. M.; Perkins, F. K.; Zaghloul, M. E. Design and Performance of a Simple, Room-Temperature Ga2O3 Nanowire Gas Sensor. *Appl. Phys. Lett.* **2009**, *95* (10), 103102. https://doi.org/10.1063/1.3223617.
(59) Higashiwaki, M.; Sasaki, K.; Kuramata, A.; Masui, T.; Yamakoshi, S. Development of Gallium Oxide Power Devices: Development of Gallium Oxide Power Devices. *Phys. Status Solidi A* **2014**, *211* (1), 21–26. https://doi.org/10.1002/pssa.201330197.
(60) Oishi, T.; Koga, Y.; Harada, K.; Kasu, M. High-Mobility β-Ga_2O_3 Single Crystals Grown by Edge-Defined Film-Fed Growth Method and Their Schottky Barrier Diodes with Ni Contact. *Appl. Phys. Express* **2015**, *8* (3), 031101. https://doi.org/10.7567/APEX.8.031101.
(61) Higashiwaki, M.; Sasaki, K.; Kamimura, T.; Hoi Wong, M.; Krishnamurthy, D.; Kuramata, A.; Masui, T.; Yamakoshi, S. Depletion-Mode Ga_2O_3 Metal-Oxide-Semiconductor Field-Effect Transistors on β-Ga_2O_3 (010) Substrates and Temperature Dependence of Their Device Characteristics. *Appl. Phys. Lett.* **2013**, *103* (12), 123511. https://doi.org/10.1063/1.4821858.
(62) Higashiwaki, M.; Sasaki, K.; Kuramata, A.; Masui, T.; Yamakoshi, S. Gallium Oxide (Ga_2O_3) Metal-Semiconductor Field-Effect Transistors on Single-Crystal β-Ga_2O_3 (010) Substrates. *Appl. Phys. Lett.* **2012**, *100* (1), 013504. https://doi.org/10.1063/1.3674287.

(63) Kim, J. H.; Yoon, K. H. Alternating Current Electroluminescence and Structural Properties of Thin Film Gallium Oxide Doped with Manganese. *J. Korean Phy. Soc.* **2008**, *53* (2), 818–821. https://doi.org/10.3938/jkps.53.818.
(64) Stodilka, D.; Kitai, A. H.; Huang, Z.; Cook, K. 4.2: High Brightness Red Emitting Ga_2O_3 : Eu Electroluminescent Phosphor. *SID Symposium Digest of Technical Papers* **2000**, *31* (1), 11–13. https://doi.org/10.1889/1.1832880.
(65) Xiao, T.; Kitai, A. H.; Liu, G.; Nakua, A.; Barbier, J. Thin Film Electroluminescence in Highly Anisotropic Oxide Materials. *Appl. Phys. Lett.* **1998**, *72* (25), 3356–3358. https://doi.org/10.1063/1.121602.
(66) Feng, P.; Zhang, J. Y.; Li, Q. H.; Wang, T. H. Individual β-Ga2O3 Nanowires as Solar-Blind Photodetectors. *Appl. Phys. Lett.* **2006**, *88* (15), 153107. https://doi.org/10.1063/1.2193463.
(67) Li, L.; Auer, E.; Liao, M.; Fang, X.; Zhai, T.; Gautam, U. K.; Lugstein, A.; Koide, Y.; Bando, Y.; Golberg, D. Deep-Ultraviolet Solar-Blind Photoconductivity of Individual Gallium Oxide Nanobelts. *Nanoscale* **2011**, *3* (3), 1120. https://doi.org/10.1039/c0nr00702a.
(68) Park, H.; Choi, J. H.; Choi, K. M.; Lee, D. K.; Kang, J. K. Highly Porous Gallium Oxide with a High CO2 Affinity for the Photocatalytic Conversion of Carbon Dioxide into Methane. *J. Mater. Chem.* **2012**, *22* (12), 5304–5307. https://doi.org/10.1039/C2JM30337J.
(69) Collins, S. E.; Baltanás, M. A.; Delgado, J. J.; Borgna, A.; Bonivardi, A. L. CO2 Hydrogenation to Methanol on Ga2O3-Pd/SiO2 Catalysts: Dual Oxide-Metal Sites or (Bi)Metallic Surface Sites? *Catalysis Today* **2021**, *381*, 154–162. https://doi.org/10.1016/j.cattod.2020.07.048.
(70) Shrestha, N. K.; Lee, K.; Kirchgeorg, R.; Hahn, R.; Schmuki, P. Self-Organization and Zinc Doping of Ga2O3 Nanoporous Architecture: A Potential Nano-Photogenerator for Hydrogen. *Electrochemistry Communications* **2013**, *35*, 112–115. https://doi.org/10.1016/j.elecom.2013.08.011.
(71) Chang, S.-J.; Wu, Y.-L.; Weng, W.-Y.; Lin, Y.-H.; Hsieh, W.-K.; Sheu, J.-K.; Hsu, C.-L. Ga2O3 Films for Photoelectrochemical Hydrogen Generation. *J. Electrochem. Soc.* **2014**, *161* (9), H508. https://doi.org/10.1149/2.0471409jes.
(72) Gnanamani, M. K.; Jacobs, G.; Shafer, W. D.; Hopps, S. D.; Davis, B. H. Dehydration of Pentanediol over CeO_2, CeO_2-Ga_2O_3, and CeO_2-In_2O_3. *ChemistrySelect* **2017**, *2* (14), 4150–4156. https://doi.org/10.1002/slct.201700758.
(73) Ladera, R.; Pérez-Alonso, F. J.; González-Carballo, J. M.; Ojeda, M.; Rojas, S.; Fierro, J. L. G. Catalytic Valorization of CO2 via Methanol Synthesis with Ga-Promoted Cu–ZnO–ZrO2 Catalysts. *Applied Catalysis B: Environmental* **2013**, *142–143*, 241–248. https://doi.org/10.1016/j.apcatb.2013.05.019.
(74) Hengne, A. M.; Yuan, D. J.; Date, N. S.; Saih, Y.; Kamble, S. P.; Rode, C. V.; Huang, K.-W. Preparation and Activity of Copper–Gallium Nanocomposite Catalysts for Carbon Dioxide Hydrogenation to Methanol. *Ind. Eng. Chem. Res.* **2019**, *58* (47), 21331–21340. https://doi.org/10.1021/acs.iecr.9b04083.
(75) Dai, H.; Zhang, A.; Xiong, S.; Xiao, X.; Zhou, C.; Pan, Y. The Catalytic Performance of Ga_2O_3 −CeO_2 Composite Oxides over Reverse Water Gas Shift Reaction. *ChemCatChem* **2022**, *14* (6). https://doi.org/10.1002/cctc.202200049.
(76) Freeman, D.; Wells, R. P. K.; Hutchings, G. J. Conversion of Methanol to Hydrocarbons over Ga2O3/H-ZSM-5 and Ga2O3/WO3 Catalysts. *Journal of Catalysis* **2002**, *205* (2), 358–365. https://doi.org/10.1006/jcat.2001.3446.
(77) Castro-Fernández, P.; Mance, D.; Liu, C.; Moroz, I. B.; Abdala, P. M.; Pidko, E. A.; Copéret, C.; Fedorov, A.; Müller, C. R. Propane Dehydrogenation on Ga2O3-Based Catalysts: Contrasting Performance with Coordination Environment and Acidity of Surface Sites. *ACS Catal.* **2021**, *11* (2), 907–924. https://doi.org/10.1021/acscatal.0c05009.
(78) *Ethylene production capacity globally 2025*. Statista. https://www.statista.com/statistics/1067372/global-ethylene-production-capacity/ (accessed 2022-05-04).
(79) Nakagawa, K.; Kajita, C.; Okumura, K.; Ikenaga, N.; Nishitani-Gamo, M.; Ando, T.; Kobayashi, T.; Suzuki, T. Role of Carbon Dioxide in the Dehydrogenation of Ethane over Gallium-Loaded Catalysts. *Journal of Catalysis* **2001**, *203* (1), 87–93. https://doi.org/10.1006/jcat.2001.3306.
(80) Gärtner, C. A.; van Veen, A. C.; Lercher, J. A. Oxidative Dehydrogenation of Ethane: Common Principles and Mechanistic Aspects. *ChemCatChem* **2013**, *5* (11), 3196–3217. https://doi.org/10.1002/cctc.201200966.
(81) Batchu, S. P.; Wang, H.-L.; Chen, W.; Zheng, W.; Caratzoulas, S.; Lobo, R. F.; Vlachos, D. G. Ethane Dehydrogenation on Single and Dual Centers of Ga-Modified γ-Al_2O_3. *ACS Catal.* **2021**, *11* (3), 1380–1391. https://doi.org/10.1021/acscatal.0c03536.

(82) Chen, W.; Cohen, M.; Yu, K.; Wang, H.-L.; Zheng, W.; Vlachos, D. G. Experimental Data-Driven Reaction Network Identification and Uncertainty Quantification of CO2-Assisted Ethane Dehydrogenation over Ga2O3/Al2O3. *Chemical Engineering Science* **2021**, *237*, 116534. https://doi.org/10.1016/j.ces.2021.116534.
(83) Najari, S. Oxidative Dehydrogenation of Ethane: Catalytic and Mechanistic Aspects and Future Trends. *Chem Soc Rev* **2021**, 42.
(84) Nakagawa, K.; Okamura, M.; Ikenaga, N.; Suzuki, T.; Nakagawa, K.; Okamura, M.; Suzuki, T.; Kobayashi, T.; Kobayashi, T. Dehydrogenation of Ethane over Gallium Oxide in the Presence of Carbon Dioxide. *Chem. Commun.* **1998**, No. 9, 1025–1026. https://doi.org/10.1039/a800184g.
(85) Yan, B.; Yao, S.; Kattel, S.; Wu, Q.; Xie, Z.; Gomez, E.; Liu, P.; Su, D.; Chen, J. G. Active Sites for Tandem Reactions of CO2 Reduction and Ethane Dehydrogenation. *Proceedings of the National Academy of Sciences* **2018**, *115* (33), 8278–8283. https://doi.org/10.1073/pnas.1806950115.
(86) Atanga, M. A.; Rezaei, F.; Jawad, A.; Fitch, M.; Rownaghi, A. A. Oxidative Dehydrogenation of Propane to Propylene with Carbon Dioxide. *Applied Catalysis B: Environmental* **2018**, *220*, 429–445. https://doi.org/10.1016/j.apcatb.2017.08.052.
(87) Branco, J. B.; Ferreira, A. C.; Leal, J. P. Light Hydrocarbons Production over Bimetallic Calcium–Actinide Oxide Catalysts Using N2O as Oxidant. *Journal of Molecular Catalysis A: Chemical* **2014**, *390*, 45–51. https://doi.org/10.1016/j.molcata.2014.03.005.
(88) Kondratenko, E. V.; Pérez-Ramírez, J. Transient Studies of Direct N2O Decomposition over Pt–Rh Gauze Catalyst. Mechanistic and Kinetic Aspects of Oxygen Formation. *Catalysis Letters* **2003**, *91* (3), 211–216. https://doi.org/10.1023/B:CATL.0000007157.87417.fe.
(89) Nakagawa, K.; Kajita, C.; Ide, Y.; Okamura, M.; Kato, S.; Kasuya, H.; Ikenaga, N.; Kobayashi, T.; Suzuki, T. Promoting Effect of Carbon Dioxide on the Dehydrogenation and Aromatization of Ethane over Gallium-loaded Catalysts. *Catalysis Letters* **2000**, *64* (2), 215–221. https://doi.org/10.1023/A:1019047306179.
(90) Shen, Z.; Liu, J.; Xu, H.; Yue, Y.; Hua, W.; Shen, W. Dehydrogenation of Ethane to Ethylene over a Highly Efficient Ga2O3/HZSM-5 Catalyst in the Presence of CO2. *Applied Catalysis A: General* **2009**, *356* (2), 148–153. https://doi.org/10.1016/j.apcata.2008.12.038.
(91) Al-Ghamdi, S. A.; Hossain, M. M.; de Lasa, H. I. Kinetic Modeling of Ethane Oxidative Dehydrogenation over VOx/Al2O3 Catalyst in a Fluidized-Bed Riser Simulator. *Ind. Eng. Chem. Res.* **2013**, *52* (14), 5235–5244. https://doi.org/10.1021/ie303305c.
(92) Grabowski, R.; Słoczyński, J. Kinetics of Oxidative Dehydrogenation of Propane and Ethane on VOx/SiO2 Pure and with Potassium Additive. *Chemical Engineering and Processing: Process Intensification* **2005**, *44* (10), 1082–1093. https://doi.org/10.1016/j.cep.2005.03.002.
(93) Rahman, F.; Loughlin, K. F.; Al-Saleh, M. A.; Saeed, M. R.; Tukur, N. M.; Hossain, M. M.; Karim, K.; Mamedov, A. Kinetics and Mechanism of Partial Oxidation of Ethane to Ethylene and Acetic Acid over MoV Type Catalysts. *Applied Catalysis A: General* **2010**, *375* (1), 17–25. https://doi.org/10.1016/j.apcata.2009.11.026.
(94) Klose, F.; Joshi, M.; Hamel, C.; Seidel-Morgenstern, A. Selective Oxidation of Ethane over a VOx/γ-Al2O3 Catalyst – Investigation of the Reaction Network. *Applied Catalysis A: General* **2004**, *260* (1), 101–110. https://doi.org/10.1016/j.apcata.2003.10.005.
(95) Che-Galicia, G.; Quintana-Solórzano, R.; Ruiz-Martínez, R. S.; Valente, J. S.; Castillo-Araiza, C. O. Kinetic Modeling of the Oxidative Dehydrogenation of Ethane to Ethylene over a MoVTeNbO Catalytic System. *Chemical Engineering Journal* **2014**, *252*, 75–88. https://doi.org/10.1016/j.cej.2014.04.042.
(96) Sinev, M. Yu. Free Radicals as Intermediates in Catalytic Oxidation of Light Alkanes: New Opportunities. *Res. Chem. Intermed.* **2006**, *32* (3), 205–215. https://doi.org/10.1163/156856706777346471.
(97) Wang, S.; Murata, K.; Hayakawa, T.; Suzuki, K. Oxidative Dehydrogenation of Ethane Over Zirconia-Supported Lithium Chloride Catalysts. *Chemical Engineering & Technology* **2000**, *23* (12), 1099–1103. https://doi.org/10.1002/1521-4125(200012)23:12<1099::AID-CEAT1099>3.0.CO;2-W.
(98) Kumar, C. P.; Gaab, S.; Müller, T. E.; Lercher, J. A. Oxidative Dehydrogenation of Light Alkanes on Supported Molten Alkali Metal Chloride Catalysts. *Top Catal* **2008**, *50* (1), 156–167. https://doi.org/10.1007/s11244-008-9102-3.
(99) Au, C. T.; Zhou, X. P.; Wan, H. L. The Activation of O2 and the Oxidative Dehydrogenation of C2H6 over SmOF Catalyst. *Catal Lett* **1996**, *40* (1), 101–104. https://doi.org/10.1007/BF00807464.

(100) Rebeilleau-Dassonneville, M.; Rosini, S.; Veen, A. C. van; Farrusseng, D.; Mirodatos, C. Oxidative Activation of Ethane on Catalytic Modified Dense Ionic Oxygen Conducting Membranes. *Catalysis Today* **2005**, *104* (2), 131–137. https://doi.org/10.1016/j.cattod.2005.03.071.
(101) Maffia, G. J.; Gaffney, A. M.; Mason, O. M. Techno-Economic Analysis of Oxidative Dehydrogenation Options. *Top Catal* **2016**, *59* (17), 1573–1579. https://doi.org/10.1007/s11244-016-0677-9.
(102) Zhang, R.; Wang, H.; Tang, S.; Liu, C.; Dong, F.; Yue, H.; Liang, B. Photocatalytic Oxidative Dehydrogenation of Ethane Using CO2 as a Soft Oxidant over Pd/TiO2 Catalysts to C2H4 and Syngas. *ACS Catal.* **2018**, *8* (10), 9280–9286. https://doi.org/10.1021/acscatal.8b02441.
(103) Bolotov, V. A.; Chesnokov, V. V.; Tanashev, Y. Y.; Parmon, V. N. The Oxidative Dehydrogenation of Ethane: Convectional vs Microwave Heating of Ba - Containing Catalysts. *Chemical Engineering and Processing - Process Intensification* **2018**, *129*, 103–108. https://doi.org/10.1016/j.cep.2018.05.006.
(104) James, O. O.; Mandal, S.; Alele, N.; Chowdhury, B.; Maity, S. Lower Alkanes Dehydrogenation: Strategies and Reaction Routes to Corresponding Alkenes. *Fuel Processing Technology* **2016**, *149*, 239–255. https://doi.org/10.1016/j.fuproc.2016.04.016.
(105) Zhao, B.; Pan, Y.; Liu, C. The Promotion Effect of CeO2 on CO2 Adsorption and Hydrogenation over Ga2O3. *Catalysis Today* **2012**, *194* (1), 60–64. https://doi.org/10.1016/j.cattod.2012.05.011.
(106) Baumann, T. F.; Gash, A. E.; Satcher, J. H. A Robust Approach to Inorganic Aerogels: The Use of Epoxides in Sol–Gel Synthesis. In *Aerogels Handbook*; Aegerter, M. A., Leventis, N., Koebel, M. M., Eds.; Springer New York: New York, NY, 2011; pp 155–170. https://doi.org/10.1007/978-1-4419-7589-8_8.
(107) Gash, A. E.; Tillotson, T. M.; Satcher, J. H.; Poco, J. F.; Hrubesh, L. W.; Simpson, R. L. Use of Epoxides in the Sol−Gel Synthesis of Porous Iron(III) Oxide Monoliths from Fe(III) Salts. *Chem. Mater.* **2001**, *13* (3), 999–1007. https://doi.org/10.1021/cm0007611.
(108) Yong, L.; WenJie, S. Morphology-Dependent Nanocatalysis on Metal Oxides. *Sci. China-Chem.* **2012**, *55* (12), 2485–2496. https://doi.org/10.1007/s11426-012-4565-2.
(109) Xue, J.; Wu, T.; Dai, Y.; Xia, Y. Electrospinning and Electrospun Nanofibers: Methods, Materials, and Applications. *Chem. Rev.* **2019**, *119* (8), 5298–5415. https://doi.org/10.1021/acs.chemrev.8b00593.
(110) Kakoria, A.; Devi, B.; Anand, A.; Halder, A.; Koner, R. R.; Sinha-Ray, S. Gallium Oxide Nanofibers for Hydrogen Evolution and Oxygen Reduction. *ACS Appl. Nano Mater.* **2019**, *2* (1), 64–74. https://doi.org/10.1021/acsanm.8b01651.
(111) Park, K.-W.; Cho, W.-J. High-Performance IGZO Nanowire-Based Field-Effect Transistors with Random-Network Channels by Electrospun PVP Nanofiber Template Transfer. *Polymers* **2022**, *14* (3), 651. https://doi.org/10.3390/polym14030651.
(112) Deliormanlı, A. M. Electrospun Cerium and Gallium-Containing Silicate Based 13-93 Bioactive Glass Fibers for Biomedical Applications. *Ceramics International* **2016**, *42* (1), 897–906. https://doi.org/10.1016/j.ceramint.2015.09.016.
(113) Cherstiouk, O. V.; Simonov, P. A.; Zaikovskii, V. I.; Savinova, E. R. CO Monolayer Oxidation at Pt Nanoparticles Supported on Glassy Carbon Electrodes. *Journal of Electroanalytical Chemistry* **2003**, *554–555*, 241–251. https://doi.org/10.1016/S0022-0728(03)00198-0.
(114) Maillard, F.; Eikerling, M.; Cherstiouk, O. V.; Schreier, S.; Savinova, E.; Stimming, U. Size Effects on Reactivity of Pt Nanoparticles in CO Monolayer Oxidation: The Role of Surface Mobility. *Faraday Disc.* **2004**, *125*, 357. https://doi.org/10.1039/b303911k.
(115) Leng, Y. *Materials Characterization: Introduction to Microscopic and Spectroscopic Methods*, 2. ed.; Wiley-VCH: Weinheim, 2013.
(116) Components in a SEM. *Nanoscience Instruments*.
(117) *Powder Diffraction: Theory and Practice*; Dinnebier, R. E., Billinge, S. J. L., Eds.; Royal Society of Chemistry: Cambridge, 2008.
(118) Scherrer, P. Bestimmung der Größe und der inneren Struktur von Kolloidteilchen mittels Röntgenstrahlen. *Nachrichten von der Gesellschaft der Wissenschaften zu Göttingen, Mathematisch-Physikalische Klasse* **1918**, *1918*, 98–100.
(119) Uvarov, V.; Popov, I. Metrological Characterization of X-Ray Diffraction Methods at Different Acquisition Geometries for Determination of Crystallite Size in Nano-Scale Materials. *Materials Characterization* **2013**, *85*, 111–123. https://doi.org/10.1016/j.matchar.2013.09.002.
(120) Jaroniec, M.; Kruk, M.; Sayari, A. Adsorption Methods for Characterization of Surface and Structural Properties of Mesoporous Molecular Sieves. In *Studies in Surface Science and Catalysis*; Bonneviot, L., Béland, F., Danumah, C., Giasson, S., Kaliaguine, S., Eds.; Mesoporous

Molecular Sieves 1998; Elsevier, 1998; Vol. 117, pp 325–332. https://doi.org/10.1016/S0167-2991(98)81008-2.
(121) Naderi, M. Chapter Fourteen - Surface Area: Brunauer–Emmett–Teller (BET). In *Progress in Filtration and Separation*; Tarleton, S., Ed.; Academic Press: Oxford, 2015; pp 585–608. https://doi.org/10.1016/B978-0-12-384746-1.00014-8.
(122) Armandía, M. A.; Borau, V.; Jiménez, C.; Marinas, J. M.; Porras, A.; Urbano, F. J. Dehydration-Dehydrogenation of 2-Propanol as a Model Reaction for Acid-Base Characterization of Catalysts. *React Kinet Catal Lett* **1994**, *53* (2), 397–404. https://doi.org/10.1007/BF02073048.
(123) Wang, J. A.; Chen, L. F.; López, T.; Gómez, R.; Novaro, O. Dehydrogenation and Dehydration of Isopropanol Catalyzed with Sol-Gel MgO-Al2O3 Oxide. In *Emerging Fields in Sol-Gel Science and Technology*; López, T. M., Avnir, D., Aegerter, M., Eds.; Springer US: Boston, MA, 2003; pp 78–83. https://doi.org/10.1007/978-1-4615-0449-8_8.
(124) Polychronopoulou, K.; Jaoudé, M. A. Nano-Architectural Advancement of CeO2-Driven Catalysis via Electrospinning. *Surface and Coatings Technology* **2018**, *350*, 245–280. https://doi.org/10.1016/j.surfcoat.2018.07.014.
(124) Liao, Y. *Practical Electron Microscopy and Database: www.globalsino.com/EM/*; 2013.
(126) *X-ray Transition Energies - Search Result*. https://physics.nist.gov/cgi-bin/XrayTrans/search.pl?element=Ga&lower=&upper=&units=eV (accessed 2022-10-08).
(127) Callister, W. D. *Materials Science and Engineering: An Introduction*, 7th ed.; John Wiley & Sons: New York, 2007.
(128) *Database of Ionic Radii*. http://abulafia.mt.ic.ac.uk/shannon/ptable.php (accessed 2022-10-15).
(129) Collins, S.; Finos, G.; Alcántara, R.; del Rio, E.; Bernal, S.; Bonivardi, A. Effect of Gallia Doping on the Acid–Base and Redox Properties of Ceria. *Applied Catalysis A: General* **2010**, *388* (1–2), 202–210. https://doi.org/10.1016/j.apcata.2010.08.050.
(130) Fornero, E. L.; Vecchietti, J.; Boucinha Rodrigues, M.; Hernández-Garrido, J. C.; Bonivardi, A. L. Cooperative Role of Cobalt and Gallium under the Ethanol Steam Reforming on Co/CeGaOx. *International Journal of Hydrogen Energy* **2022**, *47* (41), 18018–18031. https://doi.org/10.1016/j.ijhydene.2022.03.278.
(131) Vilé, G.; Dähler, P.; Vecchietti, J.; Baltanás, M.; Collins, S.; Calatayud, M.; Bonivardi, A.; Pérez-Ramírez, J. Promoted Ceria Catalysts for Alkyne Semi-Hydrogenation. *Journal of Catalysis* **2015**, *324*, 69–78. https://doi.org/10.1016/j.jcat.2015.01.020.
(132) Vecchietti, J.; Collins, S.; Xu, W.; Barrio, L.; Stacchiola, D.; Calatayud, M.; Tielens, F.; Delgado, J. J.; Bonivardi, A. Surface Reduction Mechanism of Cerium–Gallium Mixed Oxides with Enhanced Redox Properties. *J. Phys. Chem. C* **2013**, *117* (17), 8822–8831. https://doi.org/10.1021/jp400285b.
(133) Hasni, W.; Boukortt, A.; Bekkouche, B.; Kacimi, S.; Djermouni, M.; Zaoui, A. B-Cation Effect on the Electronic and Magnetic Properties of CeBO3 (B=Ga, In) Compounds from First Principles Study. *Physica B: Condensed Matter* **2012**, *407* (5), 901–906. https://doi.org/10.1016/j.physb.2011.12.113.
(134) Shishido, T.; Zheng, Y. T.; Horiuchi, H.; Yoshikawa, A.; Hosoya, S.; Tozawa, S.; Saito, A.; Tanaka, M.; Fukuda, T. Crystal structure of perovskite type CeGaO3 synthesized by arc- and skull- melting methods. *Nippon Kagaku Kaishi* **1996**, No. 11, 991–994. https://doi.org/10.1246/nikkashi.1996.991.
(135) Shishido, T.; Zheng, Y.; Saito, A.; Horiuchi, H.; Kudou, K.; Okada, S.; Fukuda, T. Microstructure, Thermal Properties and Hardness of the CeMO3 (M=Al,Ga) Synthesized by Arc-Melting Method. *Journal of Alloys and Compounds* **1997**, *260* (1), 88–92. https://doi.org/10.1016/S0925-8388(97)00141-2.
(136) Leonov, A. I.; Andreeva, A. V.; Shvaiko-Svaikovskii, V. E.; Keler, E. K. High-temperature chemistry of cerium in systems of CeO2-Al2O3, -Cr2O3, -Ga2O3. *Izv. Akad. Nauk SSSR, Neorg. Mater.* **1966**, *2* (3), 517–523.
(137) Stan, M.; Armstrong, T. J.; Butt, D. P.; Wallace, T. C.; Park, Y. S.; Haertling, C. L.; Hartmann, T.; Jr. Hanrahan, R. J. Stability of the Perovskite Compounds in the Ce-Ga-O and Pu-Ga-O Systems. *Journal of the American Ceramic Society* **2002**, *85* (11), 2811–2816. https://doi.org/10.1111/j.1151-2916.2002.tb00533.x.
(138) Shibasaki, S.; Honishi, Y.; Nakagawa, N.; Yamazaki, M.; Mizuno, Y.; Nishida, Y.; Sugimoto, K.; Yamamoto, K. Highly Transparent Cu2O Absorbing Layer for Thin Film Solar Cells. *Appl. Phys. Lett.* **2021**, *119* (24), 242102. https://doi.org/10.1063/5.0072310.
(139) Faungnawakij, K.; Shimoda, N.; Fukunaga, T.; Kikuchi, R.; Eguchi, K. Cu-Based Spinel Catalysts CuB2O4 (B=Fe, Mn, Cr, Ga, Al, Fe0.75Mn0.25) for Steam Reforming of Dimethyl Ether. *Applied Catalysis A: General* **2008**, *341* (1), 139–145. https://doi.org/10.1016/j.apcata.2008.02.039.

(140) Gurunathan, K.; Baeg, J.-O.; Lee, S. M.; Subramanian, E.; Moon, S.-J.; Kong, K. Visible Light Active Pristine and Fe3+ Doped CuGa2O4 Spinel Photocatalysts for Solar Hydrogen Production. *International Journal of Hydrogen Energy* **2008**, *33* (11), 2646–2652. https://doi.org/10.1016/j.ijhydene.2008.03.018.
(141) Gingasu, D.; Mindru, I.; Patron, L.; Marinescu, G.; Tuna, F.; Preda, S.; Calderon-Moreno, J. M.; Andronescu, C. Synthesis of CuGa2O4 Nanoparticles by Precursor and Self-Propagating Combustion Methods. *Ceramics International* **2012**, *38* (8), 6739–6751. https://doi.org/10.1016/j.ceramint.2012.05.067.
(142) Meitzner, G. D.; Iglesia, E.; Baumgartner, J. E.; Huang, E. S. The Chemical State of Gallium in Working Alkane Dehydrocyclodimerization Catalysts. In Situ Gallium K-Edge X-Ray Absorption Spectroscopy. *Journal of Catalysis* **1993**, *140* (1), 209–225. https://doi.org/10.1006/jcat.1993.1079.
(143) Castro-Fernández, P.; Mance, D.; Liu, C.; Abdala, P. M.; Willinger, E.; Rossinelli, A. A.; Serykh, A. I.; Pidko, E. A.; Copéret, C.; Fedorov, A.; Müller, C. R. Bulk and Surface Transformations of Ga2O3 Nanoparticle Catalysts for Propane Dehydrogenation Induced by a H2 Treatment. *Journal of Catalysis* **2022**, *408*, 155–164. https://doi.org/10.1016/j.jcat.2022.02.025.
(144) Helali, Z.; Jedidi, A.; Syzgantseva, O. A.; Calatayud, M.; Minot, C. Scaling Reducibility of Metal Oxides. *Theor Chem Acc* **2017**, *136* (9), 100. https://doi.org/10.1007/s00214-017-2130-y.
(145) Li, L.; Wei, W.; Behrens, M. Synthesis and Characterization of α-, β-, and γ-Ga2o3 Prepared from Aqueous Solutions by Controlled Precipitation. *Solid State Sciences* **2012**, *14* (7), 971–981. https://doi.org/10.1016/j.solidstatesciences.2012.04.037.
(146) Giordano, F.; Trovarelli, A.; de Leitenburg, C.; Giona, M. A Model for the Temperature-Programmed Reduction of Low and High Surface Area Ceria. *Journal of Catalysis* **2000**, *193* (2), 273–282. https://doi.org/10.1006/jcat.2000.2900.
(147) Lee, K. Y.; Chae, H.-J.; Jeong, S.-Y.; Seo, G. Effect of Crystallite Size of SAPO-34 Catalysts on Their Induction Period and Deactivation in Methanol-to-Olefin Reactions. *Applied Catalysis A: General* **2009**, *369* (1), 60–66. https://doi.org/10.1016/j.apcata.2009.08.033.
(148) Tanabe, K. Chapter 5 - Correlation between Acid-Base Properties and Catalytic Activity and Selectivity. In *Solid Acids and Bases*; Tanabe, K., Ed.; Academic Press, 1970; pp 103–158. https://doi.org/10.1016/B978-0-12-683250-1.50009-2.
(149) Fairuzov, D.; Gerzeliev, I.; Maximov, A.; Naranov, E. Catalytic Dehydrogenation of Ethane: A Mini Review of Recent Advances and Perspective of Chemical Looping Technology. *Catalysts* **2021**, *11* (7), 833. https://doi.org/10.3390/catal11070833.
(150) Heracleous, E.; Lemonidou, A. A. Ni–Me–O Mixed Metal Oxides for the Effective Oxidative Dehydrogenation of Ethane to Ethylene – Effect of Promoting Metal Me. *Journal of Catalysis* **2010**, *270* (1), 67–75. https://doi.org/10.1016/j.jcat.2009.12.004.
(151) Sharma, P.; Sebastian, J.; Ghosh, S.; Creaser, D.; Olsson, L. Recent Advances in Hydrogenation of CO_2 into Hydrocarbons *via* Methanol Intermediate over Heterogeneous Catalysts. *Catal. Sci. Technol.* **2021**, *11* (5), 1665–1697. https://doi.org/10.1039/D0CY01913E.
(152) Dorner, R. W.; Hardy, D. R.; Williams, F. W.; Willauer, H. D. Heterogeneous Catalytic CO2 Conversion to Value-Added Hydrocarbons. *Energy Environ. Sci.* **2010**, *3* (7), 884–890. https://doi.org/10.1039/C001514H.

Appendix

A. SEM images of Ga-Ce bimetallic oxides, Ga_2O_3 aerogel, and $25_{wt.\%}Cu$ supported materials

Ga:Ce (1:3) – Fibres

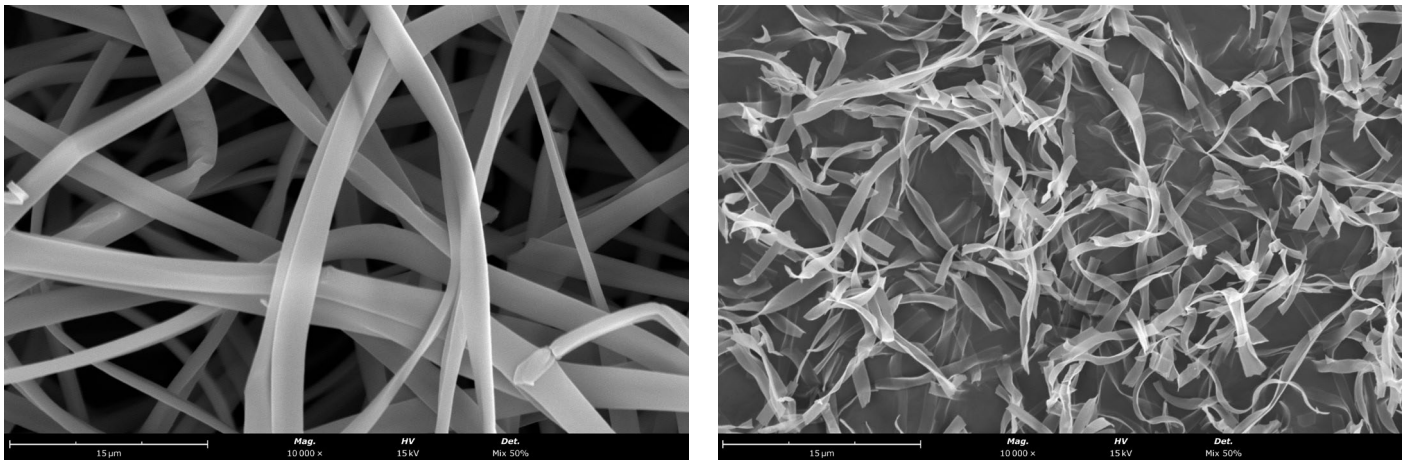

(a) (b)

Ga:Ce (3:1) – Fibres

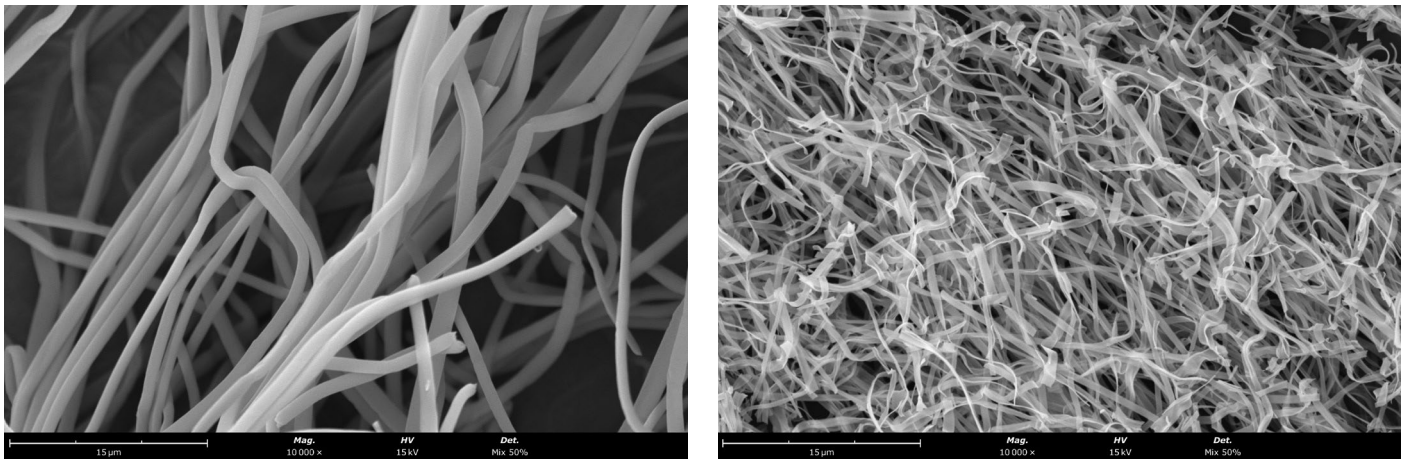

(c) (d)

Figure A1: SEM images of Ga-Ce bimetallic oxide fibres (a, c) before and (b, d) after calcination at 800 °C (magnification 10 000x).

Ga_2O_3

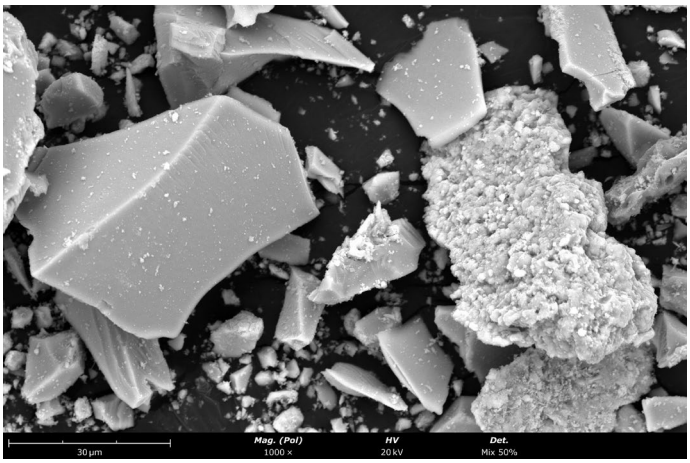

(a)

Ga:Ce (1:3)

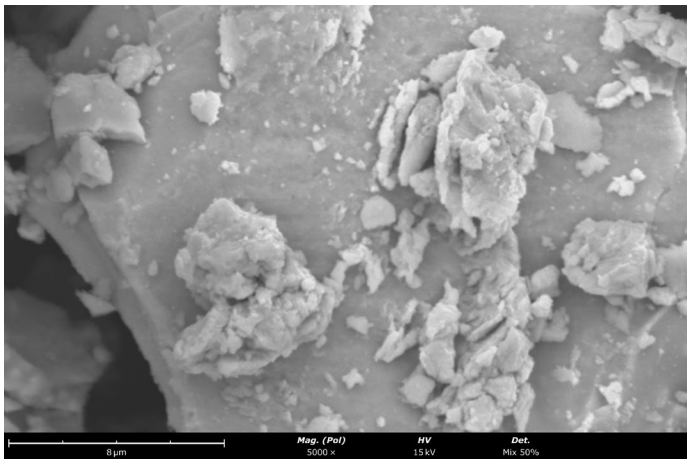

(b)

Ga:Ce (3:1)

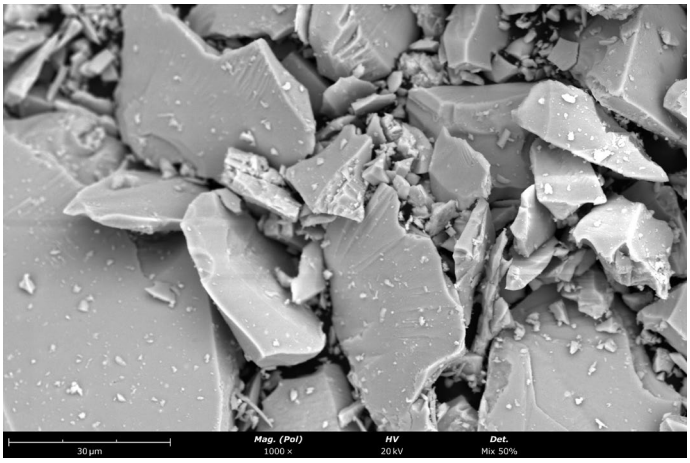

(c)

$25_{wt.\%}Cu/CeO_2$

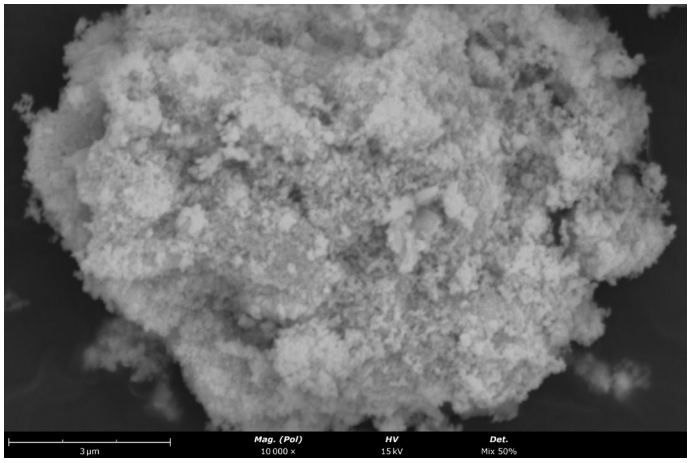

(d)

$25_{wt.\%}Cu/Ga_2O_3$

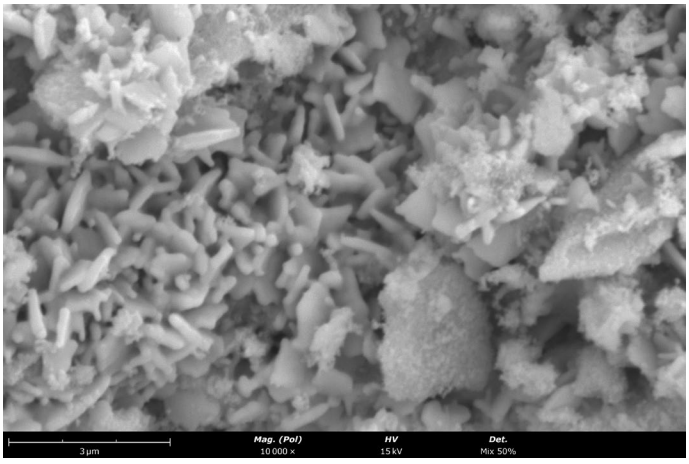

(e)

$25_{wt.\%}Cu/Ga:Ce$

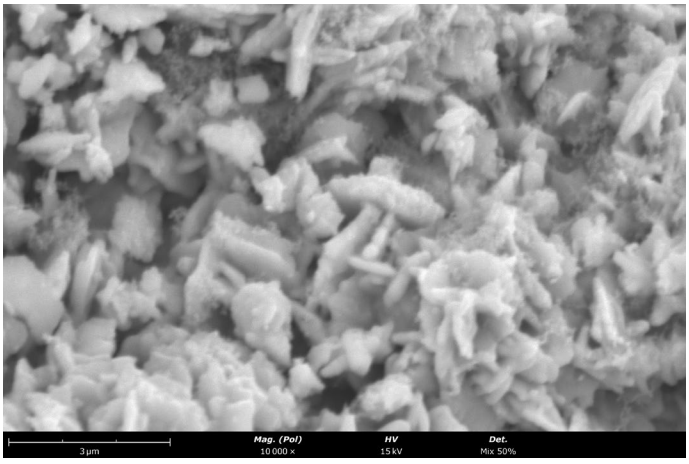

(f)

Figure A2: SEM images of (a, b, c) Ga-Ce bimetallic oxide aerogels and (d, e, f) $25_{wt.\%}Cu$ supported materials after calcination at 800 °C (magnification between 1 000x – 10 000x).

B. Preliminary catalytic studies

B.1. Hydrogenation of CO_2

The materials chosen to test the hydrogenation of CO_2 were studied under atmospheric pressure, in the temperature range 300-550 °C. A gas mixture with CO_2, H_2 and He was used, with a molar ratio H_2/CO_2 of 4, together with a GHSV of 15000 $mLCO_2/g_{cat}{\cdot}h$. These materials were the Ga-Ce bimetallic oxide aerogels, with molar ratios of 1:1 and 3:1, and the $25_{wt.\%}$Cu/Ga:Ce (1:1) (**Figure B1a**). Additionally, the last two, Ga:Ce (3:1) and 25wt.%Cu/Ga:Ce, were tested before and after an in-situ reduction treatment (**Figure B1b**). They were treated under 10% H_2 in He, at 1050 °C and 450 °C, respectively. This treatment was intended to improve their catalytic activity, since metallic species are usually assigned as the active species for this reaction.[152]

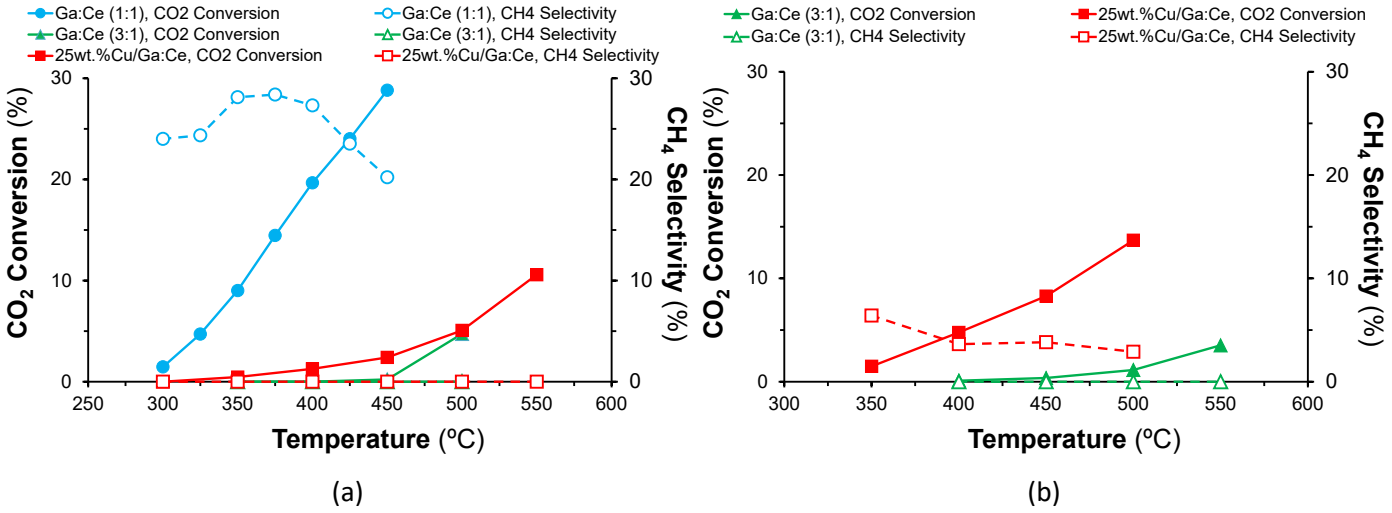

Figure B1: Effect of temperature on the methanation of CO_2 over Ga-Ce bimetallic oxide aerogels with molar ratios 1:1 and 3:1, and $25_{wt.\%}$Cu/Ga:Ce (a) without and (b) with reduction treatment. (Reaction conditions: H_2/CO_2=4, GHSV=15000 mL CO_2/g_{cat}.h).

The results here presented reveal that gallium does not seem a promising material for this reaction, as the increase in Ga_2O_3 content inhibited the activity to CO_2 conversion. So, it seems that CeO_2 has a positive effect, increasing the catalytic activity of the materials in this reaction. The reduction treatment does not show any improvement is the catalytic behaviour of Ga:Ce (3:1), which is not surprising since after H_2–TPR there is not any structural modification visible in its XDR pattern.

Regarding the copper-based material, CuO seems to deactivate the material, as the CO_2 conversion is significantly lower than the one obtained by its support, Ga:Ce (1:1). Even after the reduction treatment, the metallic Cu formed improves the catalytic activity and some CH_4 is formed, but its catalytic performance is still worse than its supports. For instance, at 400 °C, Ga:Ce (1:1) presents a CO2 conversion of 20% and CH4 selectivity of 27%, while the reduced 25wt.%Cu/Ga:Ce has 5% and 4%, respectively.

B.2. Oxidative Coupling of Methane

Using Ga-Ce bimetallic oxide with molar ratio 1:1, a catalytic study was conducted for the oxidative coupling of methane reaction. **Figure B2** show the material's catalytic evolution over increasing temperature and the influence of the oxidizing agent used.

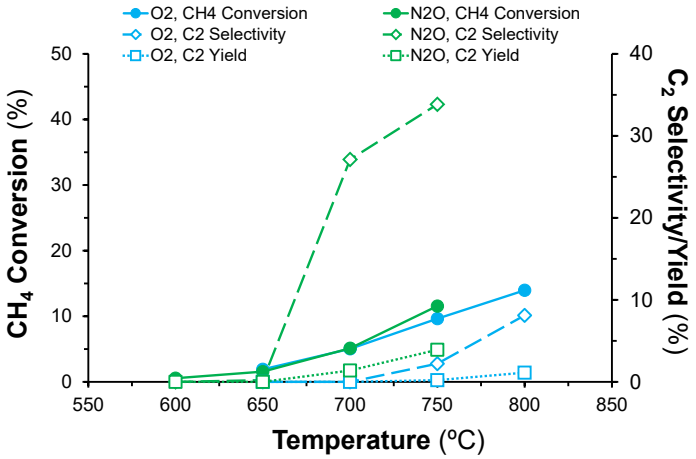

Figure B2: Effect of temperature and the oxidizing agent on the oxidative coupling of methane over Ga:Ce (1:1) aerogel under O_2 and N_2O. (Reaction conditions: Oxidant/CH_4=1, GHSV=15000 mL $CO_2/g_{cat}.h$).

In this reaction, the material tested under N_2O achieves slightly higher CH_4 conversion and selectivity towards C_2 products (such as, C_2H_4 and C_2H_6), leading to a better C_2 yield. For instance, at 750 °C, under N_2O the catalyst converts 12% of CH_4 versus 10% under O_2. However, due to higher C_2 selectivity (34% versus 2%), the C_2 yield of Ga:Ce (1:1) is a lot higher under N_2O than under O_2 (3.9% versus 0.2%, respectively). Thus, it can be concluded that N_2O promotes a better catalytic performance in this reaction.

The results show that the selectivity and the yield to methane via hydrogenation of CO2 or the selectivity and yield to ethylene via OCM are very low and it was decided to put our efforts into other reactions that are more promising, namely ODHE.